

WADC TECHNICAL REPORT 54-368
PART 2
ASTIA DOCUMENT NO. AD 151 018

TRANSIENT AERODYNAMICS OF TWO-DIMENSIONAL AIRFOILS

Part 2. Interferometric Measurements of
Airflow Development about an NACA 65-010
Airfoil in Shock-Initiated Subsonic Flow,
Including Transient Stalling Effects

J. Ray Ruetenik
Emmett A. Witmer

Massachusetts Institute of Technology

March 1958

Aircraft Laboratory
Contract No. AF33(616)-3259
Project No. 1350
Task No. 13605

Wright Air Development Center
Air Research and Development Command
United States Air Force
Wright-Patterson Air Force Base, Ohio

JUL 9 1958 REC'D

PROPERTY OF COOK RESEARCH LIBRARY

Contrails

FOREWORD

This report was prepared by the Aeroelastic and Structures Research Laboratory of the Massachusetts Institute of Technology, Cambridge, Massachusetts, under Air Force Contract No. AF33(616)-3259, Project No. 1350, Task No. 13605, (UNCLASSIFIED TITLE) "Atomic Weapon Effects on Aircraft Systems." The authors are J. Ray Ruetenik and Emmett A. Witmer; the latter was project leader in charge of the work covered under Contract No. AF33(616)-3259. The work was administered under the direction of the Aircraft Laboratory, Wright Air Development Center, with Mr. Francis J. Janik, Jr., acting as project engineer.

The cooperation and assistance of Mr. Janik and his group contributed materially to the success of this study. Professors Raymond L. Bisplinghoff and James W. Mar provided helpful suggestions and guidance of this work. We acknowledge with thanks the assistance of: Mr. George A. Reitano and Mr. Eugene DiFrancesco for assistance in conducting the experiments and in making the measurements; Mr. Phillip Andrews and Mrs. Ruth Lyon for aiding in reduction of the data. Finally, Miss Mary E. Carlo and Kathryn Roberts are thanked for their careful typing of this report, and Mr. George Falla for preparing the photographs appearing herein.

Contrails

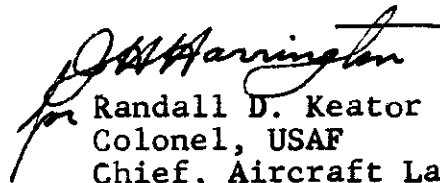
ABSTRACT

Interferometric measurements of the transient flow pattern developments about an NACA 65-010 subjected to shock-initiated flow of Mach number 0.4 are reported. Supplementary motion-picture studies of the behavior of an array of tufts placed on the upper surface of the airfoil are also discussed. The transient airforces, as deduced from interferometric data for small angles of attack, are shown to behave in a manner similar to the behavior predicted by potential-flow theory. At high angle-of-attack conditions, a decidedly different transient flow behavior is noted; this transient-stalling behavior is examined in detail.

PUBLICATION REVIEW

This report has been reviewed and is approved.

FOR THE COMMANDER:



Randall D. Keator
Colonel, USAF
Chief, Aircraft Laboratory
Directorate of Laboratories

Contrails

TABLE OF CONTENTS

<u>Section</u>		<u>Page</u>
I	Introduction	1
II	Experimental	2
	2.1 General	2
	2.2 Interferometric Studies	3
	2.3 Tuft Studies	4
III	Analysis	6
	3.1 Interferometric Studies	6
	3.1.1 Diffraction-Loading Pressure Distribution	6
	3.1.2 Example of Steady-State Potential- Type Flow	13
	3.1.3 Example Pattern of Nearly-Stalled Flow	15
	3.1.4 Example of a Transiently-Stalled Pattern of Flow	20
	3.1.5 High Angle-of-Attack Steady-State Stalled Flow	23
	3.1.6 Pressure Pattern with Strong Leading-Edge Vortex Present	25
	3.1.7 Summary Remarks	26
	3.2 Tuft Studies	27
IV	Results and Discussion	28
	4.1 The Diffraction Loading	29
	4.2 The Post-Diffractive Loading	33
	4.3 Tuft Studies	40
	4.4 Remarks on Theoretical Airload Predictions	42
V	Conclusions and Recommendations	46
	References	49
	Figures	51
	Tables	87

Contrails

LIST OF ILLUSTRATIONS

<u>Figure</u>		<u>Page</u>
1	Summary of Physical Data on the MIT-WADC Shock Tube.	51
2	Comparison of Theoretical and Experimental Density History at the Test Station in the MIT-WADC Shock Tube.	52
3	Comparison of Theoretical and Experimental Dynamic-Pressure Histories at the Test Station in the MIT-WADC Shock Tube.	53
4	View of the NACA 65-010 Airfoil Model.	54
5	Sequence of Single-Fringe Flow Interferograms Illustrating Airflow Development about the Airfoil.	55
6	Location of Tufts on the Upper Surface of the Airfoil	61
7	Sample Photographic History of Tuft Behavior.	62
8	Typical Interferogram during Diffraction-Loading Period.	63
9	Typical Interferogram of Potential-Type Steady-State Flow	64
10	Typical Interferogram of Steady-State Nearly-Stalled Flow.	65
11	Chordwise Pressure Distribution for the Fig. 10 Density Pattern.	66
12	Typical Interferograms of Transiently-Stalled Flow.	67
13	Chordwise Pressure Distributions for the Fig. 12 Density Pattern	69
14	Typical Interferogram of Steady-State Stalled Flow.	70
15	Typical Interferogram with Vortex Starting from the Nose.	71

LIST OF ILLUSTRATIONS (Continued)

<u>Figure</u>		<u>Page</u>
16	Characteristic Time of Tuft-Indicated Flow Reversal as a Function of Angle-of-Attack.	72
17	Histories of Ratio of Normal-Force Coefficient to Angle-of-Attack during the Diffractive-Flow Period.	73
18	Histories of Ratio of Normal-Force Coefficient to Angle-of-Attack during the Post-Diffraction Period.	74
19	Pressure Drag Coefficient History during the Diffractive-Flow Period.	75
20	Histories of the Ratio of Pressure-Drag Coefficient to Angles-of-Attack during the Diffractive-Flow Period.	76
21	Histories of the Ratio of Pressure-Drag Coefficient to Angle-of-Attack-Squared during the Diffractive-Flow Period.	77
22	Histories of the Ratio of Pressure-Drag Coefficient to Angle-of-Attack during the Post-Diffractive-Flow Period.	78
23	Histories of the Ratio of Pressure-Drag Coefficient to Angle-of-Attack-Squared during the Post-Diffractive-Flow Period.	79
24	Histories of the Ratio of Moment Coefficient about the Leading Edge to Angle-of-Attack during the Diffractive-Flow Period.	80
25	Histories of the Ratio of Moment Coefficient about the Leading Edge to Angle-of-Attack during the Post-Diffractive-Flow Period.	81
26	Contribution to C_N Due to Chordwise Displacement of Top- and Bottom-Surface Shocks.	82

LIST OF ILLUSTRATIONS (Continued)

<u>Figure</u>		<u>Page</u>
27	Illustration of Moving-Gust Flow Model and Idealized Shock-Tube Flow Model.	83
28	Comparisons of Theoretical and Experimental Variations of the Ratio of Lift Coefficient to Angle-of-Attack during the Diffractive-Flow Period.	84
29	Comparisons of Theoretical and Experimental Variations of the Ratio of Lift Coefficient to Angle-of-Attack during the Post-Diffractive-Flow Period.	85
30	Downstream Displacement History of the Strong Leading-Edge Vortex for the 30-Degree Angle-of-Attack Case.	86

LIST OF TABLES

<u>Table No.</u>	<u>Content</u>	<u>Page</u>
I	Test Conditions for Interferometric Studies; $\alpha = 4.9$ and 5.0 Degrees.	87
II	Test Conditions for Interferometric Studies; $\alpha = 10.0$ Degrees.	89
III	Test Conditions for Interferometric Studies; $\alpha = 14.7$ and 15.6 Degrees.	90
IV	Test Conditions for Interferometric Studies; $\alpha = 30.0$ and 30.3 Degrees.	92

SECTION I INTRODUCTION

In reference 1 interferometric studies of flow-pattern development about a double-wedge airfoil set at 0, 4, and 8.3-degree angles of attack and subjected to shock-initiated Mach 0.4 flow in the shock tube were reported. While the shape of the double-wedge profile made it convenient for use in the early stages of developing the associated shock-tube testing and interferogram analysis techniques, the sharp leading edge of the profile led to separated flow regions behind the leading edge even at small angles of attack. In order to avoid the difficulties associated with such a sharp leading edge and then to extend these transient airforce investigations to study transient flow phenomena associated with much larger angles of attack, the present experiments reported herein were performed using a two-dimensional NACA 65-010 airfoil.

These latter tests were conducted in the MIT-WADC 8-by 24-inch shock tube using shock-initiated flow of Mach number 0.4 and a number of airfoil angles of attack, α , ranging from 5 to 30 degrees. Flow Reynolds numbers of 1,300,000 for $\alpha \leq 12.5$ degrees and 600,000 for $\alpha > 12.5$ degrees were used, based upon the chord of the airfoil.

The primary measurements were sequences of interferograms of the flow development for several fixed angles of attack. Supplementing these measurements were photographic studies of the behavior of an array of tufts placed on the upper surface of the airfoil. Section II describes the experimental procedure and Section III deals with analysis of the data. In Section IV the results of the present study are discussed while Section V focuses attention on pertinent conclusions and recommendations.

Manuscript released by the authors on 30 December 1957 for publication as a WADC Technical Report.

SECTION II

EXPERIMENTAL

2.1 General

The MIT-WADC 8- by 24-inch shock tube used in the subject studies is shown diagrammatically in Fig. 1 along with a summary of certain pertinent physical data. For the present series of tests, the tube was operated using ambient air in both the expansion and the compression chamber so as to produce a shock-initiated flow having a particle Mach number, M_2 (the subscript 2 represents the fluid immediately behind the shock at the test station) of 0.4. Reynolds numbers of 600,000 and 1,300,000 were obtained by having initial expansion-chamber pressures, p_1 , of 0.5 and 1.0 atmospheres, respectively.

The flow immediately behind the flow-initiating shock at the test section was computed by the familiar Rankine-Hugoniot relation as in reference 1 from measured values of the initial pressure, p_1 , and temperature, T_1 , in the expansion chamber and the shock speed, U . While ideal shock tube theory predicts a step-function flow, such is not actually realized in practice. Boundary-layer influence and non-ideal diaphragm bursting are among the factors responsible for this deviation from the ideal. In reference 1, measurements of shock-initiated-flow density history, $\tilde{\rho}$, and deduced dynamic-pressure history, \tilde{q} , are reported, and they are reproduced in Fig. 2 and Fig. 3 of this report. Since these results are tentative, the recently predicted dynamic-pressure history by Mirels and Braun in reference 2 are shown for comparison. It is interesting to note that, in contrast with our experimental observations shown in Fig. 2, the Mirels-Braun theory predicts a more

nearly constant density, and yet their predicted dynamic-pressure history is in reasonable agreement with that deduced from interferometric measurements. In order to obtain a more direct dynamic-pressure history, \tilde{q} was measured with a total-and a static-pressure probe of the unbonded strain-gage type. The reliability of the latter measurements is questionable because of the low damping coefficient of the transducing system, although the measured results are expected to be in the right direction. These results are also shown in Fig. 3. Incidentally, shock tube dynamic-pressure history measurements are currently under way using a barium-titanate transducer, which are expected to be substantially more reliable.

The importance of the fact that the actual shock-initiated flow deviates from the ideal step function can be appreciated by noting that actual values of airfoil airforce coefficients after 60 flow chordlengths, for example, would be of the order of 23 percent smaller than would be deduced on the basis of a step-function flow of $M_2 = 0.4$ used in the present instance.

2.2 Interferometric Studies

An NACA 65-010 two-dimensional airfoil (a section view is shown in Fig. 4) having a chord of 3.900 inches spanned the 8-inch tube width and was set at angles of attack of 5, 10, 15, and 30 degrees. For each angle of attack, a series of runs was made, in each run of which an interferogram of the flow pattern was made at a different pre-selected time after the flow-initiating shock had struck the leading edge of the model, thereby yielding a reasonably complete picture of the flow-pattern development.

The test procedure for these interferometric studies is identical to that described in reference 1; hence, the reader is invited to consult reference 1 for any further details of interest. It should be noted that whenever needed, multiple-fringe interferograms as well as single-fringe interferograms were made of the flow.

Figure 5 shows typical sequences of interferograms for each angle-of-attack case. The test conditions for the studies are listed in Tables I through IV.

2.3 Tuft Studies

Other measurements supplementing the interferometric measurements were made during additional runs by photographing the behavior of an array of tufts on the airfoil's surface using a Fastax camera operated at 10,000 frames per second. These tuft studies were made at airfoil angles of attack of 7.5, 10, 12.5, 15, 20, and 30 degrees. For $\alpha \leq 12.5$ degrees the Reynolds number was 1,300,000, while for $\alpha > 12.5$ degrees the Reynolds number was 600,000. However, at $\alpha = 10$ degrees, flow Reynolds numbers of 1,300,000 and 600,000 were used to examine whether or not noticeable differences in tuft-indicated flow behavior would result.

Figure 6 shows the array of tufts on the surface of the airfoil, so arranged that the upstream tufts would not alter the flow about the downstream tufts. These tufts each consisted of a single strand of No. 10 mercerized cotton crocheting yarn. Each strand was attached along 1/8 inch of its length to the surface of the airfoil with rubber cement; the remaining 1/2 inch of the strand was free. This free end of the strand was then unravelled to form a tuft.

Contrails

A portion of a typical film strip is shown in Fig. 7 for the case in which the angle of attack of the airfoil is 15.6 degrees. Timing marks applied at a rate of 120 per second are visible on the edge of the film. Shock arrival was detected by noting the first deflection of the tufts (see frame 5) and by the displacement of a small paper flag (see frame 6) glued on the inside of the test-section window. Flag movement is detectable as early as 32 microseconds after shock arrival, as revealed by spark shadowgraph studies.

Since the tuft studies were intended to reveal the local flow-direction histories, especially for those cases in which transient stalling and subsequent flow separation appeared (from the interferograms) to be present, the question of the response times of the tufts is raised. As an indication of this response time, it was observed that after shock arrival the tufts consistently moved from their initially vertical direction to being flattened along the surface in about 0.4 milliseconds (or $\Delta s/c = 0.6$).

SECTION III

ANALYSIS

3.1 Interferometric Studies

An examination of the sequence of interferograms for each angle of attack shows that there are perhaps 4 or 5 types of flow regions which require somewhat different treatments in order to determine the pressure distribution on the surface of the airfoil from the flow density distribution which the interferogram shows directly. These several types of flow regions are depicted in Figs. 8 through 15. Figure 8 shows an interferogram for $\alpha = 5$ degrees while the flow-initiating shock is passing over the airfoil. The steady-state density pattern for $\alpha = 5$ degrees is depicted in Fig. 9. For $\alpha = 10$ degrees, the associated typical steady-state density pattern is as shown in Fig. 10. Figure 12 shows a typical density pattern wherein transient stalling is taking place when $\alpha = 15$ degrees: Fig. 14 shows the steady-state stalled pattern of density for the 30-degree angle of attack case. The final type of density pattern to be discussed is that of Fig. 15 which depicts the density pattern while the initially-shed leading-edge vortex is passing downstream across the surface of the airfoil. Tentative procedures for analyzing each in order to determine the surface pressure distribution will next be described briefly. The pressure forces were then summed to obtain the aerodynamic coefficients: lift coefficient, normal-force coefficient, drag coefficient, and moment coefficient, using \tilde{q} from Fig. 3.

3.1.1 Diffraction-Loading Pressure Distribution

Figure 8 shows a typical density pattern which

Contrails

occurs while the flow-initiating shock is passing over the airfoil. At the point on the airfoil nose where the surface is parallel to the incident shock, head-on shock reflection occurs. Gas particles in that vicinity are shocked first by the flow-initiating shock and again by the stronger reflected shock. These gas particles are therefore at a higher level of entropy than are those free-stream gas particles traversed only by the basic flow-initiating shock.

As the flow-initiating shock travels along the surface of the airfoil, the combination of incident shock strength and angle of incidence of this shock with respect to the surface is such that the regular reflection pattern (that is, the incident and reflected shock meet at the surface) occurs. Because of the fact that the incidence angle of the primary shock is changing as the shock moves along the surface, the strength of the shock reflected from the surface is also changing, and therefore the entropy levels of gas particles progressively encountered from the initial shock contact point to the flow-initiating shock itself, will vary.

When the flow-initiating shock has moved farther along the surface, the angle of incidence of the shock becomes such that a regular reflection pattern cannot occur; the triple-shock Mach configuration then appears. For the incident shock strength used in these experiments, the critical angle between the shock front and the local surface tangent for the onset of Mach reflection is approximately 43.8 degrees. For all angles of attack used herein for the NACA 65-010 airfoil, the onset of Mach reflection occurs when the shock is within 0.02 chordlengths of the nose of the airfoil. It should be noted that the strength of the regular-reflected shock quickly decreases as this shock front expands outwardly from the nose, and it will be shown that, except for those gas particles that are shock initiated in the immediate vicinity of the nose itself, the gas particles swept over by the reflected shock have their entropies increased only very slightly by the

Contrails

latter, and therefore from the nose to the slip surface the fluid is essentially at the free-stream entropy. The Mach shock stem then moves along the surface, being oriented normal to the surface at its point of contact. Subsequently, as this Mach configuration grows approximately in space-time similarity, a slip surface is traced out from the surface of the airfoil to the triple-point itself, and since the fluid is in motion following the shock the whole pattern moves downstream.

The procedure for reducing the interferograms during the diffraction period was discussed in reference 1, and, for the sake of consistency, was employed in the present measurements. This procedure will be described briefly, and then it will be examined rather carefully because some features do exist in the flow pattern about the present type of airfoil that were less pronounced in the flow pattern about the double-wedge airfoil. An estimate will be made of the accuracy of this procedure.

The flow field during the diffraction period is, for purposes of analysis, divided into three regions. One region is triangular and is bound by the slip surface (or triple-point path for coordinates fixed on the free-stream particles), the Mach stem, and the upper surface of the airfoil. A second region, also triangular, is bounded by the lower surface of the airfoil, the Mach stem, and a slip surface. The third zone is the remainder of the flow field. For convenience of reference in the following discussion, the whole of the afore-mentioned triangular regions will be referred to as slip zones. The apparent triple-point path will be termed the slip surface. These three regions are shown in Fig. 8.

Outside of the slip surfaces, the entropy was assumed to be uniform (i.e. homentropic) at the value produced behind the undisturbed flow-initiating shock, so that the reference properties are p_2 , ρ_2 , q_2 , etc. Inside of the two slip surfaces, (that is, in the "slip zone") the (different) entropy was accounted for in accordance with an observation from the analysis of Ting and

Contrails

Ludloff³. They analyzed the problem of a shock moving along a wedge. Their results showed that the steep entropy gradient present essentially occurred across the slip surface, which had a small but finite thickness, and that over the remainder of (what is herein termed) the "slip zone", the isobars coincide with the isopycnics (isodensity lines). Therefore, in reference 1 and in the present experiments, the isobars and fringes (isopycnics) were treated as being identical outside of the slip surfaces; the isobars were extrapolated across the slip surface, rejoined, and thereafter paralleled the fringe pattern within the slip zone, but at a new fringe number. This is shown in Fig. 8. There is some variation in the free-stream flow, associated with shock attenuation, but the change across the flow field shown in any one interferogram is so small that it can be neglected. The effect of the shock reflected from the nose will now be examined.

The maximum entropy rise occurs at a very small region at the nose of the airfoil when the shock first contacts the airfoil and reflects. The entropy is higher than in the free stream, and the error in the pressure coefficient, C_p , using the free-stream value would be -0.11. But the reflected-shock strength decreases so rapidly that this value is not significant in any of the interferograms that were taken; only a very limited amount of fluid would have its entropy raised by this order of magnitude. The largest pressure ratio across any reflected shock in the present series of interferograms was 1.33 at $\alpha = 30$ Deg. (a shift of 20 fringes in run 95.35). This occurs near the triple point below the airfoil, and the rest of the reflected shock is much weaker. The entropy rise given to the fluid at this point would cause an error in C_p of -0.01, whereas the ΔC_p from one fringe to the next is 0.13. At $\alpha = 15$ degrees, the error in C_p based upon free-stream rather than actual entropy would be -0.004, and continues to decrease rapidly with decreasing angle of attack (or reflected shock strength). A conservative estimate of the C_N error would be to

Contrails

assume that the above-mentioned error in C_p occurred over the whole lower surface from the nose to the shock. At $\alpha = 30$ degrees the error in C_N would be 0.4 percent, and at $\alpha = 15$ degrees the corresponding error is 0.2 percent. Therefore, all of the fluid outside of the slip surfaces can be treated as being homentropic with good accuracy.

The slip zone on the lower surface of the airfoil will now be examined. In all of the interferograms where the shock is between the nose and the mid-chord point, the depth of this zone is small so the isobars can be extrapolated across the slip surface and to the surface of the airfoil accurately. In this case the fringes are essentially parallel to the shock indicating that the pressure gradient across this region is small. In the later pictures where the shock is past the midchord point, the thickness of the subject region is still small in the 15- and 30-degree angle-of-attack interferograms. It is only the 5- and 10-degree angle-of-attack cases, where this triangular region is thick and the fringes therein tend to run parallel to the surface, that need further examination in order to determine how the surface pressure on the airfoil can be reliably determined.

Consider again the interferogram in Fig. 8 for the 5 degree angle-of-attack case. At the intersection of the slip surface and the lower surface of the airfoil, the fringe shift across the slip surface is one fringe. Fringe 97 in the slip zone then has a pressure equivalent to that of fringe 98 outside of this triangular region. This evaluation is accurate at the slip surface itself, but at the Mach shock-airfoil surface intersection, the shock strength produces a density which corresponds to about fringe 97, so the entropy there is very near the free-stream value (which is approximately denoted by fringe 100), whereas

Contrails

by the one-fringe adjustment, it was treated as being at a higher entropy, with the error in C_p being 0.066. To estimate the error in C_N , it is noted that the pressure is accurate at the slip surface and is high at the shock; hence, if the reasonable assumption that the pressure error is linear in between is made, the error in C_N at $\alpha = 5$ degrees is 3.0 percent. The error in C_p at $\alpha = 10$ degrees is the same, so the percentage error in C_N is 1.5 percent. These errors are small.

The depth (normal to the airfoil surface) of the slip zone on the upper surface of the airfoil is large at all of the angles of attack, and must therefore be examined with care at all angles of attack, for isobar extrapolation to the surface is a more uncertain procedure than for the similar region of the lower surface. For the 5 degree angle-of-attack case, Fig. 8, the fringe shift at the intersection of the slip surface and the airfoil surface is one-half of a fringe. Fringe 93 in the triangular slip zone is at the same pressure as fringe 93-1/2 outside of the zone. Therefore, one-half was added to each fringe number along the airfoil surface from the slip surface to the shock to obtain the pressure, using the free-stream entropy as a reference for conversion of density to pressure. The shock strength at the intersection point of the Mach stem and the upper surface produces density which corresponds to fringe 86, so the entropy there based on the Rankine-Hugoniot equations requires subtracting 0.5 fringes to use the free-stream p/ρ^* equation. Hence, the error in C_p at the shock intersection on the upper surface is the same as on the lower surface, and therefore they cancel in computing C_N . This is also true for the (later) run 77.18, and the (earlier) run 77.33, Fig. 5.

Contrails

For angles of attack ranging from 10 to 30 degrees, the upper slip surface is not so pronounced and with increasing α appears to vanish, so the entropy in the triangular slip zone was taken to be equal to the free-stream entropy. Actually the entropy decreases slightly along the upper airfoil surface from the nose towards the shock as the shock has been weakened as it travels over the upper surface of the airfoil; hence, the pressure near the shock is actually higher than it was taken to be, and the error at this point can be computed as follows. The location of the upper slip surface can be determined from the lower slip surface. By again assuming a linear increase in the C_p error from the intersection of the slip surface and the airfoil's surface to the Mach shock, the error in C_N can be estimated. The error is the largest when the shock is nearest the trailing edge, so these cases were computed at each angle of attack. At $\alpha = 10$ degrees, the error in C_N was 0.7 percent, and decreased to 0.4 percent at $\alpha = 30$ degrees. Both are negligible errors.

In summary then it appears that the method of extrapolation into the slip zone below and above the airfoil is accurate to within 3 percent in all cases. Further refinement would require finding the entropy of all of the fluid particles along the surface by locating where each was shock initiated, the shock strength at initiation, and then tracing its movement until the time of interest, that is, at the instant of time corresponding to the interferogram in question.

An error of even greater magnitude occurs in the measurement of the chordwise position of the shocks on the upper and the lower surfaces. In the interferograms, the shock has an apparent thickness of about 0.007 chords

irrespective of angle of attack. Added to this difficulty of resolution is the bunching of the fringes at the Mach shocks, so a reasonable estimate of the uncertainty in the measurement of the chordwise displacement between the two shocks would be 0.01 chords. Due to the large pressure difference across the shock, this shock-displacement error represents an uncertainty in C_N of 0.04. Based upon peak values of C_N during the diffraction period, this corresponds to a percentage error of 7.5 at $\alpha = 5$ degrees and 0.8 at $\alpha = 30$ degrees.

The accuracy in measuring the effective chordwise position of a fringe of given number is estimated to be one-fifth of a fringe. This leads to an uncertainty in C_N of 2 percent at $\alpha = 5$ degrees, and decreases with increasing angle of attack to 0.7 percent at $\alpha = 30$ degrees. The accuracy of the aerodynamic-time coordinate in the plots of the aerodynamic coefficients during the diffraction period, namely s/c , is primarily dependent upon the measurement of the shock position. The estimated uncertainty in s/c is 0.01. This is believed to be a conservative estimate.

3.1.2 Example of Steady-State Potential-Type Flow

Figure 9 is an interferogram of the steady-state potential-type-flow density pattern for the 5-degree angle-of-attack condition. Whereas in the flow pattern of Fig. 8 the boundary layer had not developed to a noticeable extent, the boundary layer in the Fig. 9 pattern is pronounced. Invoking the assumption of zero pressure gradient across the boundary layer, the isobars, which are represented by the fringes themselves in the outer flow, are extrapolated smoothly across the boundary layer to the surface as indicated in Fig. 9. In practice, the density data are

Contrails

converted to pressure data by assuming isentropic conversion from stagnation-point conditions which occur at the point of maximum density near the nose of the airfoil, as seen in the interferogram. Isentropic compression was assumed to occur from the free-stream flow to the stagnation point. With the stagnation-point conditions (free-stream total pressure and density), it was assumed that the pressure associated with a given density at any point in the flow field (other than in the boundary layer itself and in certain other regions to be discussed below) is that resulting from an isentropic process from stagnation-point conditions. An alternative assumption for a control point is that some point in the flow field (fringe 102, for example) may be assumed to represent the conditions p_2 , ρ_2 or \tilde{p} , $\tilde{\rho}$.

Through the use of multiple-fringe interferograms, the actual density at any given fringe position can, in fact, be readily determined. It has been found that an error of up to five fringes in selecting the fringe to which p_2 , \tilde{p} , or stagnation p applies results in a normal-force coefficient error of less than one percent. In practice, the proper control fringe can usually be selected by inspection to within 2 fringes. Since single-fringe interferograms require considerably less time and effort than would be the case if multiple-fringe interferograms were used, the former were employed for the vast majority of measurements reported herein. Further, evaluation of single-fringe interferograms leads to acceptably accurate results for the present experiments.

Behind the airfoil, a "thermal" wake is visible. It appears that the primary flow over the top surface has not undergone significant viscous heating, because across the wake, where constant pressure is expected, fringes of

equal number (10^4) or density appear. Also it should be noted that the density gradient in the outer flow along a line normal to the wake extends smoothly across the wake.

It is estimated that the lift-and normal-force coefficient determinations for flow patterns of the present type are accurate to within about 5 percent. The accuracy of the aerodynamic-time coordinate in the post-diffraction period is primarily dependent upon the time-delay measurement. The estimated accuracy of the time delay is 0.2 percent, which is quite sufficient for these purposes.

3.1.3 Example Pattern of Nearly-Stalled Flow

Figure 10 is an interferogram of the "steady-flow" density pattern for $\alpha = 10$ degrees. It is seen that the density pattern over the bottom surface is similar to that of Fig. 9 and is analyzed as described in the previous few paragraphs; whereas, on the top surface, the type of flow represented by the pattern of Fig. 9 no longer occurs, that is, the pattern is approaching that associated with separation. Vorticity is continually being shed behind the leading edge. This region of distributed vorticity passes downstream over the upper surface, apparently spreading and diminishing in intensity as it does so.

Whether isobars can be considered to extend smoothly across this vorticity layer, as is assumed for conventional boundary layers, is not clear. However, a tentative such extrapolation, denoted as A, is shown in part (a) of Fig. 10 for determining the "effective" surface density (or pressure) distribution; isentropic conversion from free-stream conditions is used to calculate the surface pressure from the surface distributions of "effective" density as obtained by this extrapolation. Note that this

Contrails

extrapolation starts at a "cut-line" drawn along the apparent outer edge of the subject vorticity region. Some uncertainty does arise in establishing the location of the cut line. This will be discussed below.

It is interesting to note that approaching the surface along the extrapolation from outer "upper-surface" fringe 91, the density falls (in order) to fringe 90, 89, 88, 87, 86.5, and then climbs rapidly (in order) to 87, 88, 89, and 90 as the surface is approached. The fall in density in the outer part of this region appears to be due to viscous heating and a tendency for discrete vortices to form in this shear layer. This will be clearer at 15 and 30 degrees. The final rapid density increase as the surface is approached appears to arise from cooling of the flow by the relatively cold airfoil surface. As the fringes from the vortex-like zone approach the surface, they bend rather sharply, reminiscent of the fringe pattern associated with the boundary layer of the Fig. 9 flow.

As noted in Sub-Division 3.1.2, the "boundary-layer" type of analysis of the upper-surface shearing layer is based upon the assumption that the pressure gradient across this layer (normal to the surface of the airfoil) is small compared to the pressure gradient in the stream direction. Moving in the chordwise direction the pressure above the shear layer rises as the downstream position of the trailing edge is approached, and nearly levels off by fringe 93. By extrapolation A shown in Fig. 10, the pressure on the upper surface at the trailing edge would correspond to fringe 93 (at free-stream entropy). On the bottom surface at the trailing edge, the pressure corresponds to about fringe 96 or 97. It is expected that the upper-surface pressure at the trailing edge should be very near the lower-surface

pressure at the trailing edge because the flow behind the trailing edge is believed to have little or no curvature. Hence, the pressure drop across the thick upper-surface shearing layer at the trailing-edge downstream position is equivalent to a fringe shift of about four fringes, or a ΔC_p of 0.26 at this point. Of course, it should be observed that by extrapolation-procedure A, the extrapolated fringes do come into the surface at an appreciable inclination, which means that a fair transverse pressure gradient was assumed; hence, the boundary-layer assumption is not strictly followed. But, the pressure drop normal to the surface across the thick vorticity layer obtained by extrapolation procedure A is generally small compared to the difference between the resulting upper-surface pressure and the lower-surface pressure at the trailing edge. Therefore it is concluded that extrapolation A is defective by the discrepancy at the trailing edge.

To correct extrapolation A so that the pressure on the upper and lower surfaces agree at the trailing edge, a pressure increment was added to the pressure values on the upper surface. This pressure increment was taken as zero at the leading edge, and to increase linearly to the trailing edge at such a rate that the upper-surface and lower-surface pressure agree at the trailing edge. This is believed to be a reasonable although only a first order correction since, except at the trailing edge itself, the proper chordwise correction-pressure distribution is uncertain. A more elaborate correction at this time is considered unwarranted. The pressure distributions given by these two approaches are shown in Fig. 11. Extrapolation A yields a C_N value of 0.759 while the corrected method gives a value of 0.701 for C_N . Using the corrected method as a

reference, it is seen that the C_N results of these two methods differ by 8.3 percent. The corrected method is believed to be the more accurate and is tentatively recommended; however, direct-pressure measurements should be made to evaluate the adequacy and appropriateness of this correction procedure.

In addition to the afore-mentioned chordwise-pressure correction, there is uncertainty as to the proper extrapolation procedure to establish the "effective" density distribution along the upper surface in the first place. Since extrapolation procedure A is not a well-defined procedure, in that the way in which the isobars should be extended to the surface is not entirely clear, it is useful to define an extrapolation procedure which, from the standpoint of construction alone, involves lesser uncertainties. Such a more-readily-defined procedure is denoted as B and is also shown in part (a) of Fig. 10. In this case, each isobar is extrapolated normal to the chord line from the intersection point of the fringe and the cut line.

A third estimate (C) of the effective surface density distribution on the upper surface might be made by following the fringes through the vorticity region smoothly and extrapolating across the very dense fringe layer immediately adjacent to the surface (see part (b) of Fig. 10). Again, isentropic density-to-pressure conversion would be applied from free-stream conditions; the afore-mentioned chordwise-pressure correction might also be applied. The pressure distributions obtained by extrapolations A, B, and C are shown in part (a) and each distribution modified by the linear chordwise-pressure correction is given in part (b) of Fig. 11.

For the example flow of Fig. 10, the values of normal-force coefficient, C_N , obtained by (uncorrected) extrapolations A, B, and C are 0.759, 0.695, and 0.878, respectively. Applying the chordwise-pressure correction, these become 0.701, 0.637, and 0.878, respectively. It is seen that there is a significant difference in C_N by which extrapolation procedure is used; the chordwise-pressure correction is fairly important. It is seen in cases A and B that the chordwise-pressure correction is as important as the method of extrapolation. The lowest value of C_N is 16 percent below the highest, so using method A with the chordwise-pressure correction, giving 0.701 in this case, means the uncertainty is about 10 percent. The data presented in Section IV were obtained by the method A. Method C was compared only because it had been used for some calculations in the past. The value of C_N departs considerably from the others, and the method is somewhat more difficult to define. This method is not recommended.

Finally, it should be noted that the conventional boundary-layer pressure-extrapolation method (Sub-Division 3.1.2) is appropriate for the $\alpha = 10$ degree flow until $s/c = 1.71$ (run 78.28). Thereafter, the shearing layer rapidly thickens near the nose, spreads downstream, and hence makes the pressure determination more obscure. However, even at $s/c = 3.82$, extrapolation method A appears to have reasonable reliability. The shearing layer is thin enough to warrant straight-forward extrapolation ahead of the trailing edge; in addition, the vorticity layer has not quite reached the trailing edge so the pressure above and below the wake can be compared unambiguously. The increasing pressure toward the wake in the region above the airfoil extends smoothly into the values below the airfoil. It is

then at later times that the real uncertainty in the pressure determination arises.

3.1.4 Example of a Transiently-Stalled Pattern of Flow

At $\alpha = 15$ degrees for small values of s/c the pressure on the airfoil can be computed by the methods already described. The important exception is the region of the nose vortex, which was difficult to measure at 5 and 10 degrees. The fringes are so dense in the nose vortex that the pressure in this region must be obtained by extrapolation from the known region until $s/c = 1.12$. At $s/c = 1.89$ the fringes are all distinct, and the problem is one of arriving at an estimate of the entropy to obtain the pressure. We will first examine one of the interferograms at 15 degrees where the shearing zone covers the whole upper surface to establish a procedure, then describe how it was applied before the shearing zone reached the trailing edge.

Figure 12 shows a transiently-stalled pattern of flow for $\alpha = 15$ degrees and $s/c = 6.02$. Again, over the lower surface, the flow is essentially homentropic; hence, the lower-surface pressure distribution is readily determined as previously described. But above the airfoil, the flow is separated, and whereas at $\alpha = 5$ and 10 degrees the fringes above the shear layer exhibited a definite tendency to descend nearly normal to the shear layer, and therefore, with reasonably small uncertainty, could be extrapolated across the layer to the upper surface of the airfoil, they are now running essentially parallel to the shear layer. Thus, a new basis must be established to determine the pressure distribution along the upper surface.

Several new features should be noted before the reduction procedure is established. Except near the outer

edge of the thick vorticity region which covers the upper surface, the density gradient normal to the surface is small. This indicates that the shearing essentially takes place near the outer edge of the zone. In this vorticity region the surface cooling effects are not as evident as in the flow patterns previously discussed. Also, the transverse pressure gradient is probably not large over most of the region. The outer shearing layer is not a simple plane surface, there are large vortices that leave the nose of the airfoil and wash downstream, and the outer shear layer tends to wander in between the vortices. In general, from the airfoil surface to the outer shearing layer, the density gradient is small; therefore, within this region precisely what fringe is used to represent the surface pressure does not sensitively affect the resulting computed airforce coefficients for the airfoil.

A further question posed is the extent the gas in the zone above the airfoil has been subjected to viscous heating. Across the wake from bottom-surface fringe 94 is fringe 90, indicating that viscous heating is again significant. For this case also, the magnitude of this entropy effect will be estimated by the linear pressure correction described in the previous sub-division.

Two methods have been studied for assigning an "effective" distribution of density along the upper surface. In the first (see Fig. 12-a), a "cut" line was drawn through the apparent center of the shear zone; this is the line along which the density normal to the surface is a minimum. Surface normals were drawn from the intersections of this cut line with each fringe; in this way the distribution of effective surface density was assigned. In the second density-distribution determination (see Fig. 12-b), the

fringes in apparent contact with the upper surface served to fix the sought distribution.

For both of the above density distributions over the top surface, first isentropic flow was assumed using the stagnation point as a reference and, in addition, the aforementioned approximate correction was applied for entropy variation from front to rear along the upper surface. Comparisons of these pressure coefficient distributions are shown in Fig. 13. The cut-line method gives a value of C_N of 1.56, and the surface-intersection method gives a value of 1.335. The latter method is 14.5 percent less than the former method. After the correction was made for the trailing-edge pressure difference the cut-line method was reduced to 1.265, and the surface-intercept method to 1.135, so that the surface-intercept method agrees better with the cut-line method when the correction is applied, being 10.3 percent less.

The cut-line method was employed on the 15-degree data. From $s/c = 0.89$ to 2.68 it was applied only to the portion of the upper surface which had the nose vortex. The remainder of the upper surface was treated as in Sub-Divisions 3.1.2 and 3.1.3, whichever was appropriate. For the runs at $s/c = 4.04$ and later, the cut-line method was applied to the whole upper surface, and the correction at the trailing edge was also incorporated.

It is difficult to estimate the uncertainty involved in arriving at a pressure distribution in the nose vortex region up to $s/c = 1.12$. The vortex region grows linearly with time, so it is only in the post-diffraction period that it has any importance. An estimate will be deferred for the present, and it will be noted that this is one of the areas where direct pressure measurement is needed. At

$s/c = 1.89$ all the fringes are visible, so an estimate of the uncertainty can be made from the entropy difference at the trailing edge as indicated by the upper and lower-surface fringe difference described above. The entropy discrepancy was such that the average correction to C_N in 16 interferograms was -21 percent, with a standard deviation of 3.3 percent of C_N . The latter number indicates that the entropy rise is rather consistent. The -21-percent correction indicates that the entropy rise is large. The entropy may increase at a faster rate near the nose than it does downstream, so a reasonable estimate of the uncertainty of the entropy correction is 5 to 10 percent. Added to this is the 10-percent difference between the cut-line method and the surface-intersection method, and a 5-percent uncertainty in $\frac{q_1}{q_2}$ at later times. Therefore, the resultant uncertainty in the absolute value of the 15-degree C_N data for $s/c \geq 1.89$ is 20 to 25 percent. But the density profiles in this period are essentially similar, so the uncertainty in the timewise trend (relative uncertainty) is estimated to be about 10 percent.

3.1.5 High Angle-of-Attack Steady-State Stalled Flow

A typical pattern of "steady-state" stalled flow for the 30-degree angle-of-attack condition is shown in Fig. 14. The bottom-surface density pattern is similar to that of the previously-discussed post-diffraction patterns of flow; the bottom-surface flow appears to be essentially homentropic and may be analyzed as discussed previously.

With reference to the upper surface, the flow is seen to separate from the surface near the leading edge, with a separation surface fairly clearly bounding a so-called "dead air" region which extends over the upper

surface. Across the region in a direction normal to the surface, the density gradient is seen to be very small except near the separation boundary itself.

The density distribution along the upper surface can apparently be defined with little difficulty and uncertainty. These density values might then be converted to pressures by assuming an isentropic conversion from the free-stream conditions. A second approach to account, at least approximately, for the viscous heating effects might consist of assuming isentropic flow over the whole upper surface but with the entropy level there being that such that lower-surface fringe 90 and upper-surface fringe 86, for the example pattern, refer to the same value of pressure; the fringe-90 pressure being defined on the basis of isentropic conversion from free-stream conditions. Applying these two schemes to the example flow pattern of Fig. 14, a C_N value of 1.485 was obtained from the former and 1.245 for the latter scheme, a reduction of 16 percent. The latter correction scheme was applied to the 30-degree steady-state-stalled data for delay times of $s/c \geq 9.0$. The average reduction in C_N for 13 interferograms by this correction was 21 percent, and the standard deviation of this correction was 9 percent. The latter number indicates a greater scatter in the correction between runs, although this is not necessarily indicative of the accuracy of the correction. A large scatter in the entropy on the top surface would be expected between runs at such a large angle of attack. A reasonable estimate of the uncertainty in the entropy correction would be 10 percent of C_N . Including the uncertainty in $\frac{\tilde{q}}{q_2}$, the combined uncertainty is about 15 percent, which is somewhat better than at $\alpha = 15$ degrees.

3.1.6 Pressure Pattern with Strong Leading-Edge Vortex Present

Figure 15 shows the density pattern which occurs early in the development of the flow about the airfoil at $\alpha = 30$ degrees. The initial vortex shed from behind the leading edge is seen to be exerting a powerful influence on the upper surface; it appears not to exert an unusual influence on the bottom-surface flow. The bottom-surface flow is essentially homentropic and may be analyzed as discussed previously; the boundary layer there is apparently still very thin.

Assuming that the fluid of the vortex has a constant entropy (neglecting the region very near the vortex center itself), Howard and Matthews⁴ obtained good agreement between computed and measured radial density distribution in a vortex produced behind a flat plate set normal to a shock-initiated flow. Hence, it appears reasonable to assume that the fluid in the vortex region above the airfoil is homentropic. The upper-surface pressure in the vortex region was computed from the density values of the fringes at the fringe-surface contact. Note that there is a small region along the upper surface from the nose to the near-circular fringe pattern about the main vortex wherein the density is nearly constant. (Also, near the trailing edge in Fig. 15 is a boundary layer where the extrapolation of section 3.1.2 was employed.) This method was applied to the runs at $\alpha = 30$ degrees, from the time the slip zones left the airfoil until $s/c = 8$. In several of the later runs during this period, the fringe number at the trailing edge was slightly different on the top and bottom surfaces. This was corrected by the linear method described in Sub-Division 3.1.3.

3.1.7 Summary Remarks

It is believed that the interferometrically-deduced airforces are reliable throughout the observation period from initial shock impingement through the steady-state pattern of flow for $\alpha = 5$ degrees. This is also believed to be the case for $\alpha = 10$ degrees except that the evaluation uncertainty increases at large values of s/c because of the presence of the vortex-like zone extending over the upper surface. For the late-transient and steady-state patterns for $\alpha = 15$ and 30 degrees, the evaluation uncertainty is greater. Certain estimates of this uncertainty have been made and are described in this report; however, direct-pressure measurements are believed necessary in order to resolve these uncertainties. Such transient pressure measurements are being made at the present time in the shock tube at MIT, and results of these studies will be presented in a future report.

3.2 Tuft Studies

Before each test the tufts were oriented normal to the airfoil surface. At shock arrival the tufts were first driven flat to the airfoil surface in the direction of the shock, and after an interval of time, which depended upon the angle of attack of the airfoil, the tufts at $\alpha \geq 10$ degrees reversed direction. The problem was to select a method of describing this tuft behavior so as to present the essential features of the flow-direction indication as represented by the tufts.

After the tufts were hit by the shock, it was consistently 0.4 milliseconds (or $\Delta s/c = 0.6$) at all angles of attack before they lay flat. The tufts continued to point downstream for a period which depended upon α , and then at $\alpha \geq 12.5$ degrees the tufts would lift from the surface and reverse direction until they pointed upstream. The time interval required for this latter reversal was 0.6 milliseconds ($\Delta s/c = 0.9$). This reversal time was so nearly the same at these values of α that only the delay time at which the reversal was complete was reported. This is given in Fig. 16. At $\alpha = 10$ degrees the tufts would occasionally flutter and sometimes swing partially upstream then quickly return downstream, and even occasionally completely reverse direction, but the reversal was not correlatable with delay time so it was not plotted. At $\alpha = 7.5$ degrees the tufts always pointed downstream.

SECTION IV

RESULTS AND DISCUSSION

It is desirable to divide the transient airforce development into a "diffractive" and a "post-diffractive" phase. In reference 1 the diffractive phase was defined as terminating when the undisturbed shock traveled one chord length downstream from the leading edge of the airfoil: which is approximately equal to c/U , or nondimensionalized is $s/c = u_2/U$, which is $s/c = 0.3$ at $M_2 = 0.4$. As was pointed out, the two phases are not distinct since shock waves continue to pass over the airfoil after $s/c = 0.3$, and the rotational flow generated by the Mach shock leaves at about $s/c = 1$. Because the airforces continue to change rapidly for a short time after $s/c = 0.3$, it is convenient to discuss the airloads in the two modified periods: (a) from $s/c = 0$ to 1, and (b) for $s/c > 1$, which will be called, respectively, the diffractive and post-diffractive periods.

The methods of interferogram analysis described in Section III were employed to obtain the surface pressure distribution for each interferogram of the sequence for each angle of attack. These pressure forces were summed in order to determine lift, normal force, moment, and pressure drag. In turn these forces were converted to coefficient form on the basis of airfoil chord and the density-indicated dynamic pressure given in Fig. 3. These airforce-coefficient results are presented in Figs. 17 through 25.

First, results of interferometric studies during the diffractive-loading period will be discussed. Then, interferometric results during the post-diffractive period of loading will be considered. Next, the results of the tuft studies will be reviewed. Finally, some remarks concerning theoretical airforce predictions during the diffraction and the post-diffraction periods, including transient stalling, will be made.

4.1 The Diffraction Loading

Before proceeding to examine the experimental time histories of the various airforce coefficients during the diffractive-loading period, it is useful to examine briefly the flow phenomena observed interferometrically in this period. In Fig. 5 one observes that as the airfoil is shock enveloped, the shock which passes over the lower surface is strengthened by reflection whereas that passing over the upper surface is, in general, rarefaction weakened. As a result, the lower-surface shock travels faster than does the upper-surface shock and thus progressively moves ahead of the upper-surface shock, reaching the trailing edge first. At the trailing edge the flow induced by the bottom-surface shock tries to turn the corner and follow the shock as it itself turns the corner and moves forward on the upper surface toward the on-coming upper-surface shock. It is during this time that a counter-clockwise "starting" vortex is observed to form behind the trailing edge.

During passage of the upper- and lower-surface shocks over the airfoil, initially regular shock reflection occurs; but, very shortly as the shock moves farther along the airfoil, the Mach reflection pattern is produced. As the Mach reflection pattern grows, in approximate space-time similarity, a slip surface is traced out extending from the surface of the airfoil to the triple point of the Mach configuration. The features of this pattern have been discussed in detail in Sub-Division 3.1.1 with reference to Fig. 8.

Following collision of the upper-surface and the lower-surface shocks, a pattern of rarefaction and compression waves forms and spreads. Since the primary shock-initiated flow is subsonic in the present test series, these waves can be observed to move forward over the airfoil.

The phenomena just described are observed for both small and large airfoil angles of attack. At large angles of attack, however, additional flow phenomena are observed. The

oncoming stream of flow tries to turn about the leading edge and to follow the surface but is unable to do so and separation occurs. The attendant large velocity gradient then leads immediately to the formation of a clockwise vortex which becomes very strong and considerably influences the surface pressure distribution while near the airfoil. The vortex is still very small by the time the shock reaches the trailing edge, so the discussion of this vortex will be deferred to Division 4.2 on the post-diffraction loading.

As previously mentioned, the shock passing over the lower surface is reflected and strengthened while that passing over the upper surface is rarefaction weakened. Consequently, the lower-surface shock gets ahead of the shock on the upper surface. It is interesting to see what portion of the normal-force coefficient, C_N , is due to this shock displacement; that is, what the contribution to C_N is due to the net pressure force on that chordwise part of the airfoil covered by the bottom- but not yet by the top-surface shock. This contribution to C_N as shown in Fig. 26 is seen to be nearly independent of α at any value of s/c for the presently-examined range of α , although there is some data scatter. The measurement uncertainty is greatest for the smallest angle-of-attack condition. In view of the large contribution of this shock displacement it will be important to include it in any theoretical analysis of the diffraction period.

Figure 17 shows C_N/α as a function of s/c . Within the present measurement accuracy, C_N/α appears to be independent of α while the shock is passing over the airfoil. C_N/α appears to increase nearly linearly, reaching a maximum when the shock traversing the lower surface reaches the trailing edge of the airfoil. Subsequently C_N/α decreases, reaches a minimum at about $s/c = 0.58$, and again increases. The peak diffraction-loading value of C_N/α appears, for the present shock-strength condition, to depend primarily upon the angle of attack of the airfoil.

Concerning theoretical prediction of such transient airforces, it may be noted that no compressible-flow model representing the shock-tube flow field to which the airfoil has been subjected has yet been analyzed to yield theoretical air-force time histories. However, Miles⁵, Hobbs⁶, and Diederich and Drischler⁷ have analyzed the incompressible-flow problem to predict the transient airforces on a flying airfoil subjected to a uniform vertical-gust field headed by a boundary which envelopes the airfoil at an arbitrary rate. This 'moving-gust' model is depicted in part (a) of Fig. 27, while the model of the stationary airfoil subjected to shock-tube flow is shown in part (b) of Fig. 27. It is found that the features of the theoretical generalized indicial-lift functions associated with the moving-gust flow model depend upon a parameter* $\lambda = \frac{V+V_g}{V}$ which is the ratio of the sweep speed of the gust boundary over the airfoil to the airfoil speed, where V and V_g are depicted in Fig. 27. As special cases, the Wagner function is given for $\lambda = \pm \infty$, and the Küssner function for $\lambda = 1$.

While not strictly correct, assume the shock-tube airfoil to be in forward flight at a (shock-initiated flow) velocity u_2 while the shock is passing over the airfoil. In this case, $\lambda = \frac{U}{u_2}$. Using this characteristic parameter, the indicial-lift function for a flat plate airfoil (Ref. 6), with the Prandtl-Glauert correction applied, is as shown on Fig. 28. It is seen that there is an initial lift pulse of similar peak value but of different shape from that measured. This theoretical lift pulse is contributed largely by apparent-mass forces although some

* The parameter λ may also be regarded as defining the reciprocal of the number of chordlengths of airfoil travel while the gust front is passing over the airfoil (see Fig. 27a).

small circulatory-lift contributions are also present as the Kutta condition is invoked immediately from the instant of airfoil contact with the gust boundary. The experimental lift pulse on the other hand arises primarily from forces due to shock reflection. It may be said, however, that the incompressible-flow apparent-mass forces and the compressible-flow shock-reflection airloads arise from the same basic cause; namely, that of satisfying the condition that the flow must not penetrate but flow parallel to the surface of the airfoil.

For a thin airfoil at $\alpha = 0$ degrees, it is expected that the pressure drag at any instant during passage of the shock over the airfoil is approximately equal to the shock overpressure times the net projected thickness of the portion of the airfoil already shock enveloped. This was confirmed in the double-wedge airfoil test¹, where the thickness ratio was 10 percent. As airfoil thickness and angle of attack are increased, shock reflection effects occur to the extent that a drag greater than this simple rule implies is found to occur as shown on Fig. 19 where this calculated value is compared to measured values of C_{Dp} . Figure 20 shows C_{Dp}/α versus s/c while C_{Dp}/α^2 versus s/c is shown in Fig. 21. In Fig. 20 the 5-degree data do not follow the other C_{Dp}/α data well during the early period. The 10- and 15-degree data are correlated until $s/c = 0.3$, and the 30-degree data have a similar profile, except on an expanded time scale. In Fig. 21 it is apparent that none of the data are correlated by C_{Dp}/α^2 during the period the shock is passing over the airfoil, $s/c < 0.3$; but, all of the data, except for $\alpha = 5$ degrees, are in good agreement in the interval $0.4 < s/c < 1.0$.

Referred to the leading edge of the airfoil, the moment coefficient, C_{M_0} , divided by α is shown as a function of s/c in Fig. 24; a reasonably good correlation is observed.

4.2 The Post-Diffractive Loading

Following the diffraction-loading period, a gradual change took place in the pattern of non-separated flow at $\alpha = 5$ degrees, finally attaining the conventional "steady-state" pattern of flow. The transient airforce behavior is discussed with reference to Fig. 18 which shows C_N/α against s/c for $\alpha = 5, 10, 15,$ and 30 degrees. It is seen that the airforce development for $\alpha = 5$ degrees is quite similar to that of the familiar Wagner function. This is better illustrated in Fig. 29 where, for comparison, the generalized indicial-lift function for a flat-plate airfoil, with the Prandtl-Glauert correction applied throughout and for $\lambda = \frac{U}{u_2}$ is shown. Also included are the reference 1 results for the u_2^2 double-wedge airfoil at $\alpha = 4$ degrees. The measured forces initially (that is at $s/c = 1$) start lower but catch up by and surpass after $s/c = 3$, then fall below and level off until $s/c = 14$, and finally rise and again level off at a value slightly below the flat-plate theory. This behavior suggests that the actual shed vorticity may be more concentrated than that of the theoretical model, leading to this lower initial value and the subsequent more rapid growth of airloading. In the incompressible-flow theory, vorticity is shed from the trailing edge both while and after the gust (or shock) boundary is passing over the airfoil; whereas, in the actual case, gust-induced vorticity cannot be shed from the trailing edge until the shock front (which is the first signal to arrive) reaches the trailing edge. Thus, a different strength-time history of shed vorticity from that given by incompressible-flow theory should not be unexpected.

For large values of s/c , C_N for $\alpha = 5$ degrees appears to have attained a steady-state value which is seen to be in excellent agreement with steady-state values measured in a wind tunnel⁸. A number of repeat runs were made, with the results duplicating well over the entire range of values of s/c except at

$s/c = 6$. The latter spread has not been explained as yet, but is not believed to be significant.

For the 10-, 15-, and 30-degree angle-of-attack cases, the flow over the bottom surface was similar to that at $\alpha = 5$ degrees; however, on the upper surface, a transient pattern of separated and vortex-like flow was observed which finally developed into patterns reminiscent of those associated with conventional stalled flow over the airfoil. It is during the transient period that the airloads exhibit distinct differences from those of the case in which flow separation and stalling are absent as represented by the flow pattern history for the $\alpha = 5$ -degree case.

Leading-edge separation has recently been receiving considerable attention in connection with thin straight and swept wings which must operate at low speed and high angles of attack. The present series of interferograms shows rather clearly the development of leading-edge separation. Referring to the $\alpha = 30$ -degree sequence of interferograms in Fig. 5, it is seen that the leading-edge vortex starts to form independent of the initial vortex shed from the trailing edge of the airfoil; before a signal from the trailing edge could reach the leading edge, this formation begins and has progressed considerably. As this vortex grows and moves downstream, its center remains essentially at the elevation of the leading edge of the airfoil. The downstream displacement-time history of the center of this vortex is shown in Fig. 30; its downstream speed is quite steady at about 25 percent of the free stream speed while this vortex passes over the airfoil. A back-extrapolation of the space-time position of this vortex would indicate its origin to have been at the leading edge at the instant of shock impingement there.

As this strong leading-edge vortex passes over the airfoil, it exerts a considerable influence on the surface pressure distribution, which is clearly shown in Fig. 5, run 95.23. As this (clockwise) vortex approaches the downstream position of the trailing edge, it provides a very strong transverse

Contrails

velocity gradient which results in the formation of a strong counter-clockwise companion vortex behind the trailing edge. This latter vortex can first be seen in run 95.12; in run 95.27, it has a greater strength such that the density at the apparent center is less than that, at present, of the leading-edge vortex. Repeated runs consistently reveal the presence of this vortex pair. Actually, following the appearance of this initial vortex pair, a whole succession of (much weaker) vortices are observed since a whole succession of weak vortices are shed from behind the leading edge itself. The so-called "steady-state" pattern of flow is, in fact, quite unsteady.

As the angle of attack is increased, the strength of the initial vorticity shed behind the leading-edge increases. At $\alpha = 10$ degrees, a well-defined vortex is not seen; only a region of weak and distributed vorticity is observed. At $\alpha = 15$ degrees there is a more pronounced but elongated region above the airfoil with a low-density zone. At $\alpha = 30$ degrees, however, a well-defined vortex appears.

At $\alpha = 30$ degrees, the post-diffractive loading, C_N , initially grows rapidly, reaching a peak value in agreement with the $\alpha = 5$ degree curve at $s/c = 2.7$. The first peak occurs approximately when the vortex initially shed behind the leading edge has moved downstream to just past the mid-chord point of the airfoil. It is at this time that this clockwise vortex exerts its strongest influence on the airfoil. In fact, over most of the upper surface of the airfoil, this vortex has induced a forward flow. When this initial leading-edge shed vortex has moved to a downstream position abreast of the trailing edge and has induced the (second) trailing edge vortex, this causes a sharp drop in C_N . In the zone between the leading-edge of the airfoil and the (first) nose vortex, the density pattern indicates a stagnant zone until the second trailing-edge vortex begins to form. At the same time the second trailing-edge vortex starts

forming, the second nose vortex appears. Frequently, several vortices formed at the nose which were not as sharply defined as the first nose vortex. These are evident in Fig. 5 at $s/c = 5.85$ and 7.98 . As this vortex (ices) move downstream, C_N builds up until the vortex approaches the trailing edge and the third trailing-edge vortex forms. The latter is evident in Fig. 5 at $s/c = 9.04$ and 9.23 . Again, this vortex is weaker than the preceding (second) trailing-edge vortex. Simultaneously C_N falls abruptly, and the third nose vortex (ices) form. Then C_N builds up for the third time. The third nose vortex is opposite the trailing edge in Fig. 5 at $s/c = 13.2$. There may be a dip in C_N immediately thereafter, but there were not sufficient data to ascertain this. In general, the first vortex is distinct, and the succeeding vortices are successively more irregular until after the third cycle they are very small in size and strength, and apparently of a non-regular period.

The initial regularity of the vortices at $\alpha = 30$ degrees was suggestive of the shedding of vortices on a circular cylinder in forming the Karman vortex street. The Strouhal number, St , defined as $St = \frac{nd}{u}$, relates the shedding frequency of the pairs of vortices, n , to the free-stream velocity u , and cylinder diameter, d . The dependence of the Strouhal number upon the Reynolds number based on cylinder diameter is given, for example, by Roshko⁹ for Reynolds numbers up to 10,000; essentially the Strouhal number has been found to be constant at a value of about 0.2 above a Reynolds number of 400. For the airfoil, if the chord is taken as the characteristic length, the period of the leading-edge and trailing-edge vortex pairs would be $\Delta \frac{s}{c} = 5$ based on a Strouhal number of 0.2, which is in agreement with the peaks in C_N at $s/c = 3, 8, \text{ and } 13$. The agreement indicates a surprising similarity of the wake of the airfoil with the wake of the circular cylinder. It would be of interest to conduct tests at other values of α well beyond the steady-state-stall angle to confirm that the airfoil chordlength is actually the character-

istic length to give vortex-street agreement with the vortex street of the circular cylinder. Furthermore, these results should be independent of the direction of approach of the shock front.

It is of interest to note that Roshko⁹ mentioned that periodic fluctuations have been observed in the wake of a circular cylinder up to the critical Reynolds number, about 200,000. The Reynolds number of the airfoil based upon chord was 600,000, and distinct vortices are expected at early times no matter how high the Reynolds number might be. The important point is that at latter times in the shock tube the vortices become weaker and less distinguishable from the remainder of the flow, and probably lose their regularity (an occurrence which is observed in wind tunnels). Of course, some difference is expected between the critical Reynolds number on the airfoil and the value on a circular cylinder, but it should be remembered that full-scale in-flight airfoils are at very large Reynolds numbers, which are well above the critical value, so that the vortices would become irregular after several cycles.

The next point is to find the effect of decreasing α on this flow pattern. For $\alpha = 15$ degrees, the C_N/α data follow the data for $\alpha = 5, 10,$ and 30 degrees up to $s/c = 1.3$. Then they rise sharply above the other data at $s/c = 2$, and at $s/c = 3$ they reach a peak 25 percent greater than the curve for $\alpha = 5$ degrees. The 15-degree curve then falls, crossing the 5-degree curve at $s/c = 6$ and finding a minimum at $s/c = 9$, another peak at about $s/c = 13$, and finally leveling-off by $s/c = 20$. The force-fluctuation period at $\alpha = 15$ degrees is about double the period observed at $\alpha = 30$ degrees. The uncertainty in the values of C_N at $\alpha = 15$ degrees was estimated to be 20 to 25 percent, which is equal to the departure from the 5-degree data. But the uncertainty estimate was very conservative, so that this possibility is believed to be highly improbable. This will be checked with the direct pressure measurements.

Contrails

At $\alpha = 10$ degrees, the C_N/α data agree well with that for $\alpha = 5$ degrees up to about $s/c = 3$. At this point they fall below the 5 degree curve with some indication of an oscillation at a period about equal to that of the 30-degree data. As a matter of fact, there is even some indication of an oscillation in C_N/α at $\alpha = 5$ degrees; but, the presence of oscillations in only the 15- and 30-degree data is definite. The effect of α on the periods of these oscillations should be re-examined when direct pressure measurements are made. For the 10-degree data, the solid guide curves are drawn to follow the average of the data, although more data might change the curves somewhat. The steady-state data at $\alpha = 10$ degrees, is about 29 percent below that for $\alpha = 5$ degrees.

It is interesting to note that by approximately $s/c = 20$, the steady-state airforces have developed for all of the angle-of-attack cases examined. Within the limits of the various uncertainties previously cited, the transient airforce histories must be regarded as tentative particularly for the cases of $\alpha = 15$ and 30 degrees. Efforts are currently being made to make direct measurements of the surface pressures for the large as well as the small angle-of-attack cases. This work will serve to provide both independent pressure data, and data which will guide analysis of interferograms in complex flow regions.

One effect for which data corrections are not available arises from the interference of the top and bottom walls of the shock tube. When the shock is passing over the airfoil, a reflection pattern develops due to the interference which travels to the floor and ceiling and reflects. The disturbance due to the reflection is not computable at present. But, the time when the reflection arrive at the airfoil is readily calculable, and is shown in Fig. 18. At first glance it might appear that the oscillations in the 10 and 30-degree angle-of-attack data were synchronized with and hence due to these reflections. But this latter possibility is seen to be without validity by considering the qualitative

effect of the interference waves. The first reflections from the floor and ceiling, in order to preserve the boundary of the shock tube, are produced by images that increase the apparent angle of attack. The second set of reflections reduces the apparent angle of attack, etc., which is opposite to the behavior of C_N/α at 10 and 30 degrees in Fig. 18. Therefore, a correction for the interference would accentuate rather than diminish the oscillations in C_N at $\alpha = 10$ and 30 degrees. At $\alpha = 15$ degrees the oscillation frequency definitely differs from the interference wave frequency. However, at $\alpha = 5$ degrees, there is a possibility that the high C_N values after the first reflection are a result of the reflections; even here the small magnitude of this "oscillation" would substantiate the expectation that the magnitude of the interference is small. The strengths of the successive "reflection" disturbances diminish.

Pressure-drag coefficients are difficult to determine accurately percentagewise in the post-diffraction period due to their small magnitude. Figure 22 shows that correlation is poor on the basis of C_{Dp}/α at all times. In Fig. 23 after $s/c = 10$, the data for $\alpha = 5, 10,$ and 15 degrees are correlated within the experimental scatter. The values for $\alpha = 30$ degrees are lower. In the region of s/c between 2 and 10, there is a trend of increasing C_{Dp}/α^2 with increasing α , except again for the 30-degree case.

Although the measurement accuracy leaves much to be desired, histories of the moment coefficient referred to the leading edge divided by α are given in Fig. 25.

4.3 Tuft Studies

A primary aim of the tuft studies was to indicate whether the transient lift build-up at angles of attack above the steady-state stall angle could be treated separately from the flow separation at the surface. That is, whether the transient development was essentially over before separation took place, from which it might be possible to neglect the viscous effects during the transient lift build-up, thereby premitting use of potential-flow solutions. On the other hand, for the flow-separation features, one might treat the response to a step in flow properties neglecting the potential-type time variation.

Figure 16 shows that for $\alpha \geq 15$ degrees, separation occurs early in the transient development. In fact, since the tufts do have a time lag that is of the order of one chord-length of flow, the fluid reversal must take place quite early in the transient period. The only case in these tests where tuft-indicated complete flow reversal definitely occurred after the transient build-up had been completed was at $\alpha = 10$ degrees. At $\alpha = 12 \frac{1}{2}$ degrees, the tuft behavior in the transient period was erratic. One tuft in the first row might reverse upstream while the other pointed downstream, then it might return downstream followed by the other reversing upstream, etc. Generally it was $s/c = 5$ before any tufts reversed direction at $\alpha = 12 \frac{1}{2}$ degrees, although one did reverse at $s/c = 2.5$. Hence, $\alpha = 12 \frac{1}{2}$ degrees is the smallest angle of attack at which complete flow reversal is evident at a time when highly transient airforces are occurring. Also, an angle of attack of $12 \frac{1}{2}$ degrees might be considered as that at which pronounced reversed flow is first evident.

It is interesting to note that, in contrast to the typical wind-tunnel tests involving steady-state stall tests, the peak value of C_N was attained for angles of attack of both 15 and 30 degrees when both the front and rear rows of tufts indicated the flow had reversed direction. This indicates that the

magnitude of the forward velocity at the surface must be quite large, and this conclusion is supported by the rapidity with which the tufts reversed direction from pointing downstream. The reversing time was consistently 0.6 milliseconds compared to 0.4 milliseconds to be flattened following shock arrival, indicating that the reverse velocity was of the order of the free-stream velocity.

Since the flow does reverse direction on the upper surface, there must be a (moving) point of zero flow velocity, and it is of interest to locate this point with respect to the leading-edge vortex that was observed at $\alpha = 30$ degrees. In Fig. 30 the position of the vortex center is plotted as a function of time. Figure 16 in conjunction with Fig. 30, shows that the front tufts, which were attached to the surface at $x/c = 0.23$, were reversed when the vortex was at $x/c = 0.4$; the tufts at $s/c = 0.62$ were reversed when the vortex was at $x/c = 0.7$. If the $\Delta s/c = 0.9$ tuft reversal time is taken into account, along with the finite tuft length, which means that the stagnation point must be a finite distance downstream of the point of attachment of the tuft before the tuft will start to reverse direction, then it would appear that the stagnation point is downstream of the vortex center, as one expects. In fact the flaring of the fringes at $s/c = 0.75$ in Fig. 15 indicates that this is probably the stagnation point in question. From this evidence, it is concluded that the whole upper surface has reversed flow before the peak C_N is reached, a most interesting result in the light of usual airfoil results.

This leading-edge vortex is probably much stronger than any observed on airfoils previously, except where a moving shock wave had passed over an airfoil. Therefore, a separate investigation is now underway to study the formation of these shock-initiated vortices, and then to determine their effect on the pressure distribution about the airfoil.

4.4 Remarks on Theoretical Airload Predictions

Before concluding discussion of the transient airforces for the various angles of attack studied herein, a few remarks bearing upon theoretical descriptions of the observed flow patterns may be useful. First, it should be noted that the presently-available transient airforce theories deal only with conventional potential-type non-separated flow; this is the case for incompressible as well as for compressible subsonic and supersonic flow conditions. Furthermore, as mentioned in Division 4.1, none of the theoretical flow models can be reduced exactly to that to which the stationary airfoil is subjected in the shock tube. Hence, a rigorous comparison of shock-tube airfoil data with theory cannot yet be made.

For the case in which the airfoil in forward flight is subjected to a sharp-edged gust or blast field, the generalized indicial-lift functions of references 5, 6, and 7 for the moving-gust flow model appear attractive. It should be noted however, that the indicial-lift functions pertaining to the moving-gust flow model have been derived only for incompressible flow and for certain supersonic forward-flight speeds. The Wagner and Küssner problems, which are special cases of the moving gust model, have been examined for the compressible flow cases of subsonic and supersonic forward flight speeds.^{7, 10-15}

A few points should be recalled concerning the relative behavior of the indicial lift-growth functions for incompressible and for compressible subsonic flow based upon a linearized treatment of the problem. The predicted lift buildup for the Mach-zero (incompressible flow) case is more rapid than that for any subsonic forward-flight speed. Hence, for subsonic forward flight, the use of the Wagner function tends to overpredict the lift.

Another point worth noting is that the compressible-flow indicial-lift functions of references 14 and 15 for instantaneous gust-front envelopment exhibit an early pulse-type behavior similar to that which would be expected from shock-

diffraction loading. For weak blast or shock impingement from directly underneath, the initial theoretical lift values are reasonable. However, when strong shocks are considered, non-linear effects manifest themselves and the predicted values of starting lift are in error.

It is seen herein that, for a moving-gust flow model selected so as to represent approximately the actual immersion rate of the shock-tube airfoil, as previously-discussed, the theoretical airloading during the post-diffraction period is in general agreement with measurements (see Fig. 29) although some rather distinct differences are also apparent. The diffraction part of both the theoretical and experimental airforces exhibit lift pulses of similar magnitude but of different time histories as Fig. 28 shows.

It is seen from Fig. 18 that when the gust-induced (or geometry induced) angles of attack are beyond that for steady-state stalling, distinctly different airforce time histories are produced. Although scale effects may change these results somewhat, the general character of these airforces is believed to be as shown in Fig. 18. Also, for an airplane in subsonic forward flight exposed to a long-duration blast such that the total wing angle of attack is well beyond that for steady-state stalling, the same general phenomena as observed in these shock-tube experiments, but modified by finite-span effects, are expected to occur.

The problem of predicting the airfoil airforces associated with this transient stalling behavior in the shock tube is a most interesting one and forms a logical starting point for the study of the associated phenomena. Clearly the boundary layer(s) plays an important role in this flow. Although tedious, the shock-diffraction theory of references 3 and 16, modified to account for the non-uniform flow field about the airfoil in steady flight, might be usefully applied to predict the airforces

during shock envelopment of the airfoil, provided that the influence of the leading-edge vortex is not too large since the theory in question does not account for the presence of this vortex. With respect to the formation and growth of this vortex itself, it may be said that at present no theory exists which explains in detail the formation of such a vortex. The history of the strength and the history of the flow field about this vortex are unsolved problems.

Howard and Matthews⁴ among others have observed experimentally that shock-induced vortices behind a flat plate grow in near space-time similarity. In certain simple cases to which it has been applied, a semi-empirical theory developed by Rott¹⁷ has been found to predict the space-time location of the vortex center to within about 10 percent.

On the far end of the time scale (large s/c), steady-state stalling is present. Howarth¹⁸, a number of years ago, considered the problem of predicting the maximum lift on an airfoil. In that problem, flow separation plays a dominant role. Starting with classical potential flow about an elliptical airfoil at a given angle of attack, he calculated the boundary layer and determined the boundary layer separation points on the top and bottom of the airfoil. In order to define the final circulation, he imposed the condition that in steady flow the net vorticity shed at both the top and the bottom vorticity points must be zero. This turns out to be equivalent to the statement that the flow velocity at the outer edge of the boundary layer is equal at these two separation points.* By repeated calculation, the bound circulation, required to meet this condition was found. The qualitative behavior of lift as a function of angle-of-attack is shown by such an analysis; although the quantitative results are found wanting.

* Incidentally, it is interesting to note that the outer flow densities at the two apparent separation points of the steady-state flow pattern for $\alpha = 30^\circ$ appear to be equal.

Contrails

Moore^{19,20} has recently applied the Howarth procedure to the study of "lift hysteresis" associated with small angle of attack changes from the steady-state stall angle of attack. Within certain restrictions, he is able to show that flow separation (at the separation point itself) may be treated as a quasi-steady process. The Moore-Howarth procedure yields qualitatively interesting results although nothing is said about the transient chordwise pressure distribution itself or the wake effect on the pressure distribution. With respect to the application of this theory to the present transient-stalling phenomena, the theory applies to small perturbations from a condition of steady-state stall whereas the phenomena of the present experiments involve very large "disturbances".

During the intermediate period of the airforce development, the flow picture is more complicated. For angles of attack just beyond that at which the fully-potential-flow pattern disappears, the vorticity region which spreads over the upper surface appears to be both weak and poorly defined geometrically. At $\alpha = 30$ degrees on the other hand, a strong well-defined discrete vortex is shed behind the leading edge. It is suggested that as a beginning, one might study an incompressible-flow model which synthesizes (a) the moving-gust model, (b) one or more discrete vortices shed behind the leading edge and having prescribed histories of circulation and downstream-drift velocity, (c) and the flow criteria of Howarth as quasi-steady criteria. The fundamental weakness of such an approach is that the vortices shed behind the leading edge must be prescribed both as to strength and drift histories. Nevertheless, it may be instructive to examine the airforces resulting from this type of flow model. It appears that, in this respect, the least complicated of the experimental cases studied is that for $\alpha = 30^\circ$, with the secondary leading- and trailing-edge vortices, as a first step, being ignored. Further discussion of the airforces occurring during transient stalling will be deferred to a future report.

SECTION V

CONCLUSIONS AND RECOMMENDATIONS

From the present studies and those reported in Part 1 of WADC TR 54-368, the following summary remarks and recommendations result:

1. These studies have shown that the transient lift produced on an airfoil subjected to shock-initiated flow, for cases of small airfoil angles of attack, are in general agreement with potential-flow theory for the moving-gust flow model of Miles⁵, Hobbs⁶, and Diederick and Drischler⁷ which simulates the shock-tube flow. During the diffraction-loading period, both incompressible-flow theory and experiment reveal a lift pulse which in the two cases is of similar peak value but of somewhat different shape. In the post-diffraction period, the experimental and the theoretical airloads develop in a more similar manner although, compared to incompressible-flow theory, the experimentally-deduced airforces are initially smaller but grow at a somewhat faster rate than do their theoretical counterparts in the early portion of the post-diffraction loading.

2. While it has been expected that distinct differences from potential-flow behavior would result when airfoils at large angles of attack were subjected to shock-initiated flow, experiments have revealed these differences in some detail. The character of the transient development of the flow field to its steady-state stall pattern is revealed. As the angle of attack is increased beyond that for the onset of steady-state stalling, the differences between actual and potential-flow transient behavior become increasingly more pronounced. For example, at a 15-degree angle of attack, C_N/α is found to rise up to approximately 25 percent above that for the un-

stalled flow. Further, during this transient-stalling period, one observes oscillatory airforces which are apparently related to the near-periodic shedding of leading-edge and trailing-edge vortices.

3. For studies of the present sort, the interferometer is an extremely valuable tool both qualitatively and quantitatively. Potential-type flow patterns, including conventional boundary layers, can be analyzed with excellent quantitative reliability and accuracy. However, for those cases in which thick regions of vorticity or separated-type flow occur over the upper surface of the airfoil, completely reliable procedures for deducing airforces from the flow-field density data which the interferograms yield directly are not available. Tentative procedures for analyzing such flow fields have been discussed herein and have been applied to analyze pertinent interferograms of the present series of experiments.

In order to resolve the subject interferogram-analysis uncertainties, tests are currently being conducted to measure directly the transient pressure distribution on the airfoil for both small and large angle-of-attack cases. In addition to resolving these interferogram-analysis uncertainties, these studies should provide independent transient airforce information.

4. The interferometrically deduced steady-state lift values for the low angle-of-attack cases examined in this study are in excellent agreement with corresponding wind-tunnel data, being only 4 1/2 percent greater. This agreement serves to bolster confidence in at least a part of the interferogram evaluation techniques employed herein, and in the free-stream values of dynamic pressure \tilde{q} deduced from time history measurements of free-stream density.

Contrails

5. The use of tufts in the present experiments provided a means of supplementing the series of interferograms of the flow-pattern development. While interferograms yield flow-field density data, the tufts serve to indicate the flow direction, and the short time required for the tufts to reverse direction at 15 and 30 degrees indicates that the speed of the reversed flow at the surface was comparable to the free-stream speed. Furthermore, the tufts indicated that for $\alpha \geq 12 \frac{1}{2}$ degrees, the flow reversal occurred very early in the transient period so that essentially at all values of α above the steady-state-stall angle the transient lift development is inseparably related to separation phenomena.

6. The present interferometric and tuft data yield a reasonably clear picture of the flow phenomena associated with transient stalling as well as with potential-type flow development. Hence, while present theories are inappropriate and thus inadequate to describe the non-linear features of the transiently-stalled flow, the dominant features in the problem are revealed. With this experimental background of information, judicious approaches to a theoretical treatment of this subsonic-flow problem are more apparent.

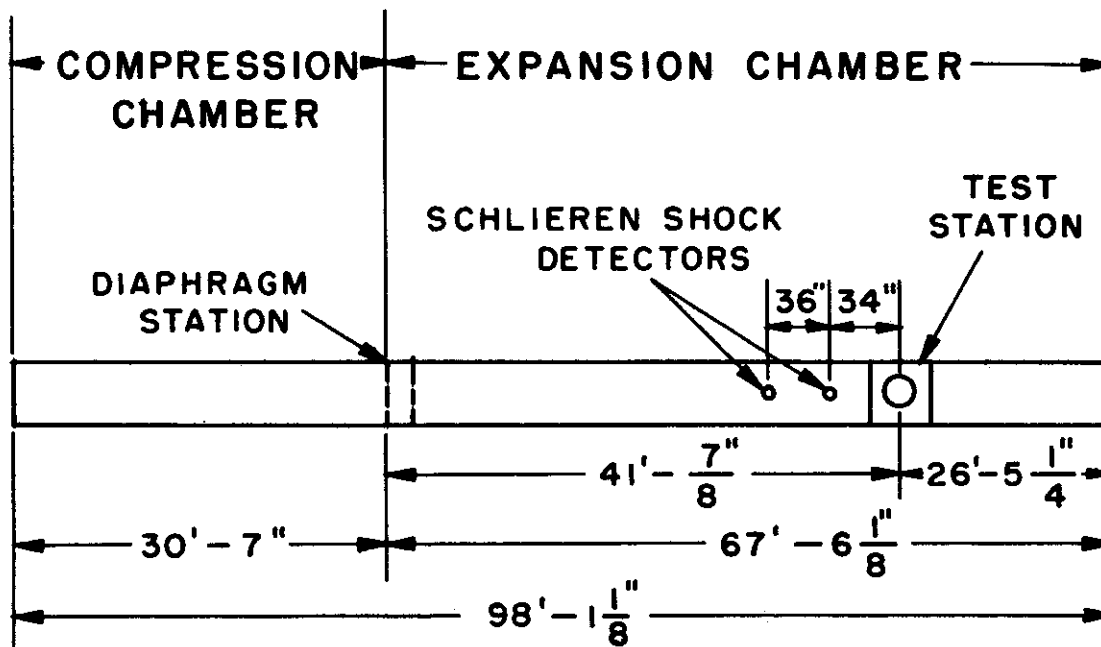
7. It is expected that similar studies involving higher-Mach number flows (both subsonic and supersonic) would reveal valuable flow phenomenology. Such tests are being conducted at $M = 0.8$ and 1.5 ; these results will appear in a future report. Also of interest are finite-span effects on the subject transient airforces at these low subsonic, transonic, and supersonic Mach numbers; work in this area is planned.

REFERENCES

1. Ruetenik, J. R., and Witmer, E. A., Transient Aerodynamics of Two-Dimensional Airfoils. Part 1- Interferometric Measurements of Two-Dimensional Airflow Development about a Symmetrical Double-Wedge Airfoil in Shock-Initiated Subsonic Flow. Massachusetts Institute of Technology, WADC TR 54-368, Part 1, August 1956.
2. Mirels, H., and Braun, W. H., Nonuniformities in Shock-Tube Flow due to Unsteady-Boundary-Layer Action, NACA TN 4021, May 1957.
3. Ting, L., and Ludloff, H. F., Aerodynamics of Blasts, Journal of the Aeronautical Sciences, Vol. 19, No. 5, May 1952.
4. Howard, L. N., and Matthews, D. C., On the Vortices Produced in Shock Diffraction, Journal of Applied Physics, Vol. 27, No. 3, pp. 223-231, March 1956.
5. Miles, J. W., The Aerodynamic Force on a Airfoil in a Moving Gust, Journal of the Aeronautical Sciences, Vol. 23, No. 11, Nov. 1956.
6. Hobbs, N. P., Indicial Downwash and its Structural Effect on the Horizontal Tail, Massachusetts Institute of Technology, WADC TR 56-164, Aug. 1956.
7. Diederick, F. W., and Drischler, J. A., Lift and Moment Responses to Penetration of Sharp-Edged Traveling Gusts, with Application to Penetration of Weak Blast Waves, NACA TN 3956, Jan. 1957.
8. Abbott, Ira H., von Doenhoff, A. E., and Stivers, L. S., Jr., Summary of Airfoil Data, NACA Report 824, 1945.
9. Roshko, A., On The Development of Turbulent Wakes from Vortex Streets, TN 2913, March 1953.
10. Lomax, H., Heaslet, M. A., Fuller, F. B., and Sluder, L., Two- and Three-Dimensional Unsteady Lift Problems in High-Speed Flight. NACA Report 1077, 1952.

REFERENCES (Continued)

11. Biot, M. A., Loads on a Supersonic Wing Striking a Sharp-Edged Gust. Journal of the Aeronautical Sciences, Vol. 16, No. 5, May 1949.
12. Miles, J. W., Transient Loading of Supersonic Rectangular Airfoils. Journal of the Aeronautical Sciences, Vol. 17, No. 10, October 1950.
13. Chang, C. C., Transient Aerodynamic Behavior of an Airfoil Due to Different Arbitrary Modes of Nonstationary Motions in a Supersonic Flow. NACA TN-2333, 1951.
14. Mazelsky, B., Numerical Determination of Indicial Lift of a Two-Dimensional Sinking Airfoil at Subsonic Mach Numbers from Oscillatory Lift Coefficients with Calculations for Mach Number 0.7, NACA TN 2562, Dec. 1951
15. Mazelsky, B., and Drischler, J. A., Numerical Determination of Indicial Lift and Moment Functions for a Two-Dimensional Sinking and Pitching Airfoil at Mach Numbers 0.5 and 0.6, NACA TN2739, July 1952.
16. Ludloff, H. F., and Friedman, M. B., Aerodynamics of Blasts—Diffraction of Blast around Finite Corners, Journal of the Aeronautical Sciences, Vol. 22, No. 1, Jan. 1955.
17. Rott, N., Diffraction of a Weak Shock with Vortex Generation, Journal of Fluid Mechanics, Vol. 1, p. 111, 1956.
18. Howarth, L., The Theoretical Determination of the Lift Coefficient for a Thin Elliptic Cylinder. Proceedings of the Royal Society (London), Ser. A, Vol. 149, No. A 168, pp. 558-586, April 1935.
19. Moore, F. K., Lift Hysteresis at Stall as an Unsteady Boundary Layer Phenomenon. NACA TN3571, Nov. 1955.
20. Moore, F. K., Aerodynamic Effects of Boundary Layer Unsteadiness. Sixth Anglo-American Aeronautical Conference Preprint, September 1957.



Internal Cross-Section	8" x 24"
Internal Length	98'-1 1/8"
Approximate Total Weight of Shock-Tube Proper	13 tons
Maximum Design Pressure	250 psia
Maximum Reynold's No. with a 4-In. Chord Model and Air in the Expansion Chamber	24 million
Maximum Mach No. Currently Obtainable with Air in the Expansion Chamber	1.5

Fig. 1 Summary of Physical Data on the MIT-WADC Shock Tube

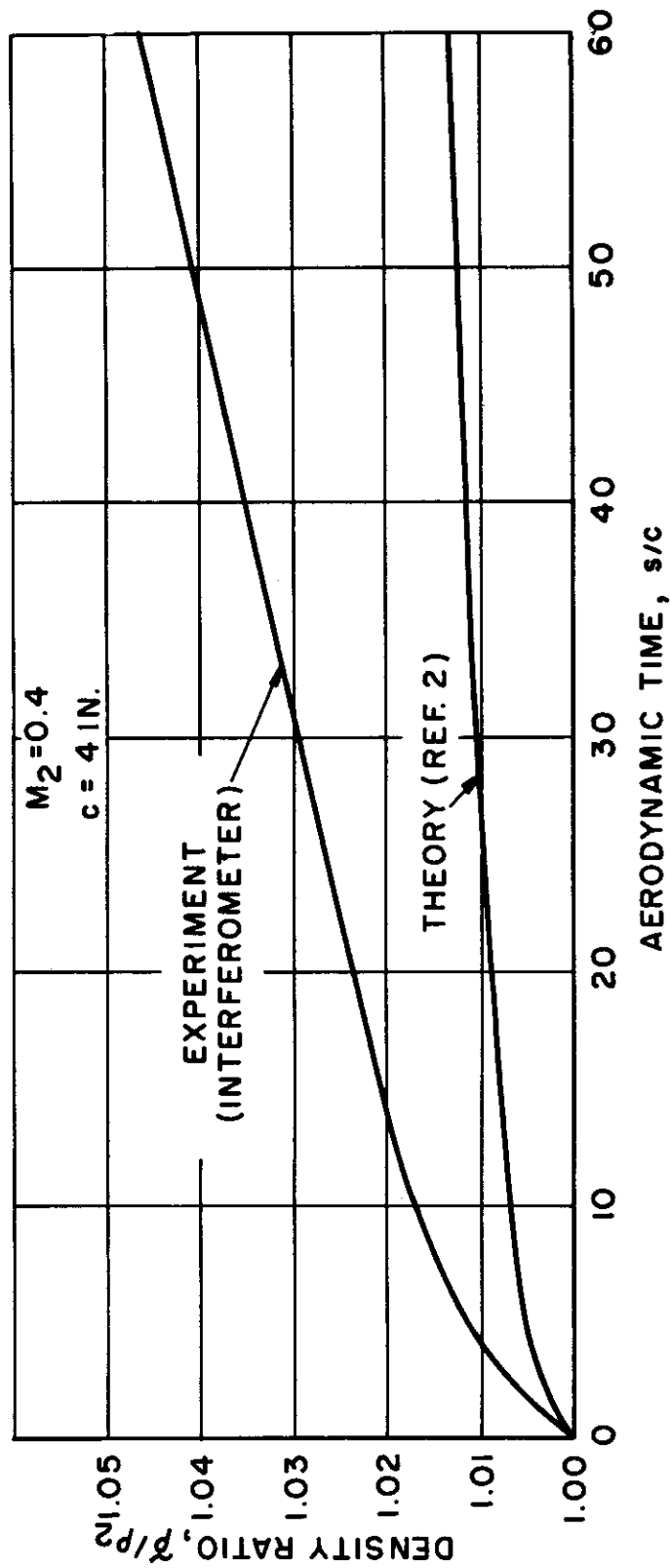


Fig. 2 Comparison of Theoretical and Experimental Density-History at the Test Station in the MIT-WADC Shock Tube.

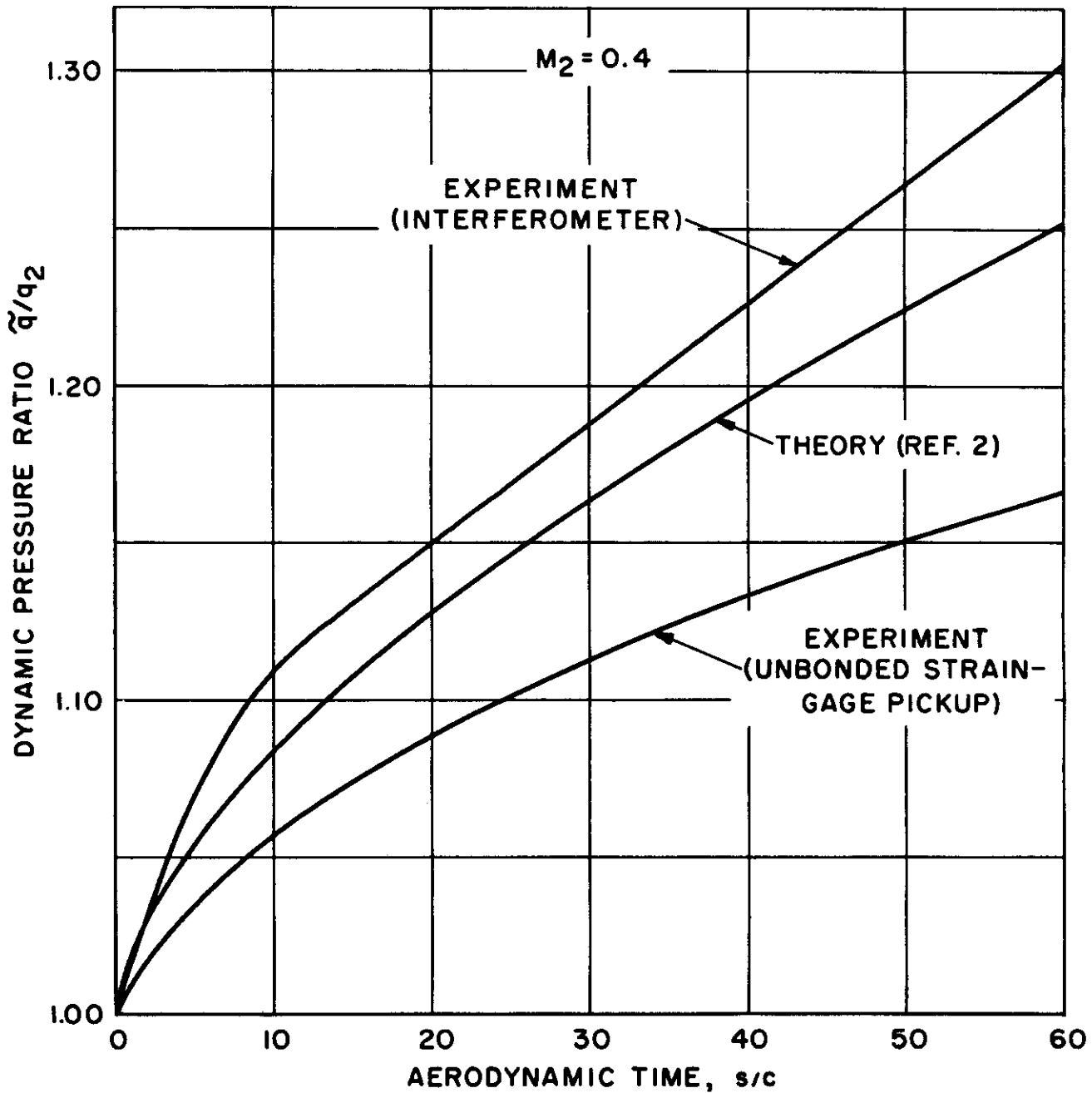


Fig. 3 Comparison of Theoretical and Experimental Dynamic-Pressure Histories at the Test Station in the MIT-WADC Shock Tube

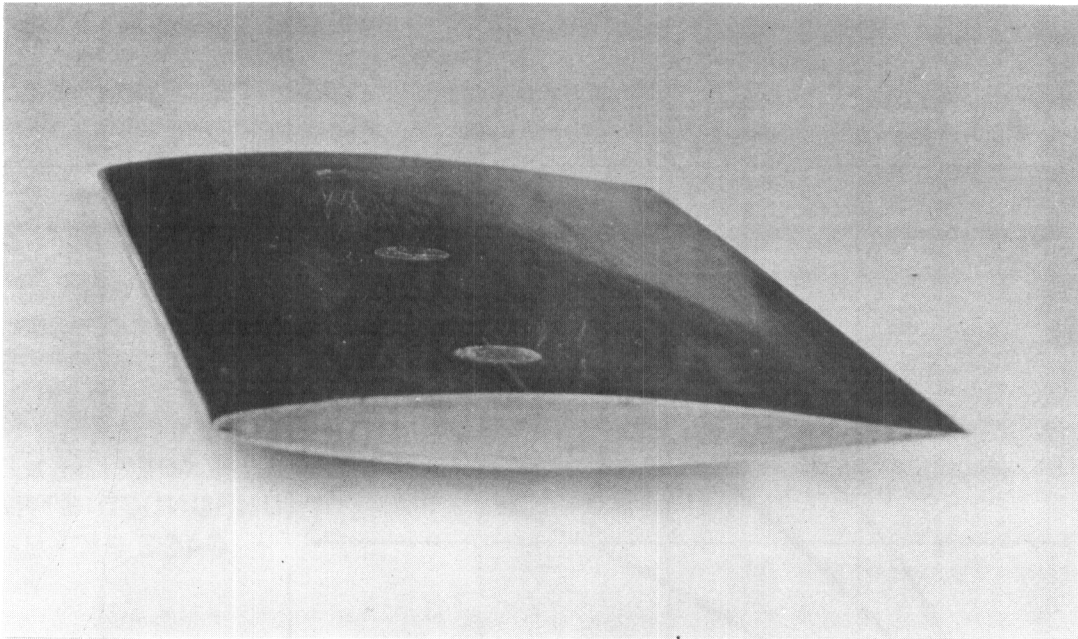


Fig. 4 View of the NACA 65-010 Airfoil Model

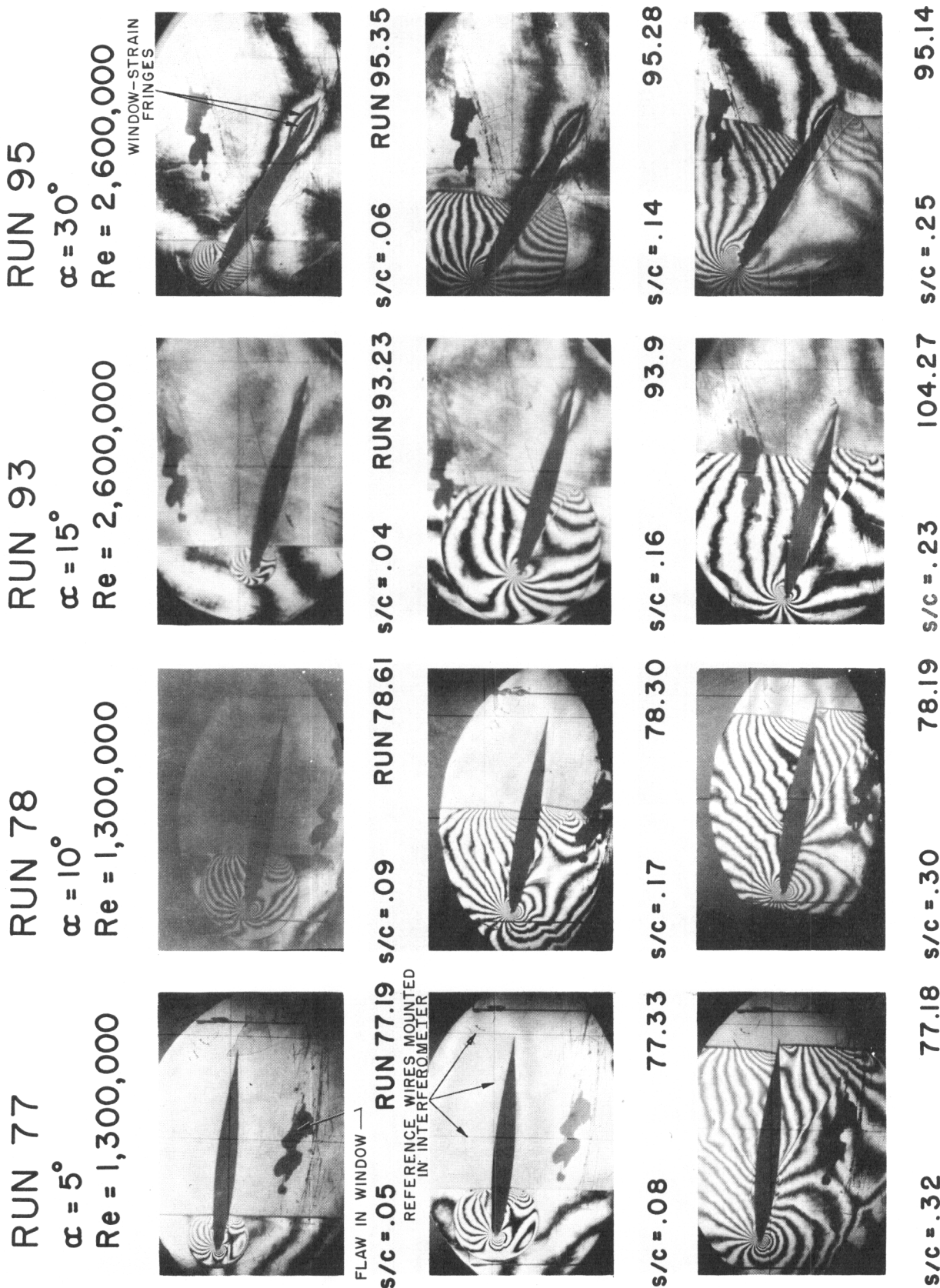


Fig. 5 Sequence of Single-Fringe Flow Interferogram Illustrating Airflow Development about the Airfoil.

Contrails

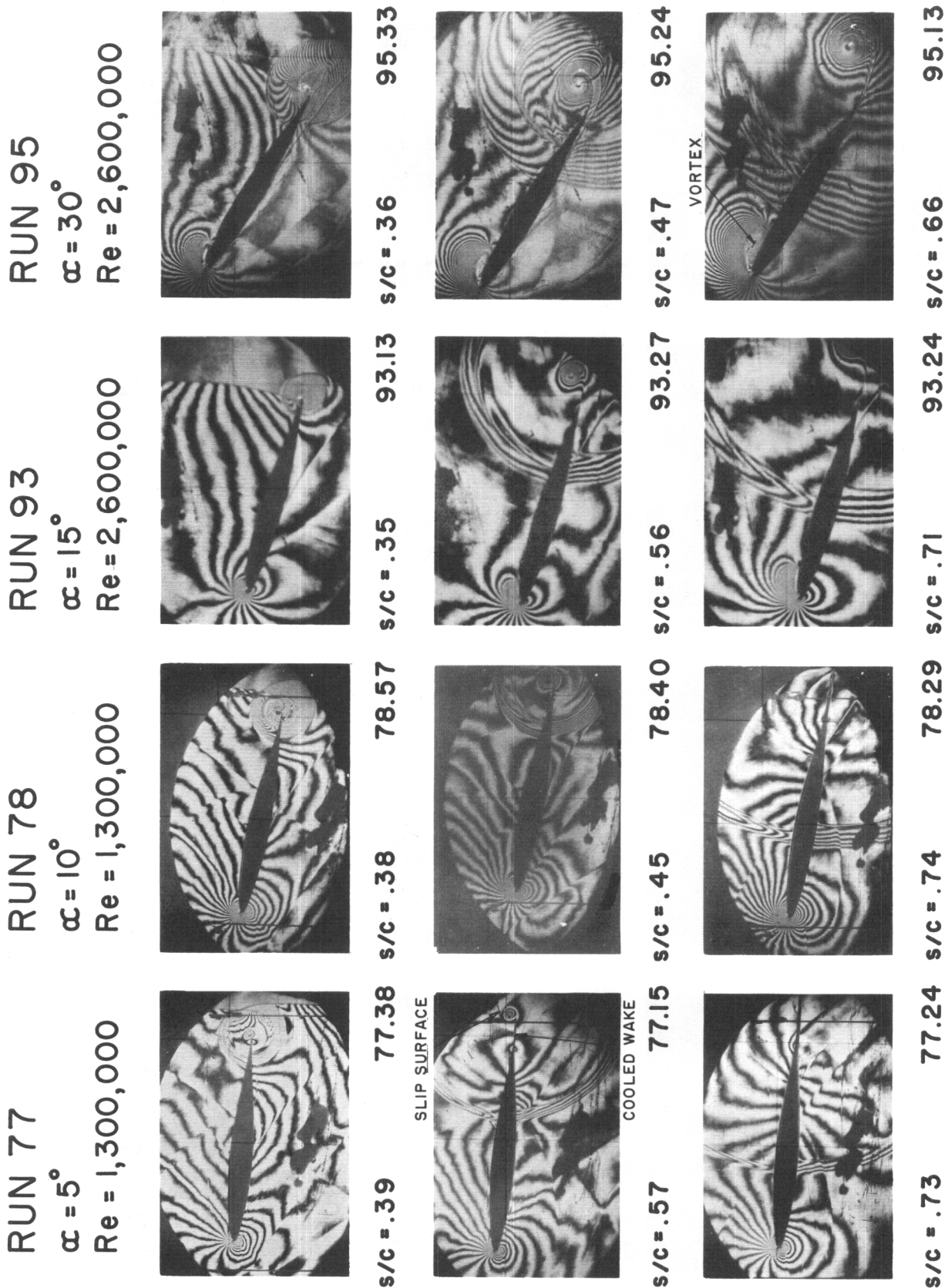


FIG. 5 CONTINUED

Contrails

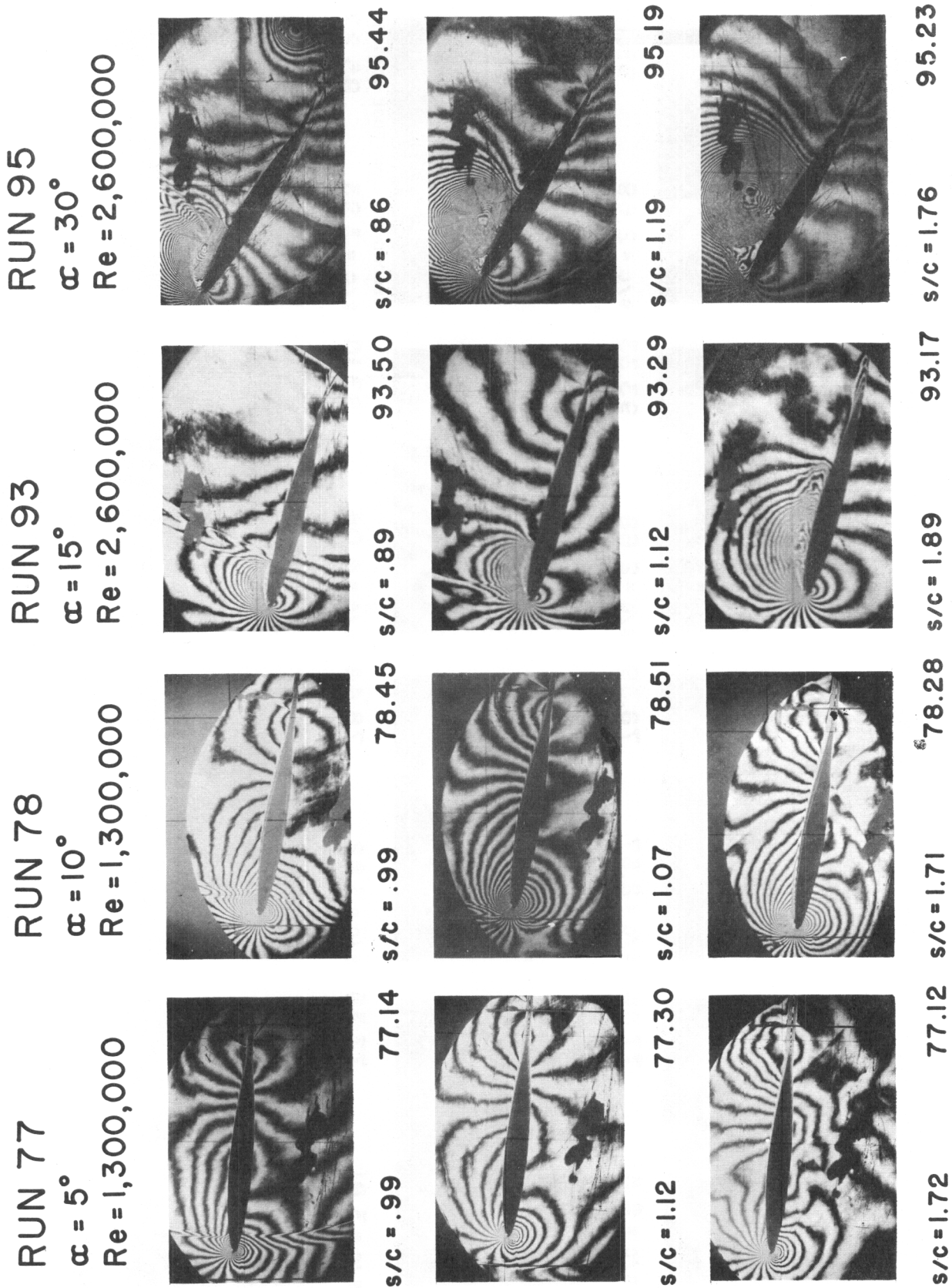


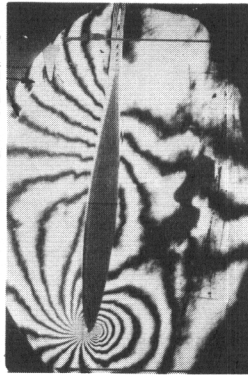
FIG. 5 CONTINUED

RUN 77

$\alpha = 5^\circ$

Re = 1,300,000

REFLECTED WAVE
FROM CEILING



s/c = 2.52

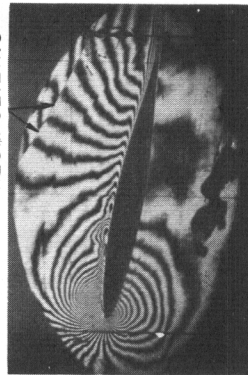
77.36

RUN 78

$\alpha = 10^\circ$

Re = 1,300,000

REFLECTED WAVE
FROM CEILING



s/c = 2.57

78.39

RUN 93

$\alpha = 15^\circ$

Re = 2,600,000



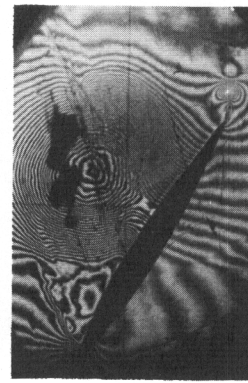
s/c = 2.68

93.33

RUN 95

$\alpha = 30^\circ$

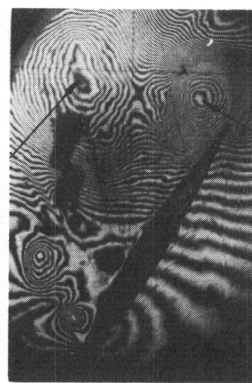
Re = 2,600,000



s/c = 2.69

95.12

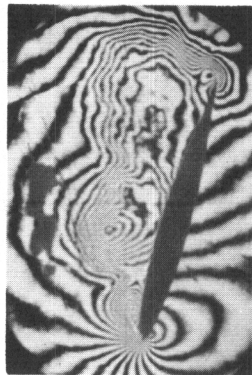
FIRST LEADING-EDGE VORTEX



SECOND TRAILING-EDGE VORTEX

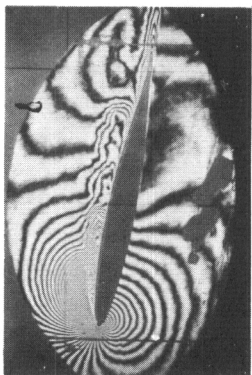
s/c = 3.93

95.27



s/c = 4.04

93.10



s/c = 3.82

78.44



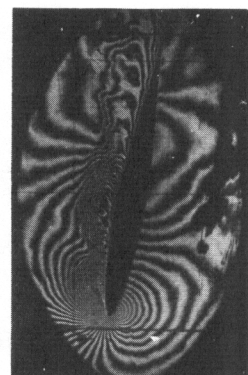
s/c = 5.85

103.40



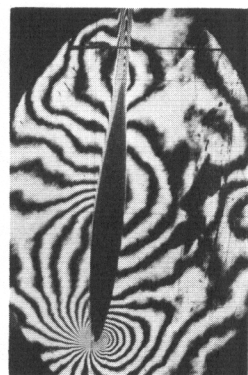
s/c = 5.98

104.10



s/c = 5.64

78.38



s/c = 6.05

77.32

FIG. 5 CONTINUED

Contours

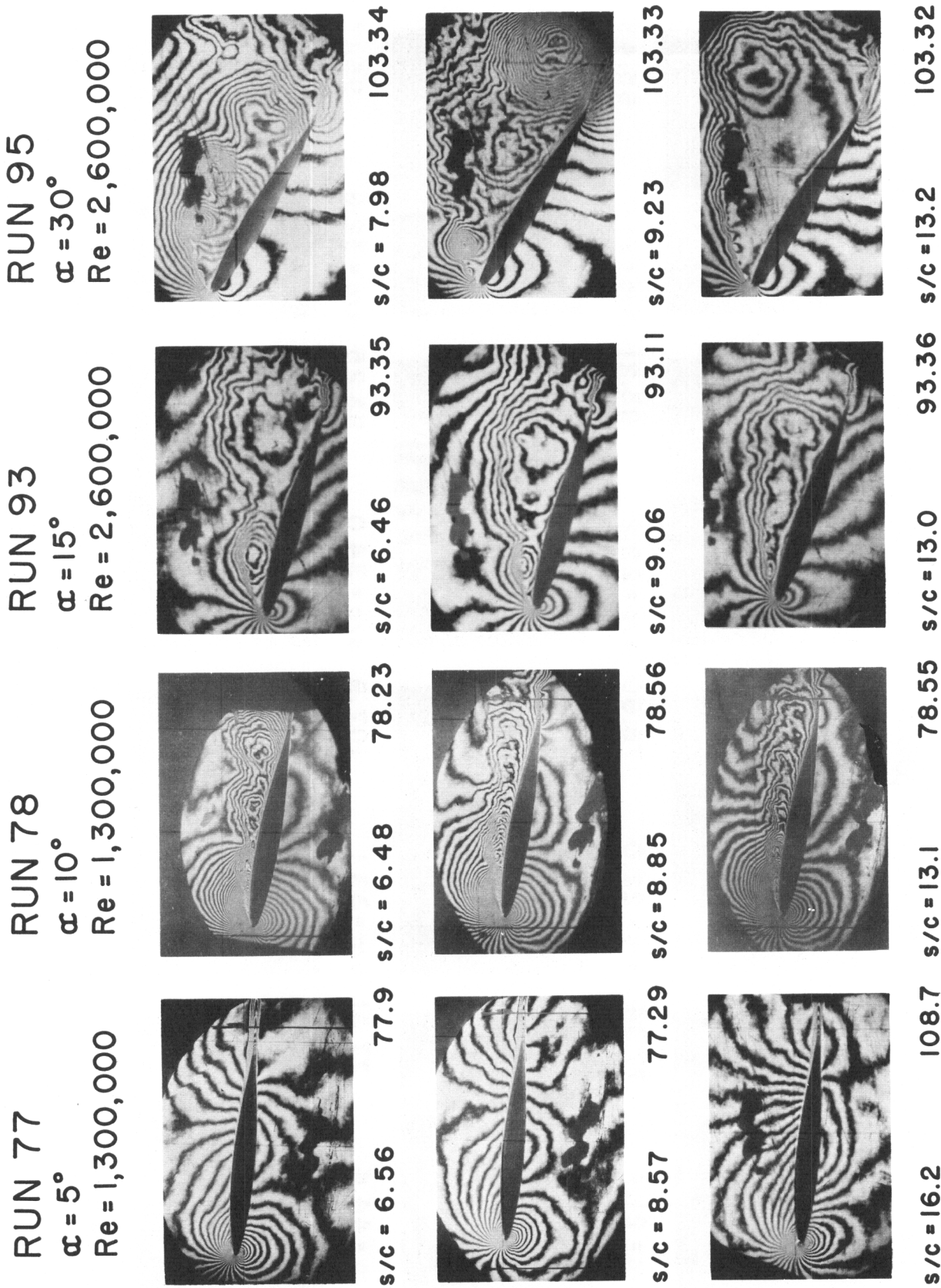


FIG. 5 CONTINUED

Contours

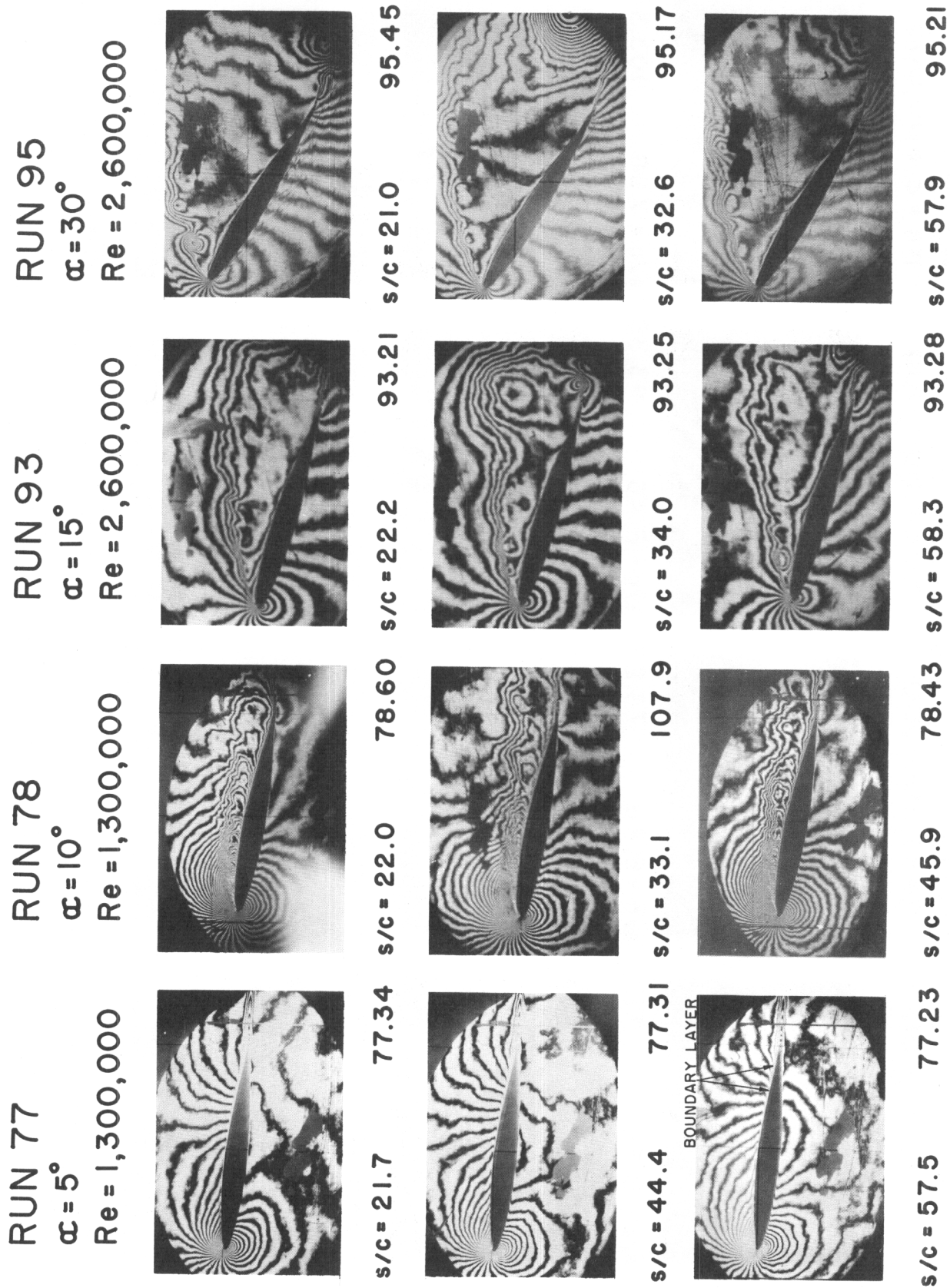


FIG. 5 CONTINUED

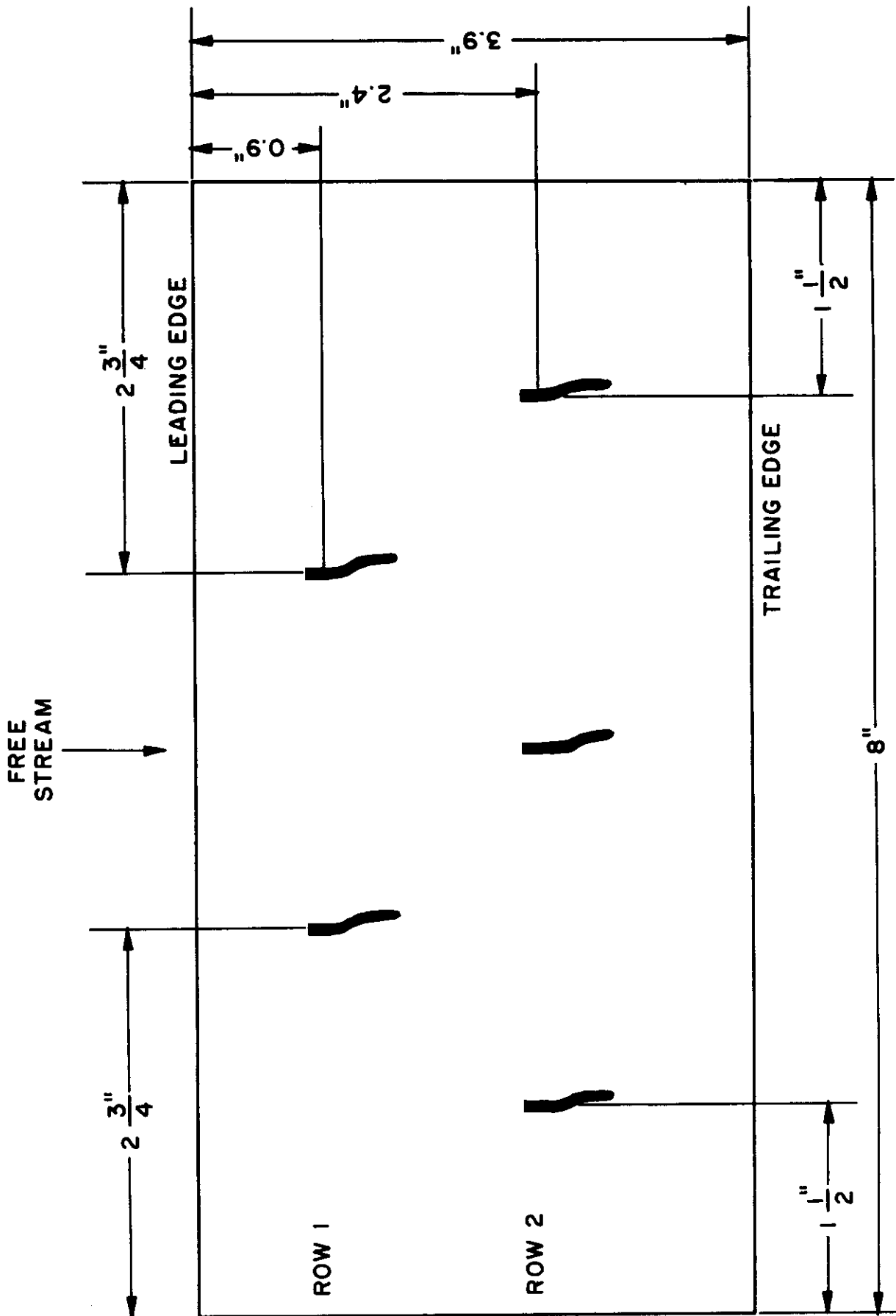


Fig. 6 Location of Tufts on the Upper Surface of the Airfoil

Contrails

L.E. BEGIN T.E.

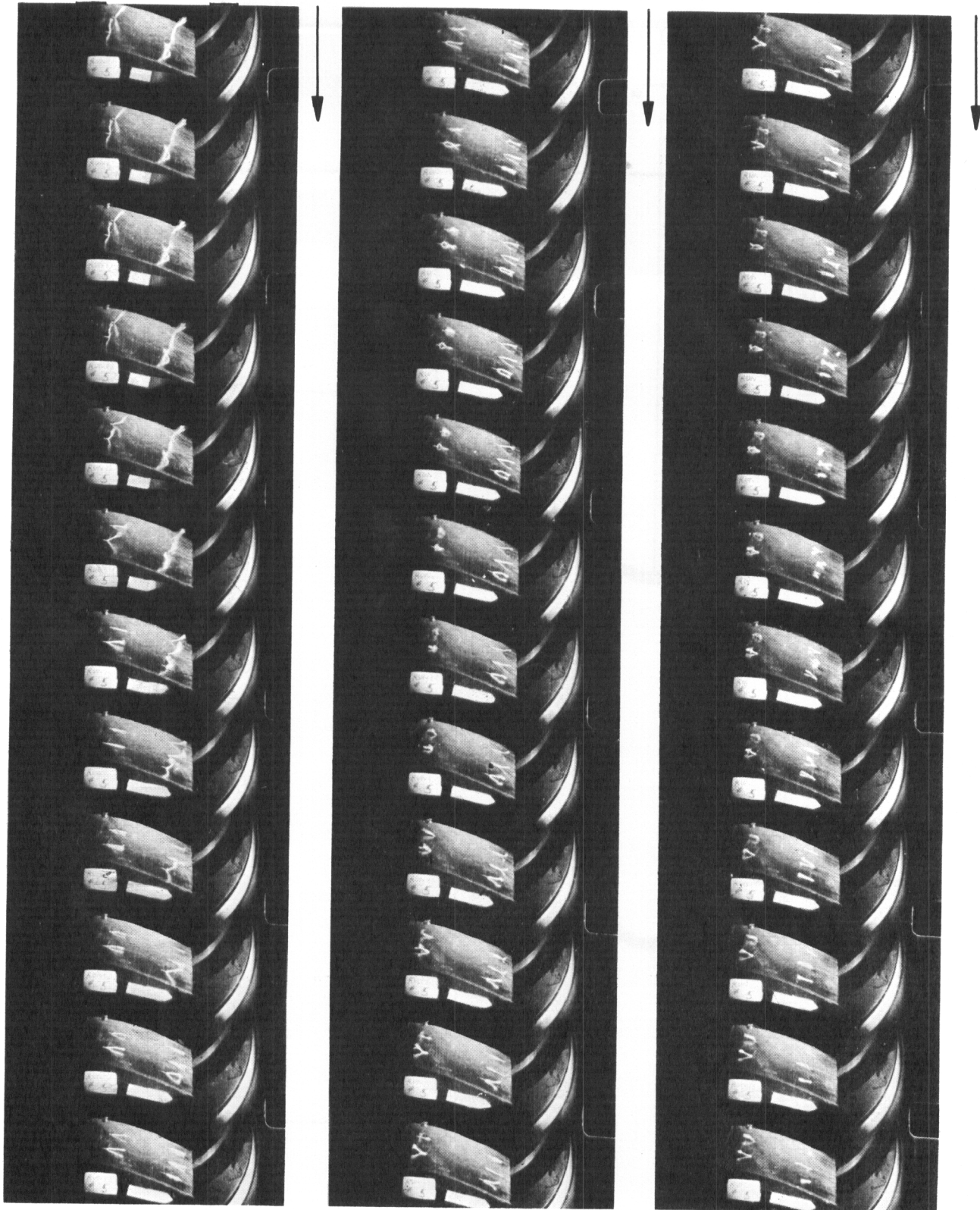


Fig. 7 Sample Photographic History of Tuft Behavior

$\alpha = 5^\circ$
s/c = 0.19

M = 0.4
Re = 1,300,000

RUN 77.22

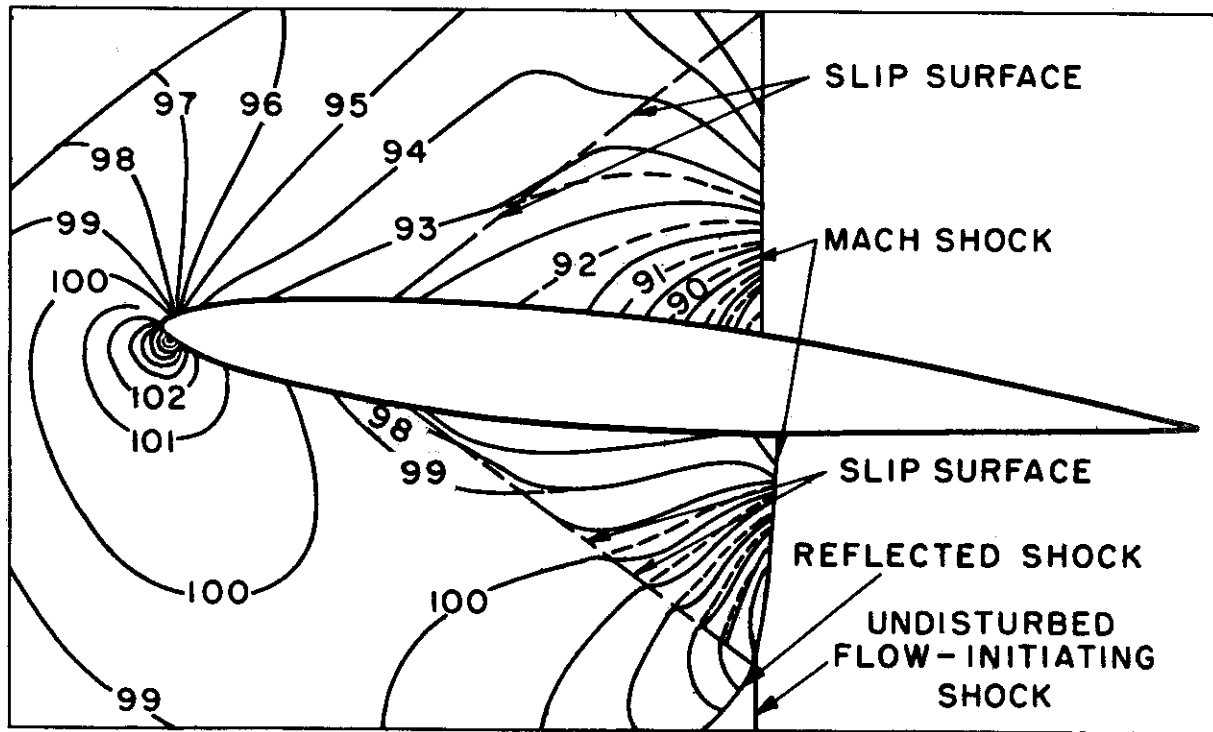
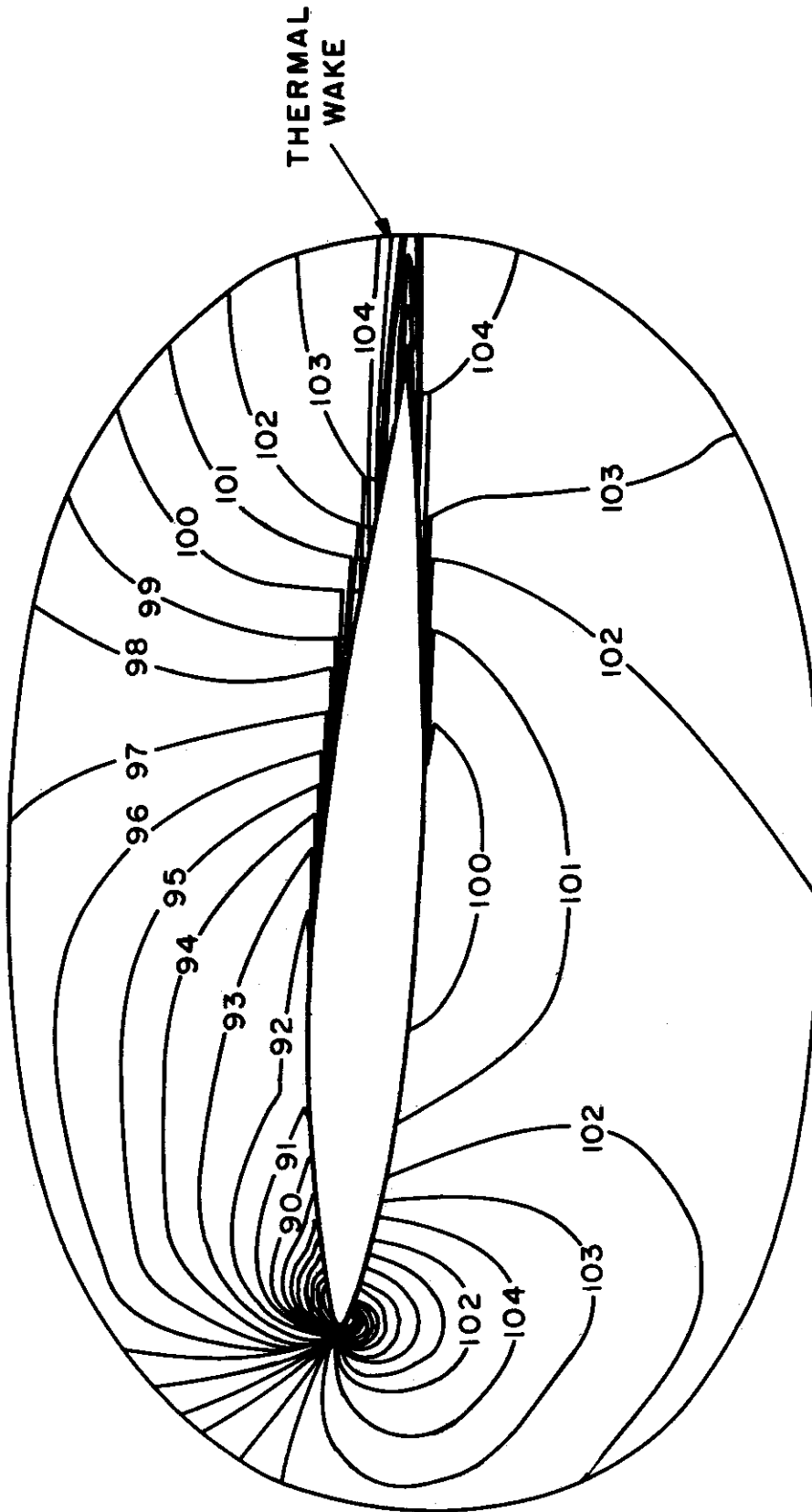


Fig. 8 Typical Interferogram during Diffraction-Loading Period

$\alpha = 5$ $M = 0.4$
 $s/c = 13.0$ $Re = 1,300,000$
RUN 77.10



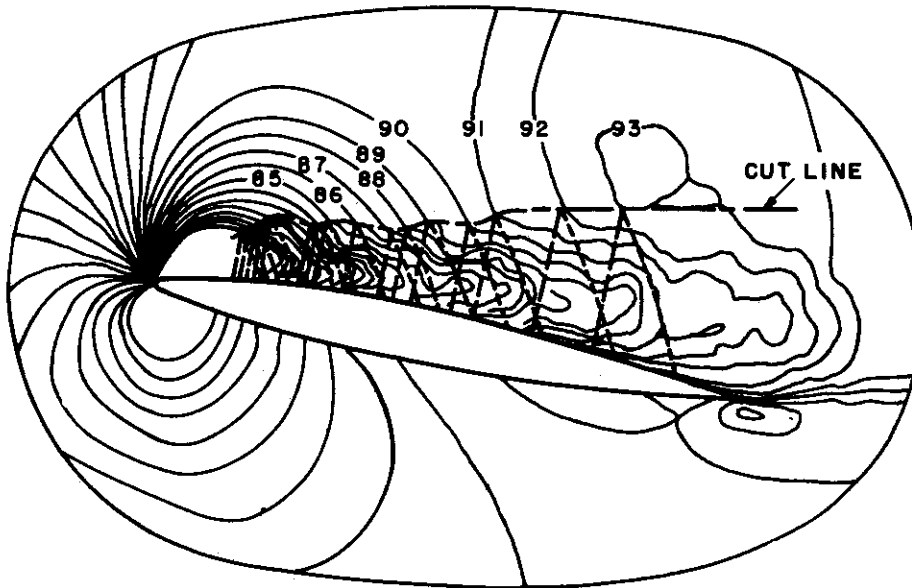
---- DENOTES ISOBAR EXTRAPOLATION

Fig. 9 Typical Interferogram of Potential-Type Steady-State Flow.

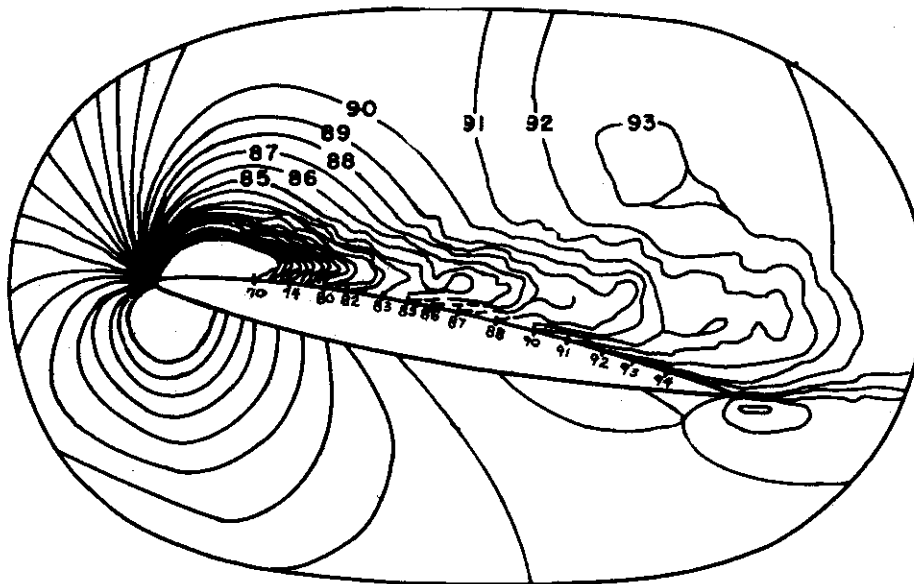
Contrails

--- EXTRAPOLATION A

--- EXTRAPOLATION B



(a) Extrapolations A and B



(c) Extrapolation C

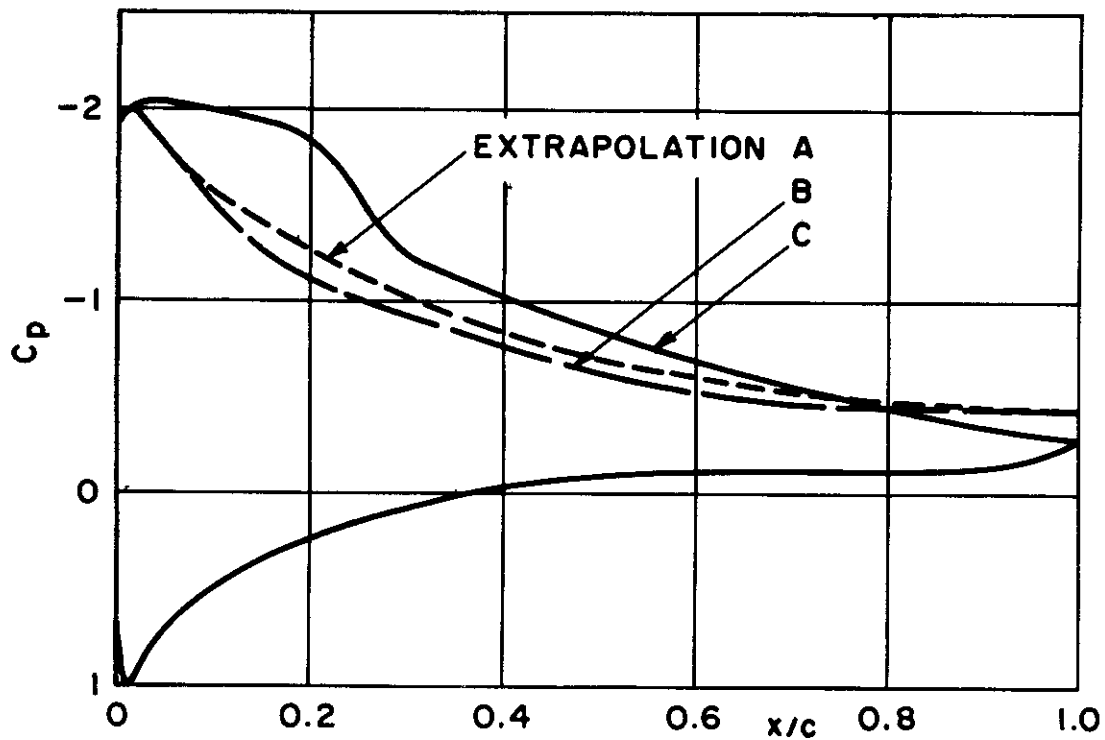
$\alpha = 10^\circ$
s/c = 34.0

M = 0.4
Re = 1,290,000

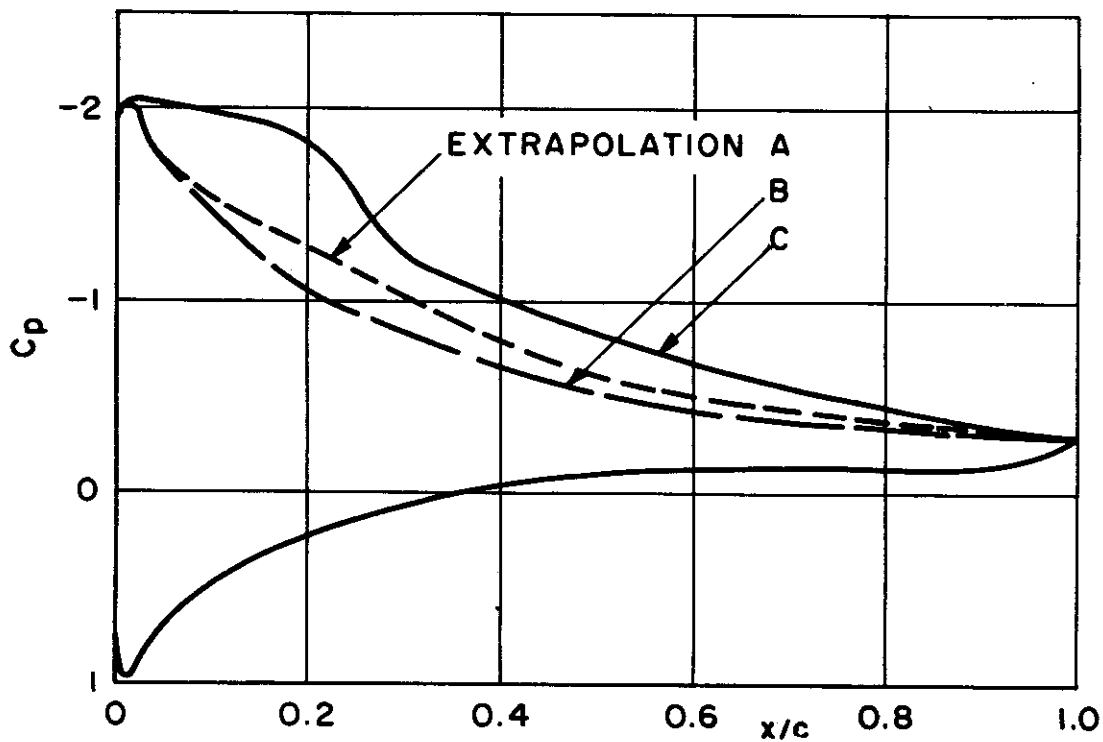
RUN 78.27

Fig. 10 Typical Interferogram of Steady-State Nearly-Stalled Flow

Contrails



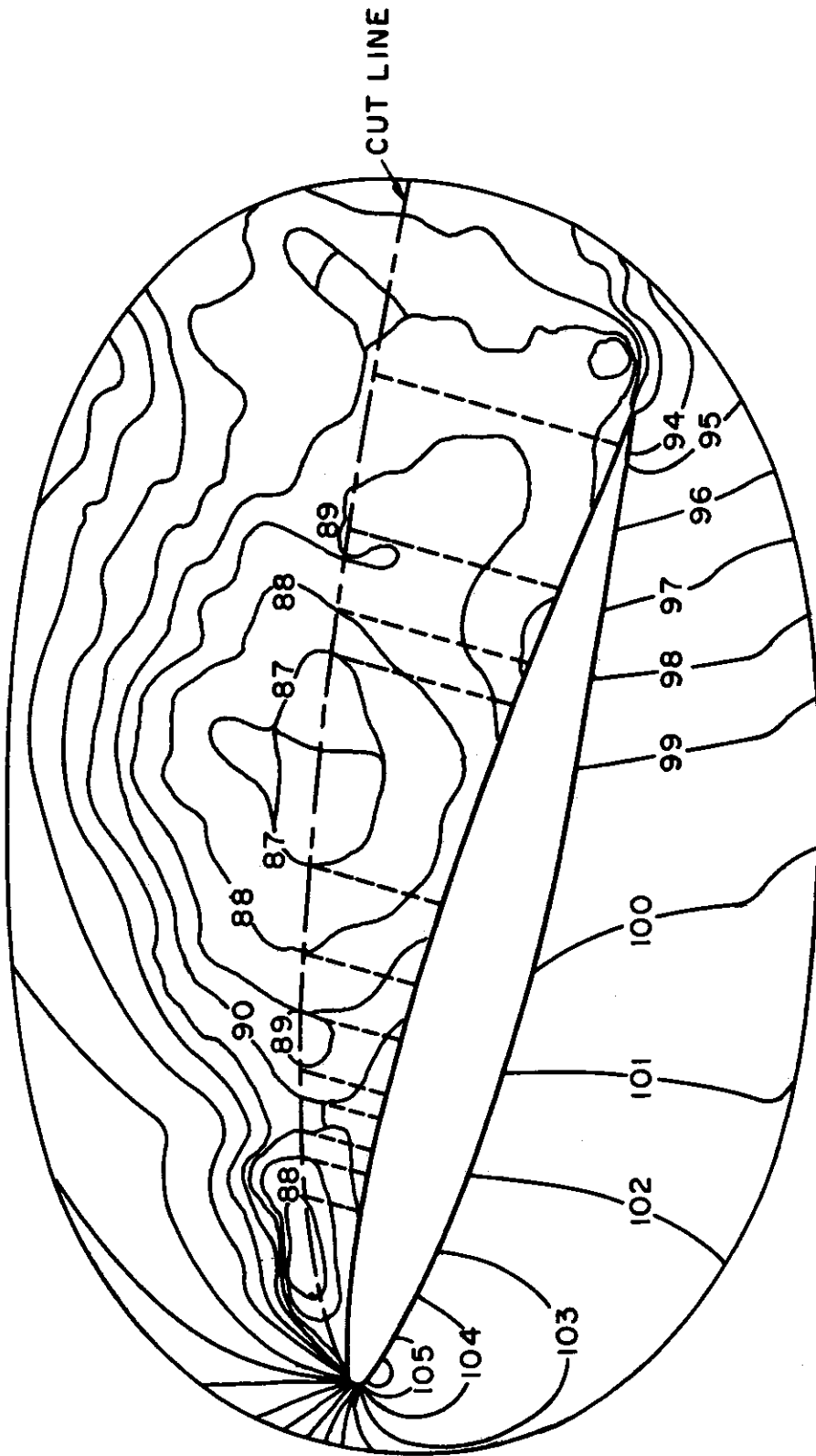
(a) Uncorrected for Trailing-Edge Discrepancy



(b) Corrected for Trailing-Edge Discrepancy

Fig. 11 Chordwise Pressure Distributions for the Fig. 10 Flow Pattern

$\alpha = 15^\circ$
s/c = 6.02
M2 = 0.4
Re = 580,000
RUN 93.20



--- DENOTES ISOBAR EXTRAPOLATION

Fig. 12a Typical Interferogram of Transiently Stalled Flow -- Interpretation A

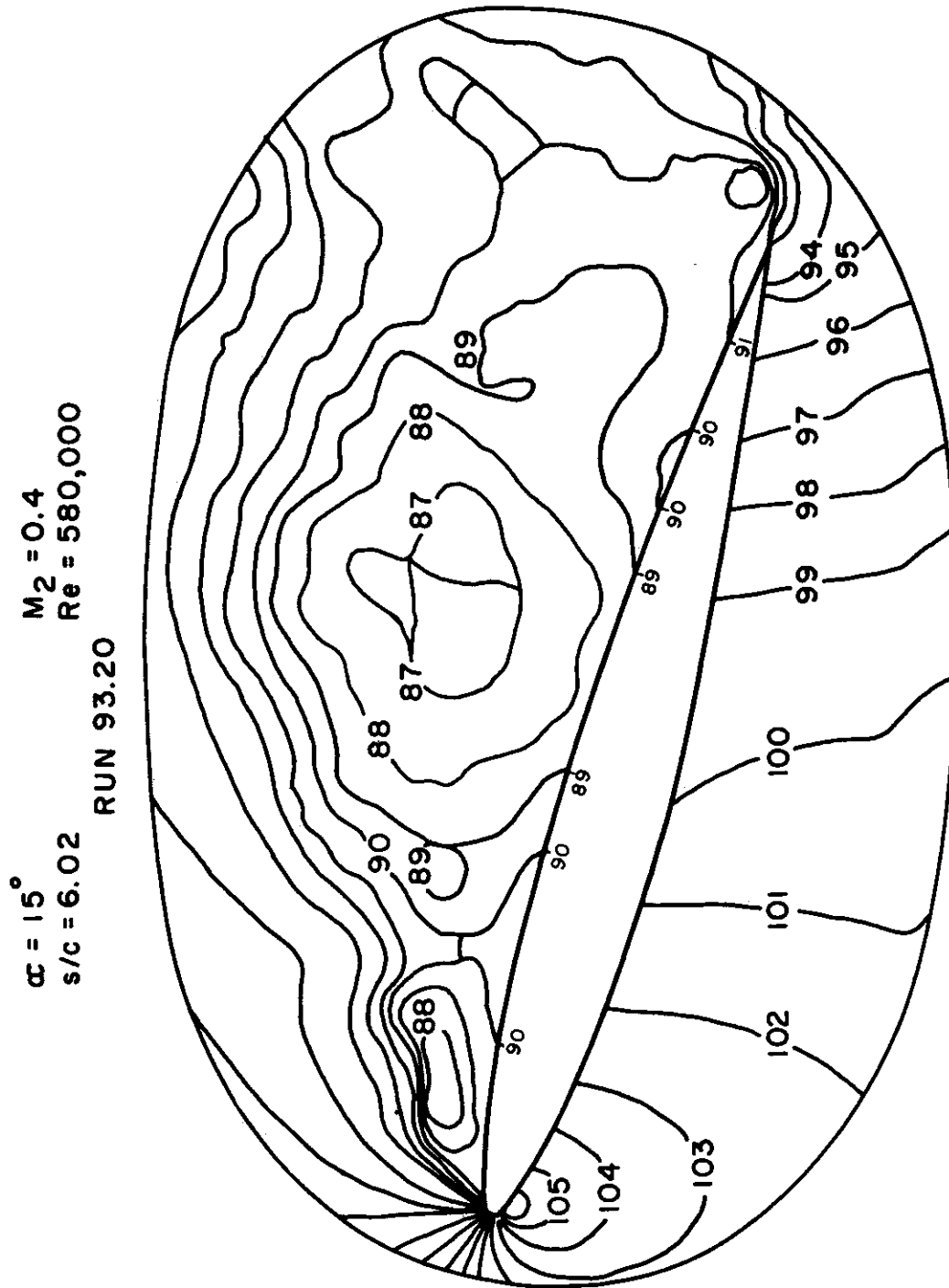
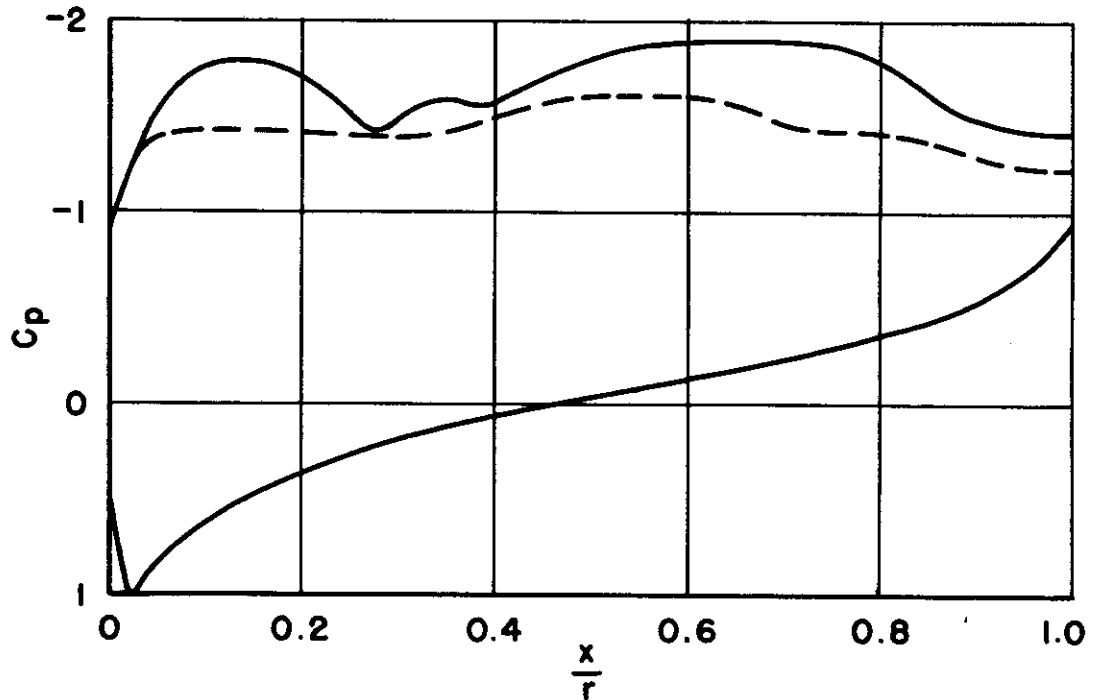


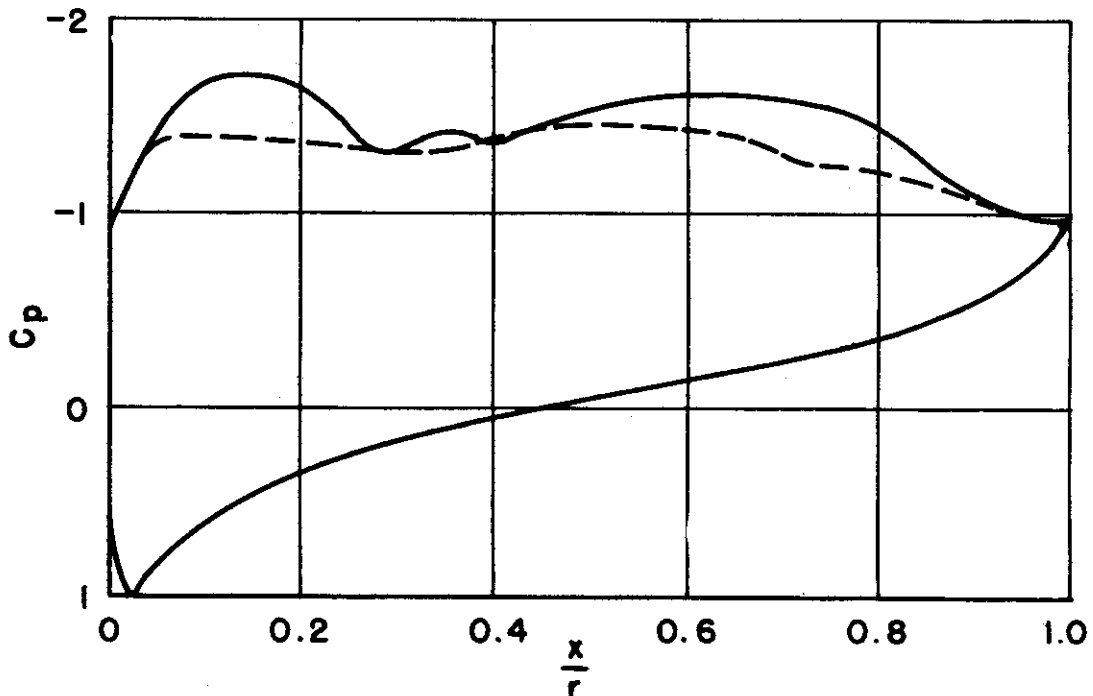
Fig. 12b Typical Interferogram of Transiently Stalled Flow -- Interpretation B

CUT-LINE METHOD ———

SURFACE INTERSECTION METHOD - - - -



(a) Uncorrected for Trailing-Edge Discrepancy



(b) Corrected for Trailing-Edge Discrepancy

Fig. 13 Chordwise Pressure Distributions for the Fig. 12 Flow Pattern

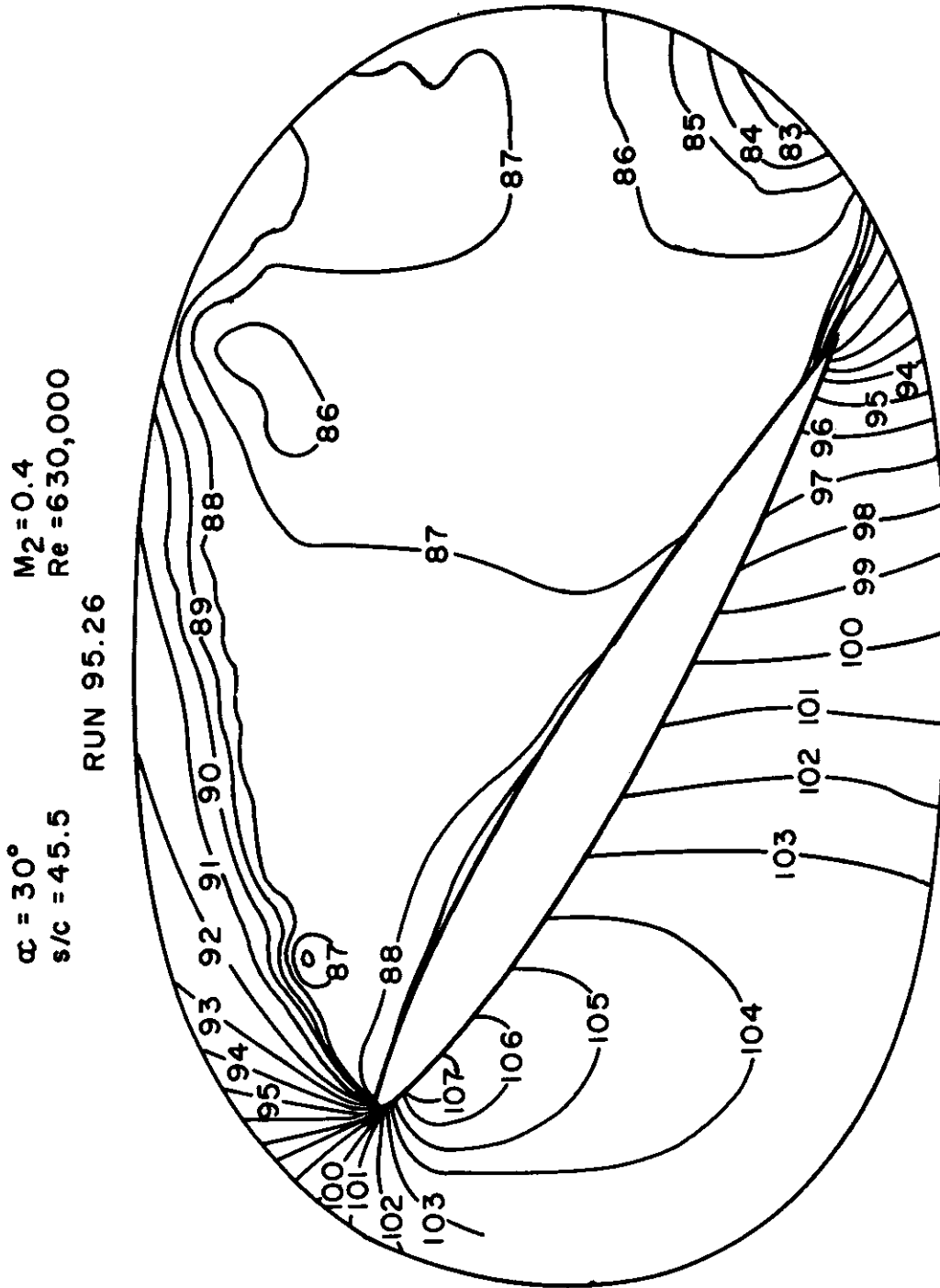


Fig. 14 Typical Interferogram of Steady-State Stalled Flow

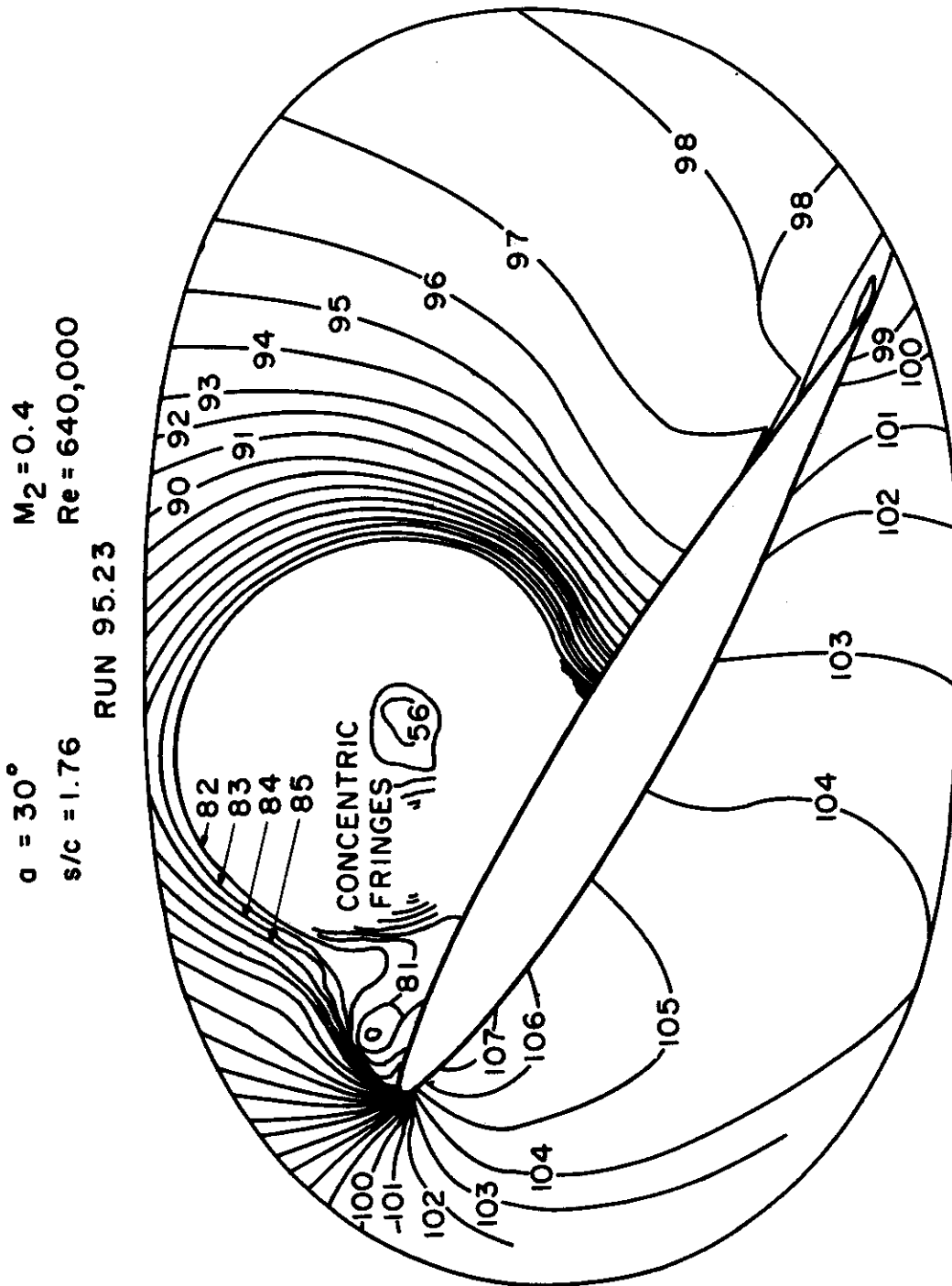


Fig. 15 Typical Interferogram with Vortex Starting from the Nose.

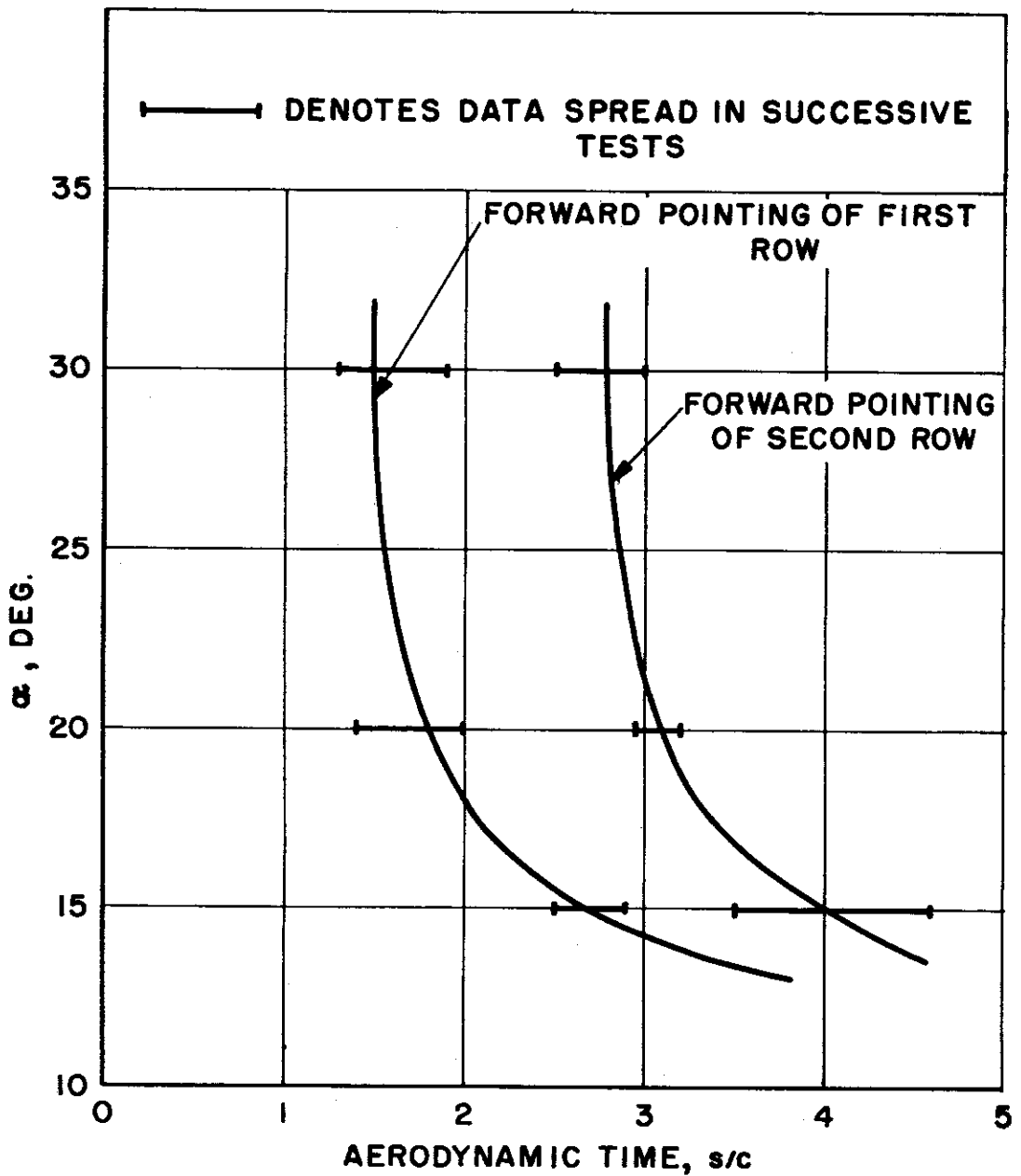


Fig. 16 Characteristic Time of Tuft-Indicated Flow Reversal as a Function of Angle-of-Attack

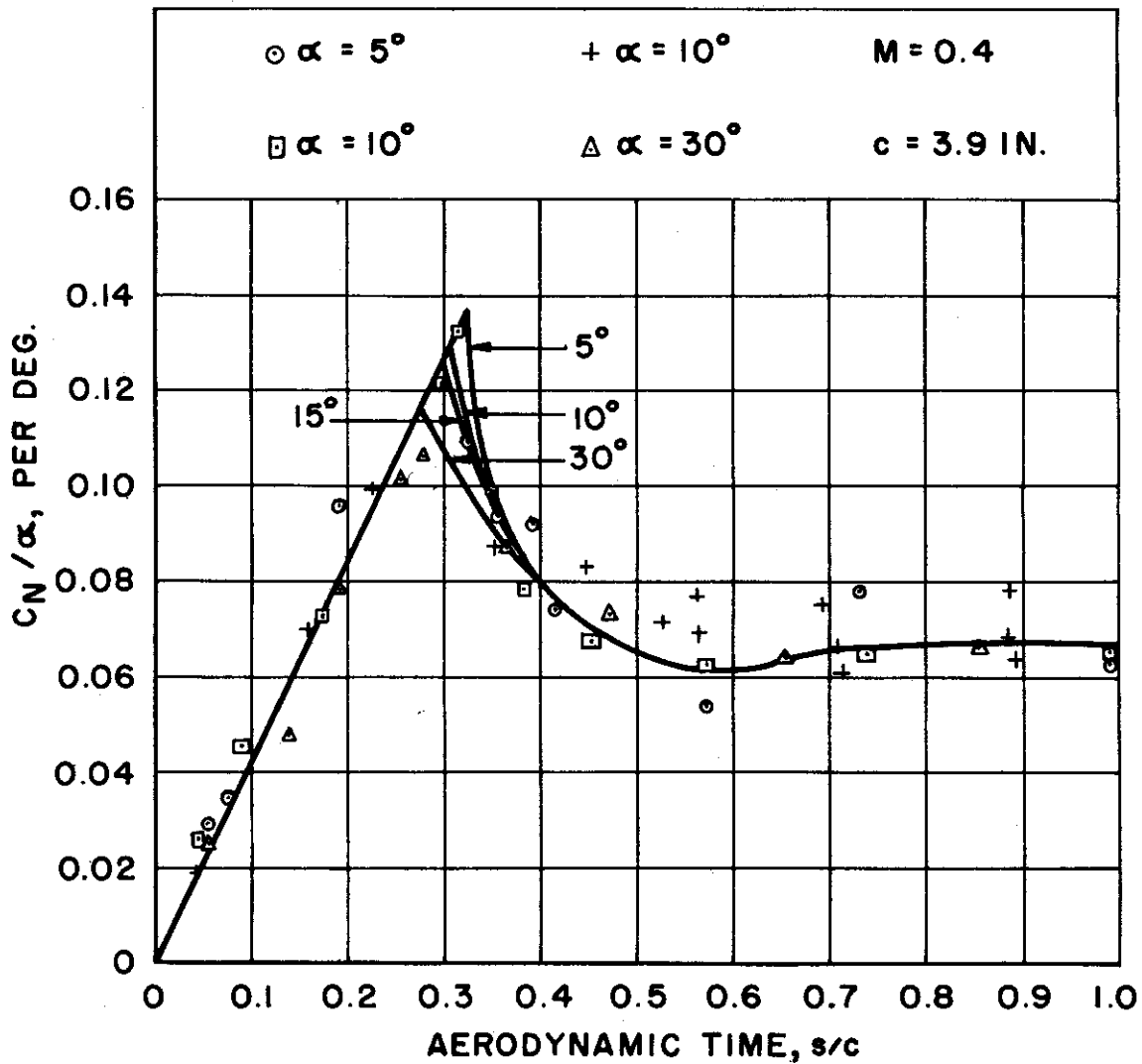


Fig. 17 Histories of Ratio of Normal-Force Coefficient to Angle-of-Attack during the Diffractive-Flow Period

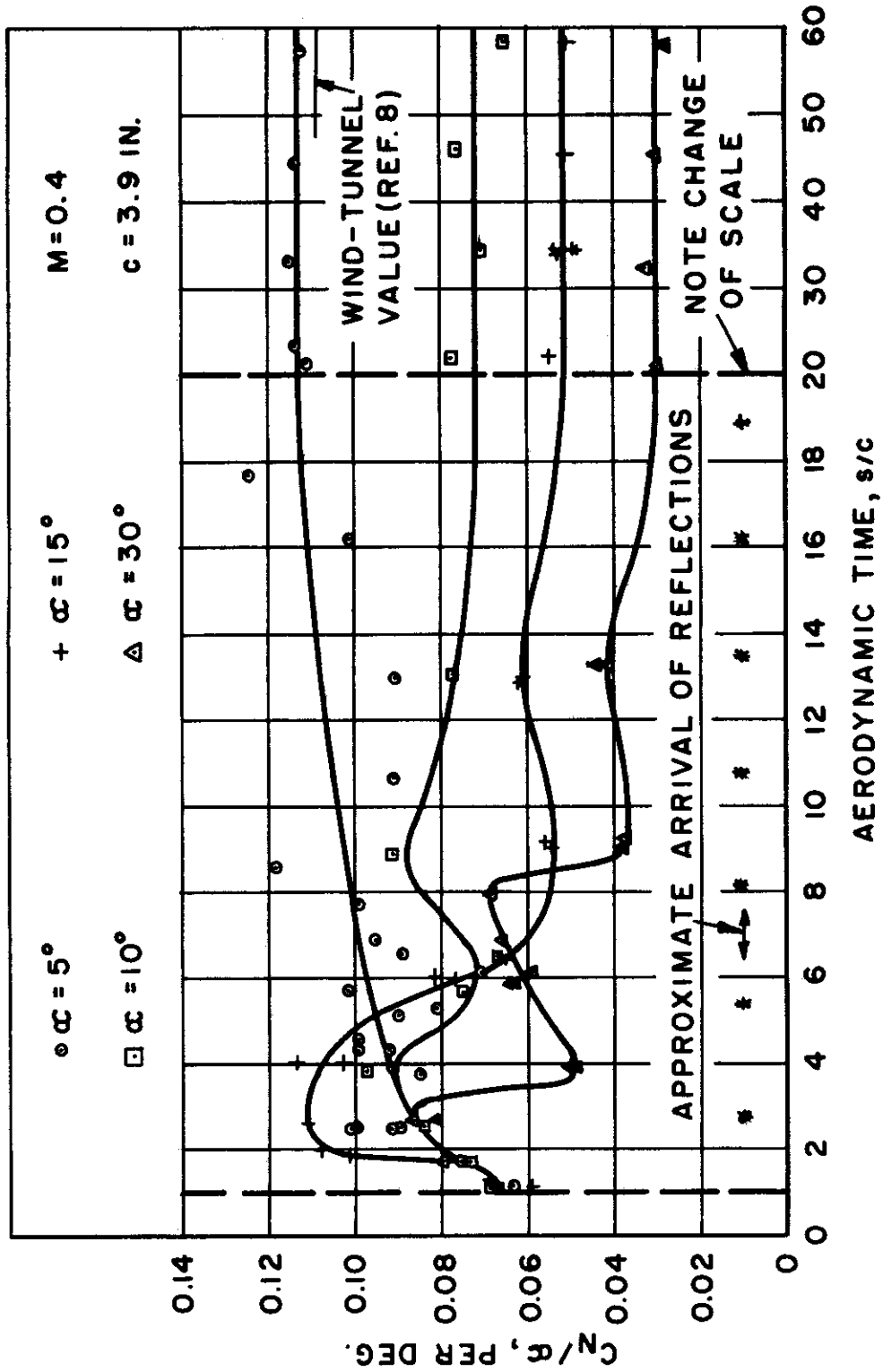


Fig. 18 Histories of Ratio of Normal-Force Coefficient to Angle-of-Attack during the Post-Diffraction Period.

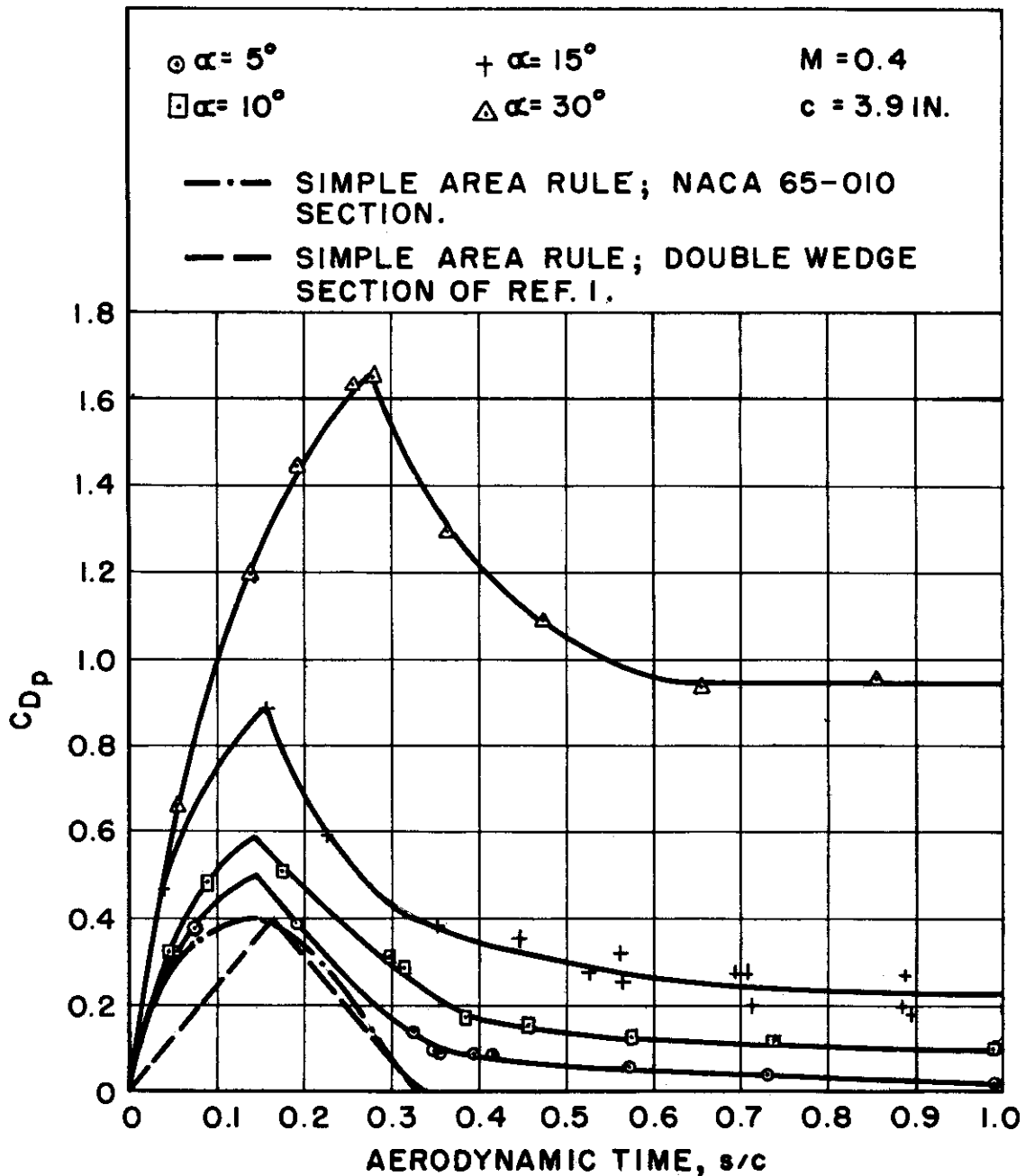


Fig. 19 Pressure-Drag Coefficient History during the Diffractive-Flow Period

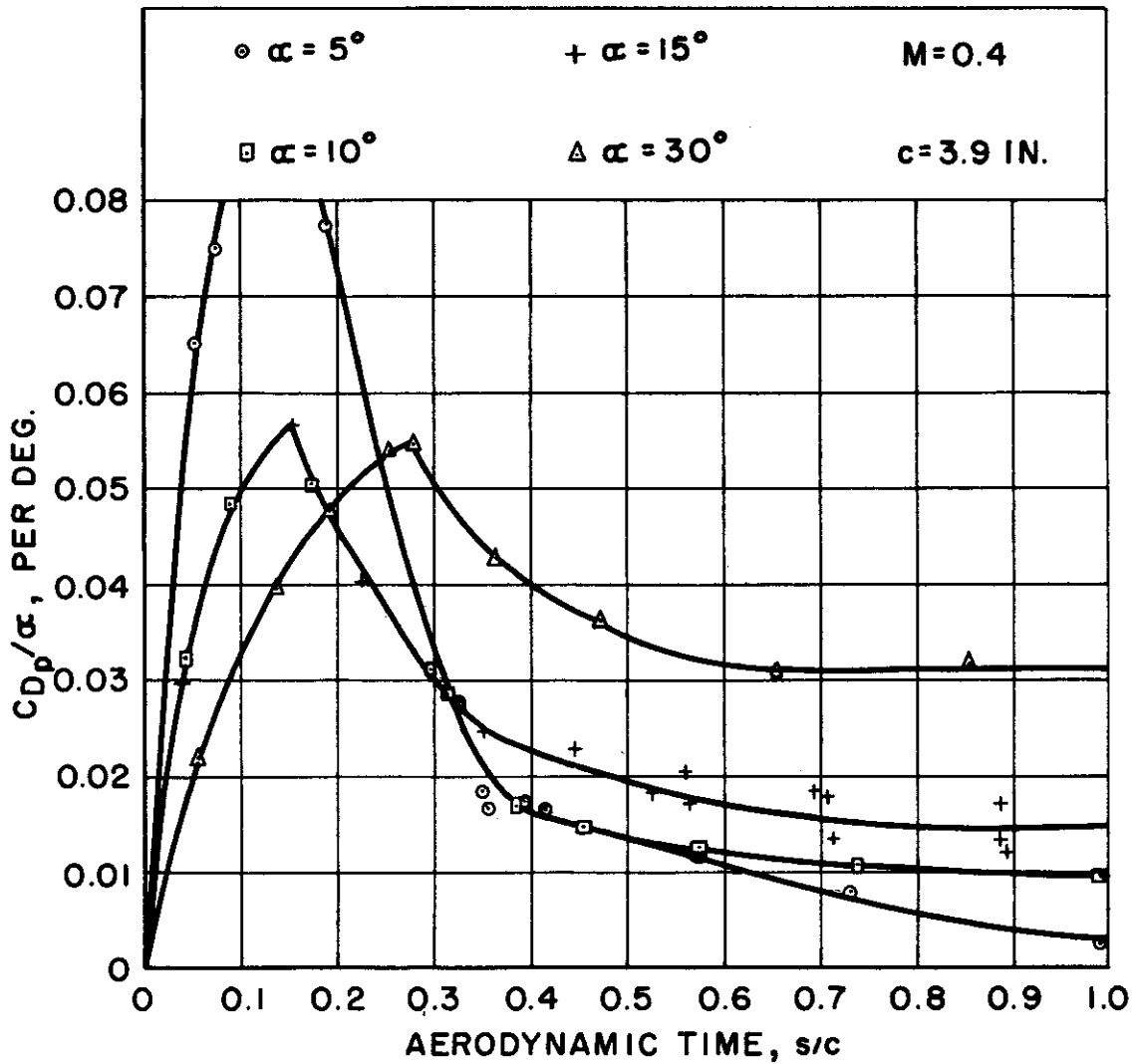


Fig. 20 Histories of the Ratio of Pressure-Drag Coefficient to Angle-of-Attack during the Diffractive-Flow Period

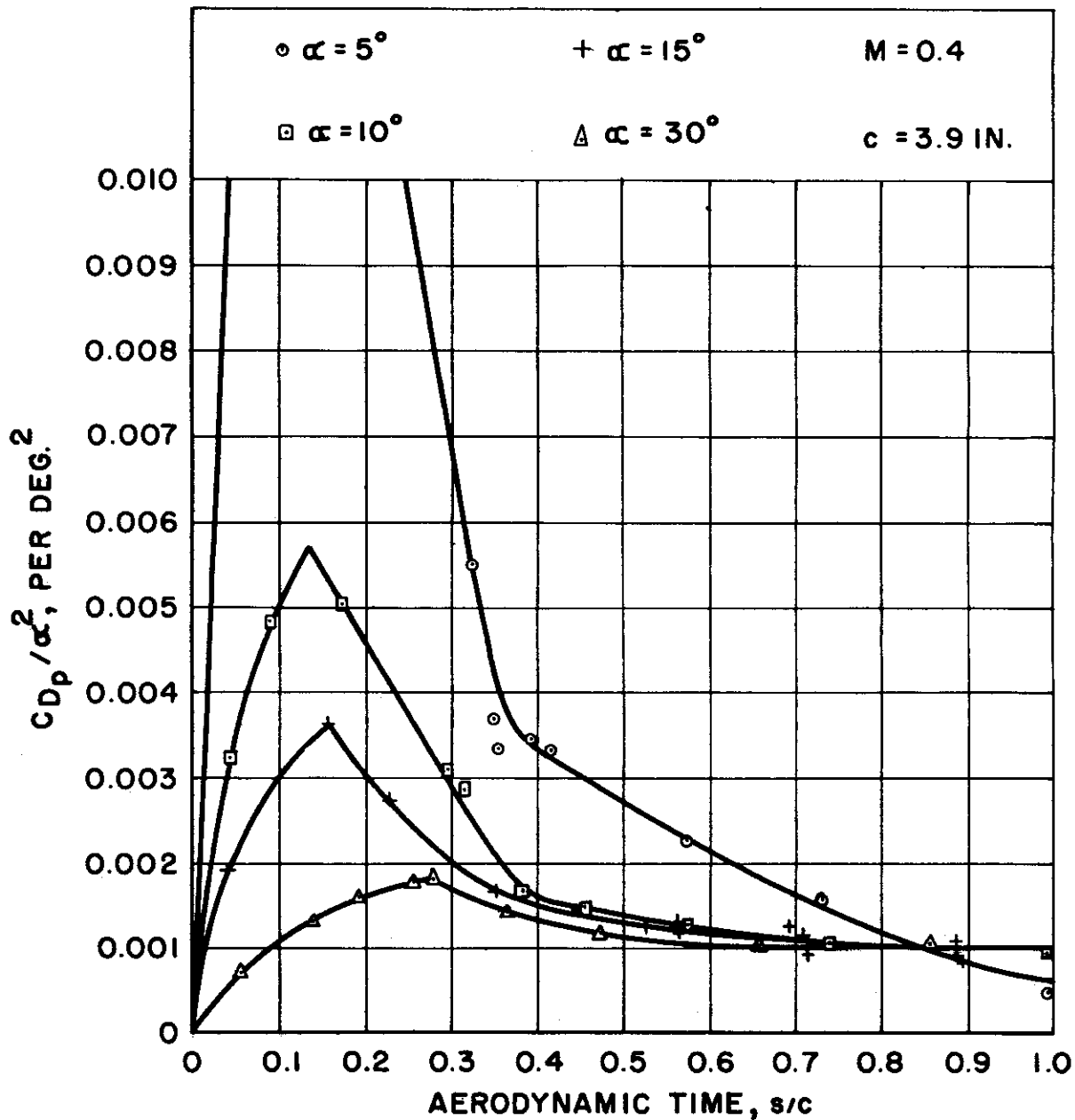


Fig. 21 Histories of the Ratio of Pressure-Drag Coefficient to Angle-of-Attack Squared during the Diffractive-Flow Period

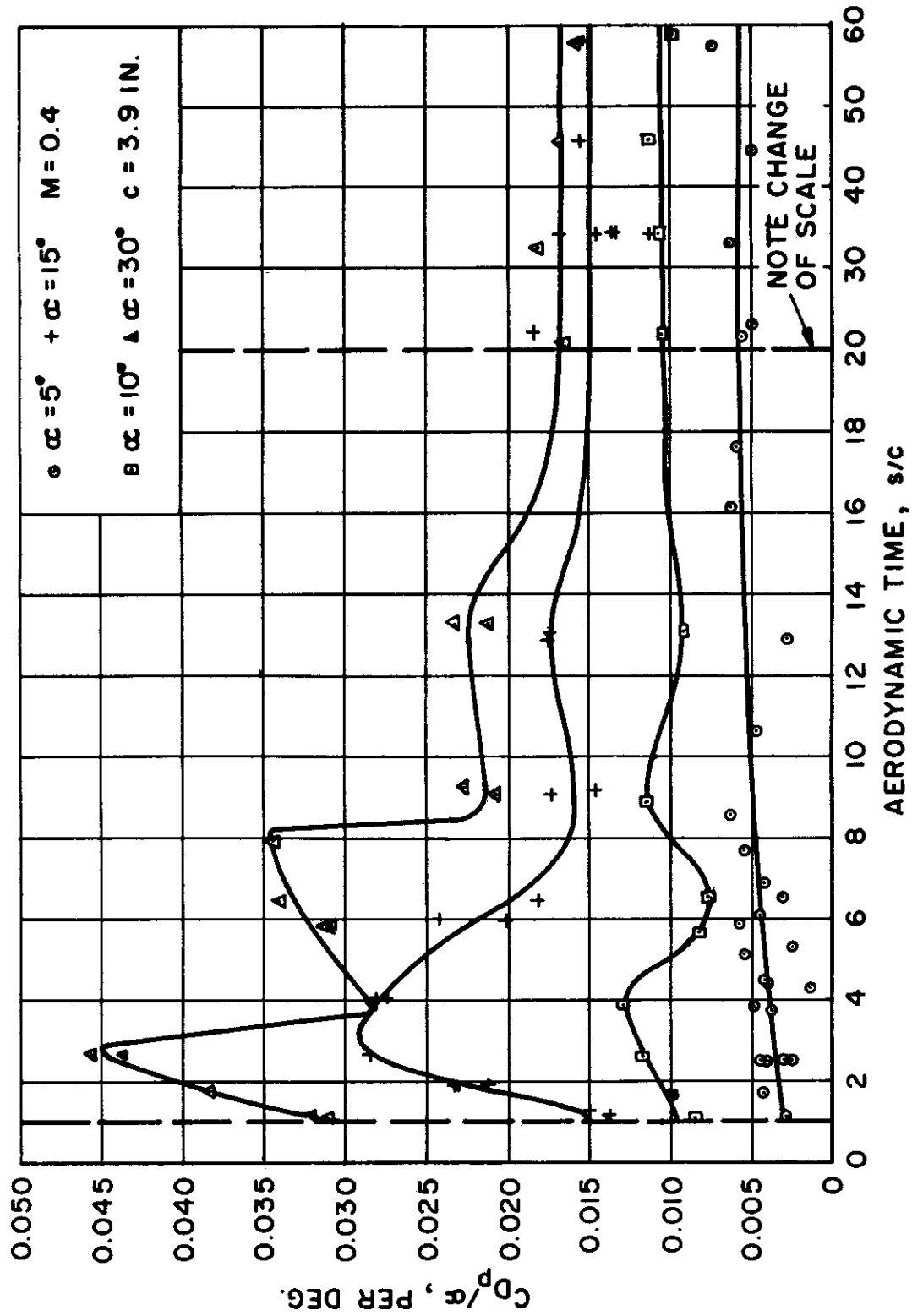


Fig. 22 Histories of the Ratio of Pressure-Drag Coefficient to Angle-of-Attack during the Post-Diffraction Flow Period

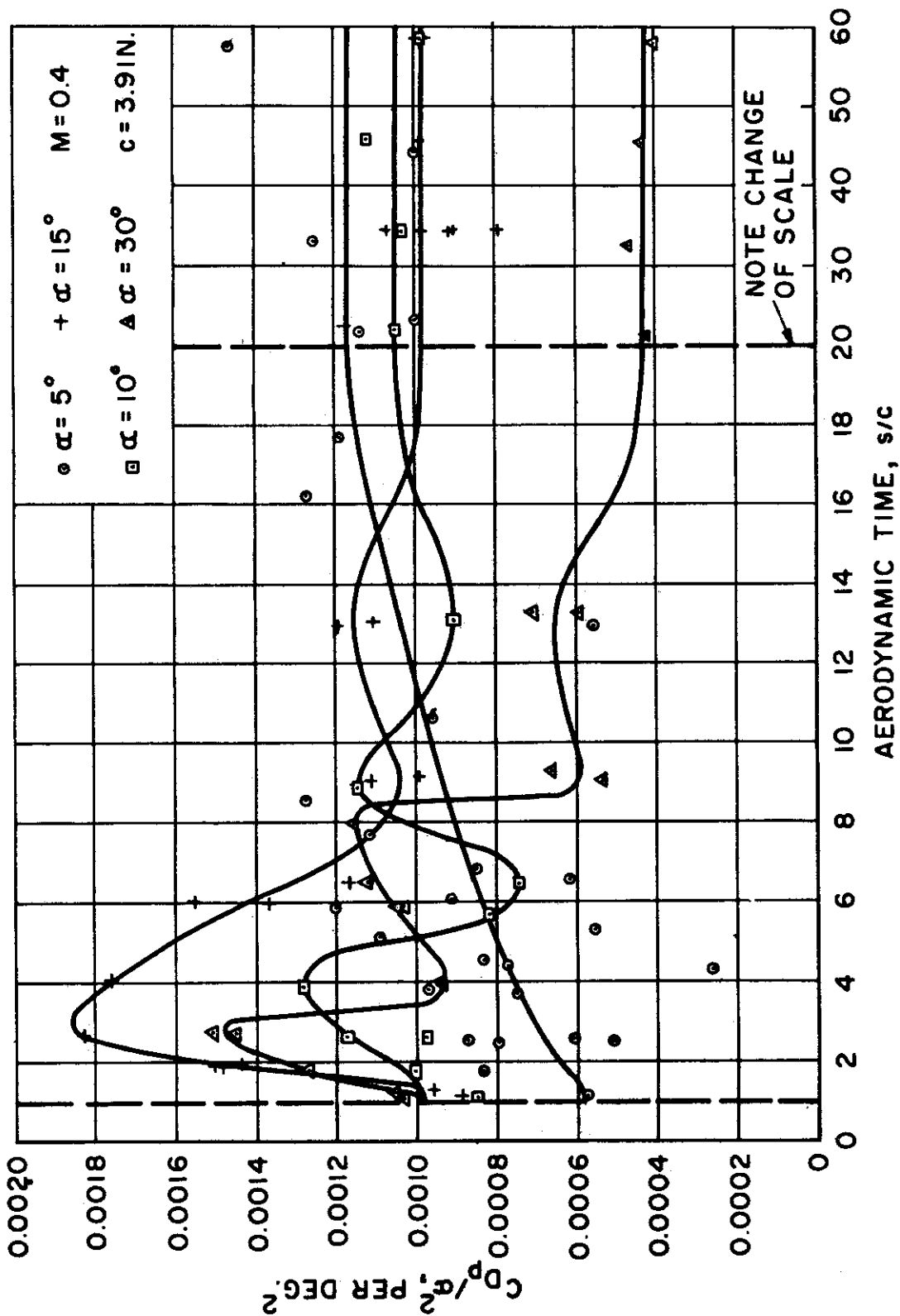


Fig. 23 Histories of the Ratio of Pressure-Drag Coefficient to Angle-of-Attack Squared during the Post-Diffractive Flow Period

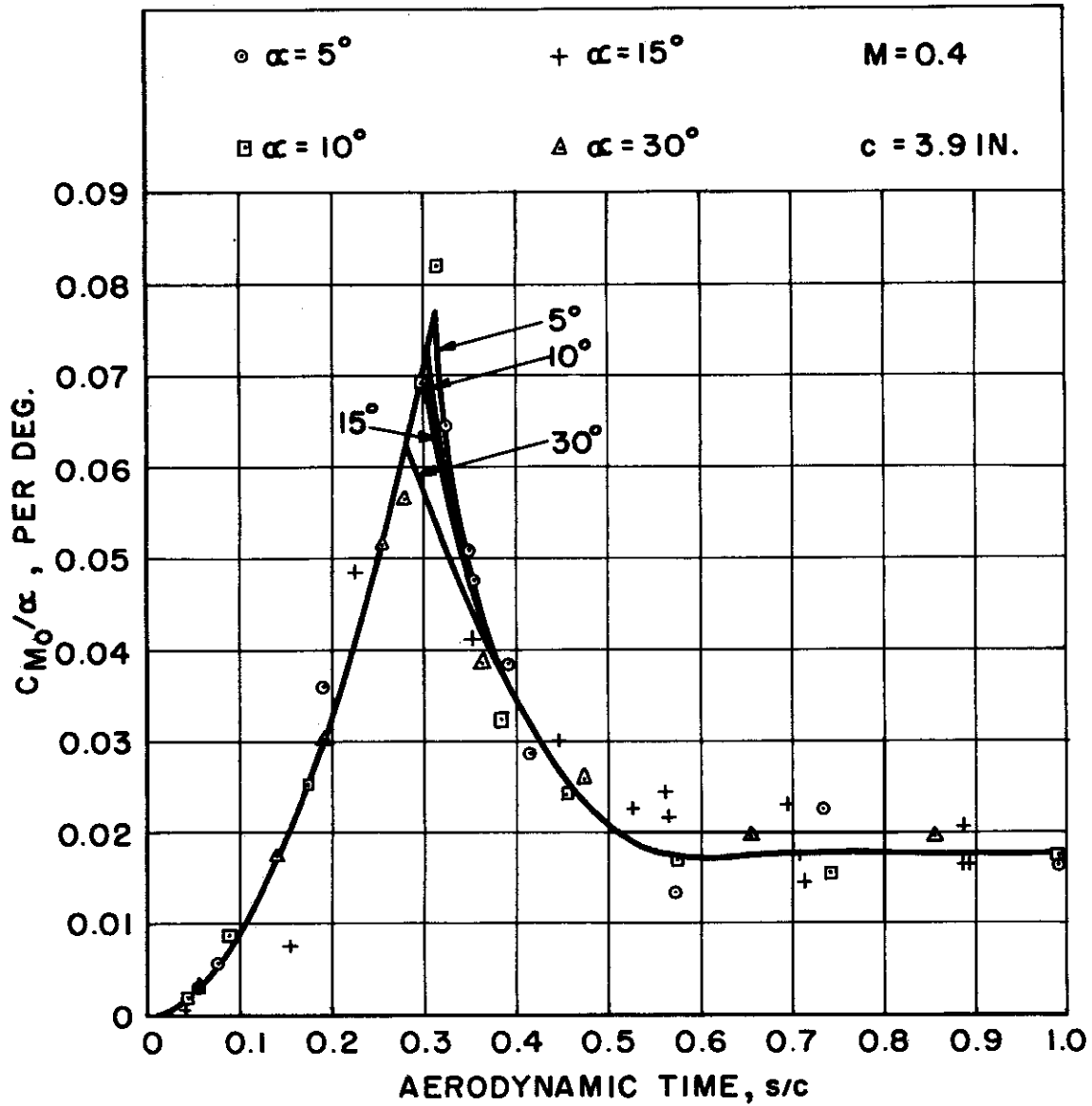


Fig. 24 Histories of the Ratio of Moment Coefficient about the Leading Edge to Angle-of-Attack during the Diffractive-Flow Period

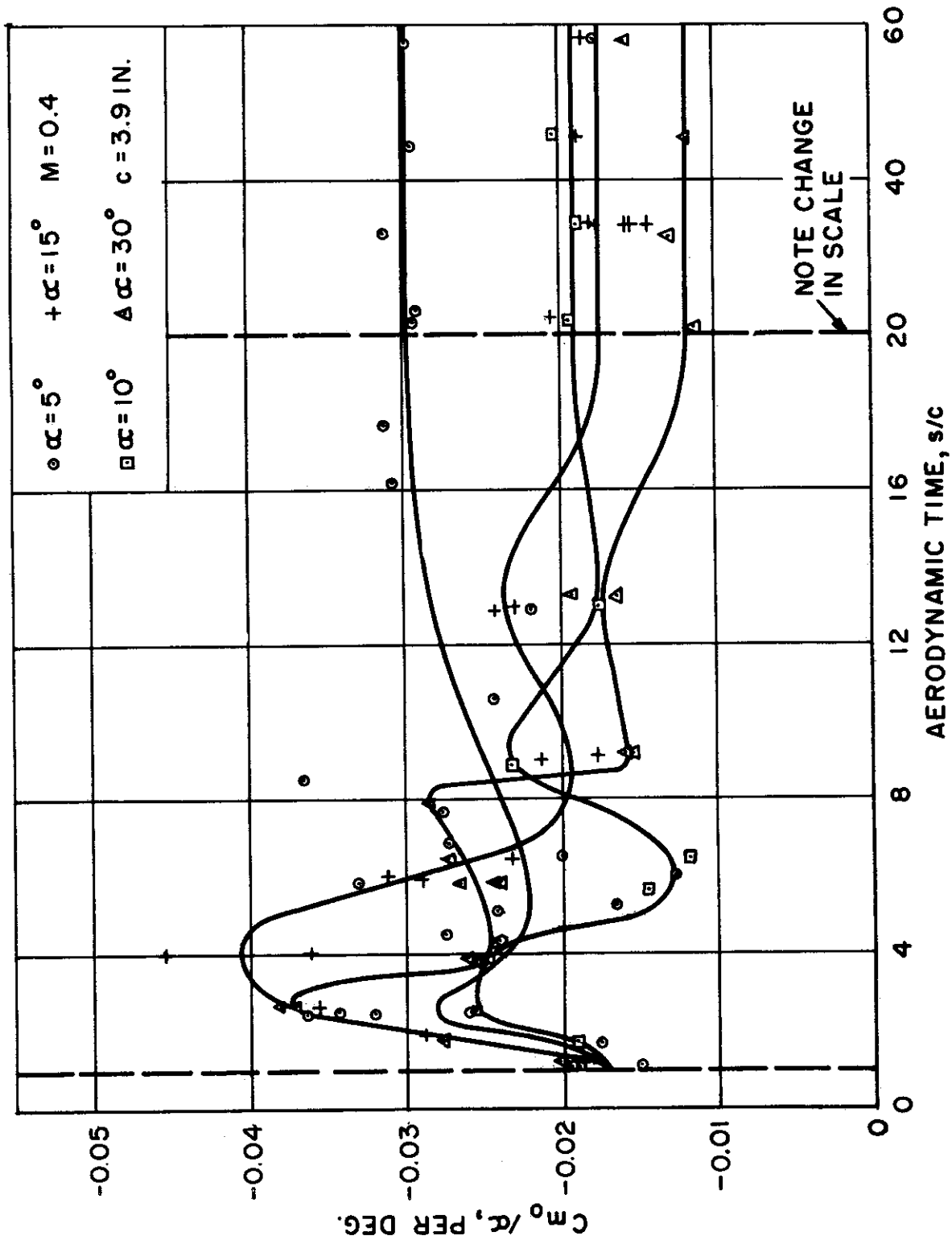


Fig. 25 Histories of The Ratio of Moment Coefficient about the Leading Edge to Angle-of-Attack during the Post-Diffraction Flow Period.

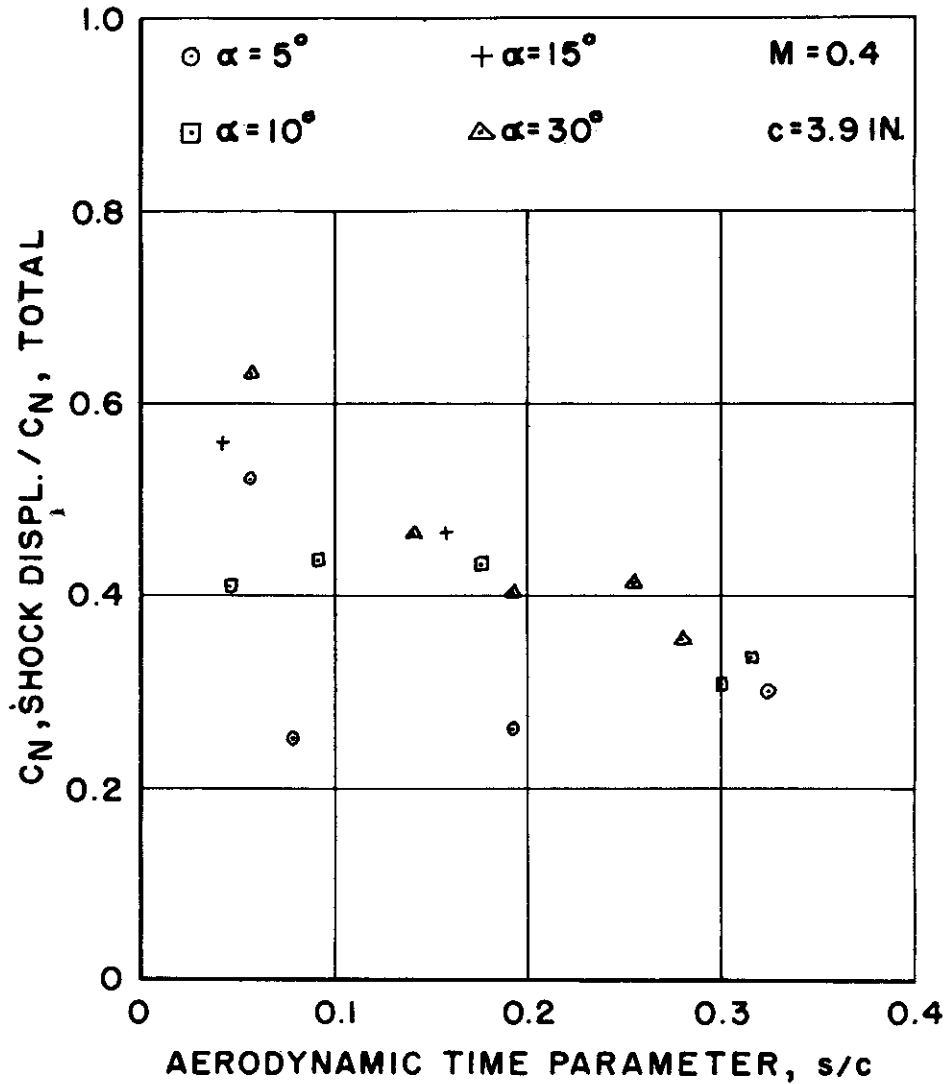
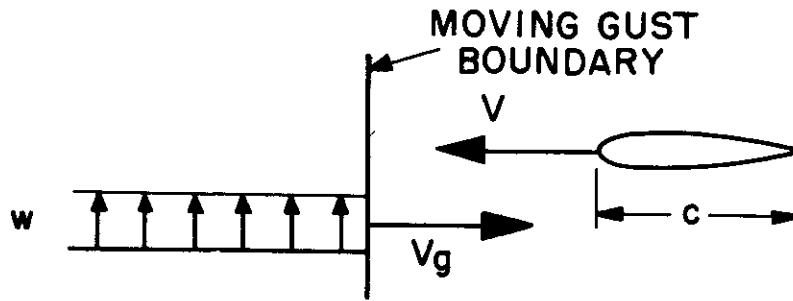
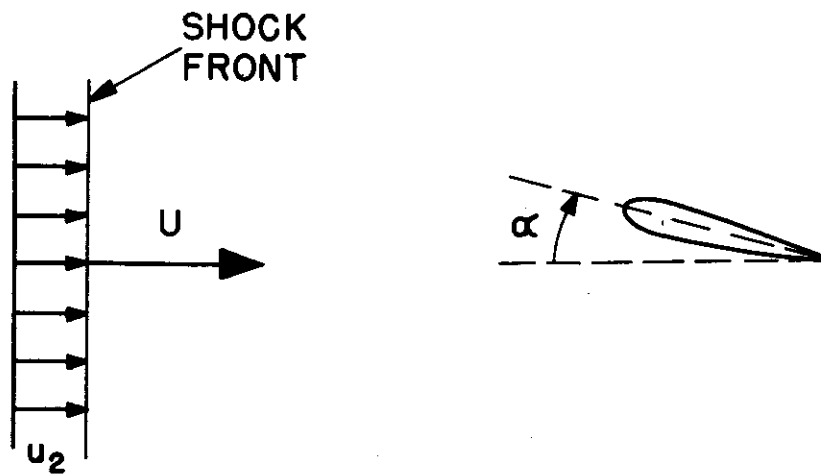


Fig. 26 Contribution to C_N Due to Chordwise Displacement of Top- and Bottom-Surface Shocks



(a) Moving-Gust Flow Model



(b) Shock-Tube Flow Model

Fig. 27 Illustration of Moving-Gust Flow Model and Idealized Shock-Tube Flow Model

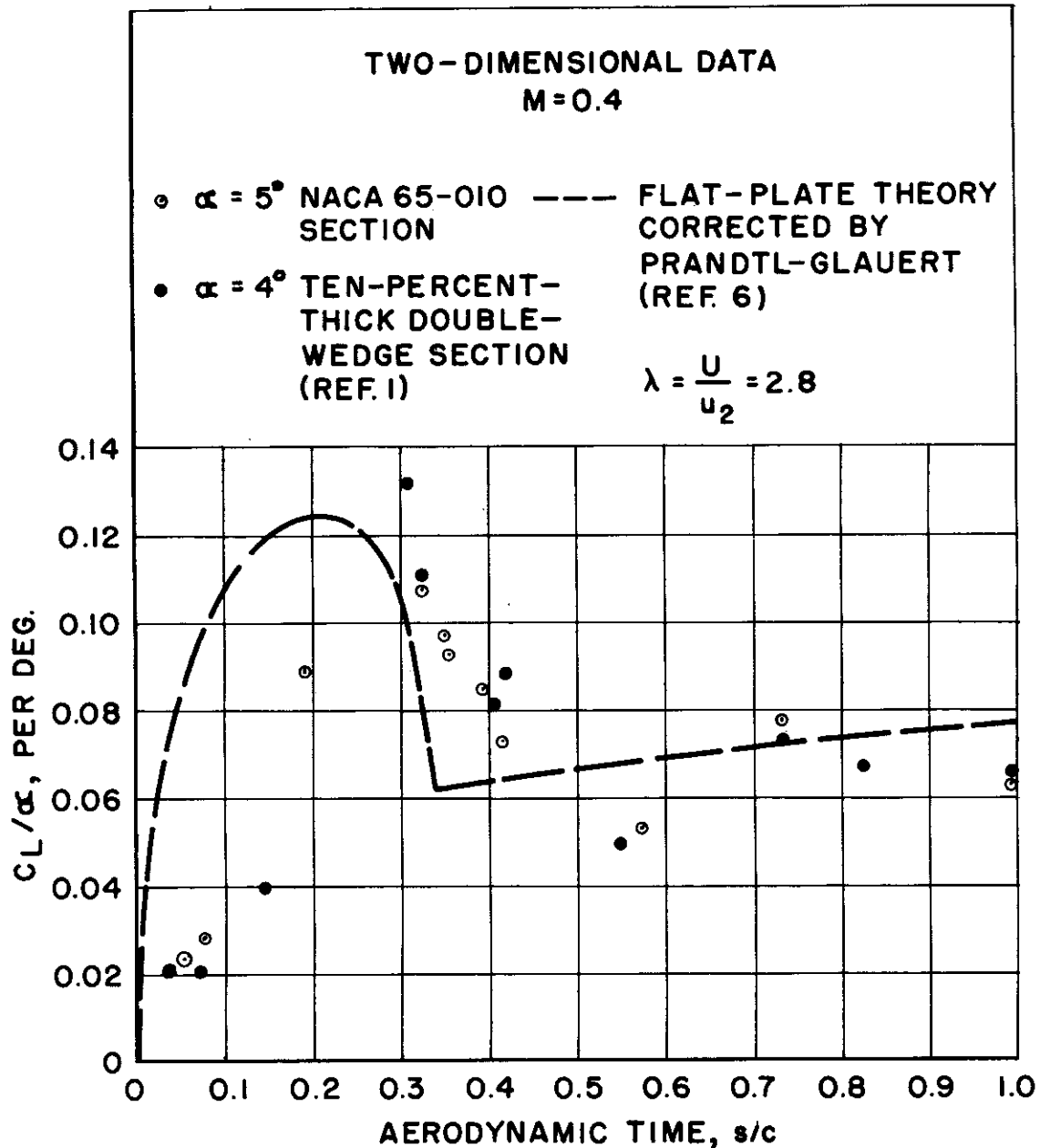


Fig. 28 Comparisons of Theoretical and Experimental Variations of the Ratio of Lift Coefficient to Angle-of-Attack during the Diffractive-Flow Period

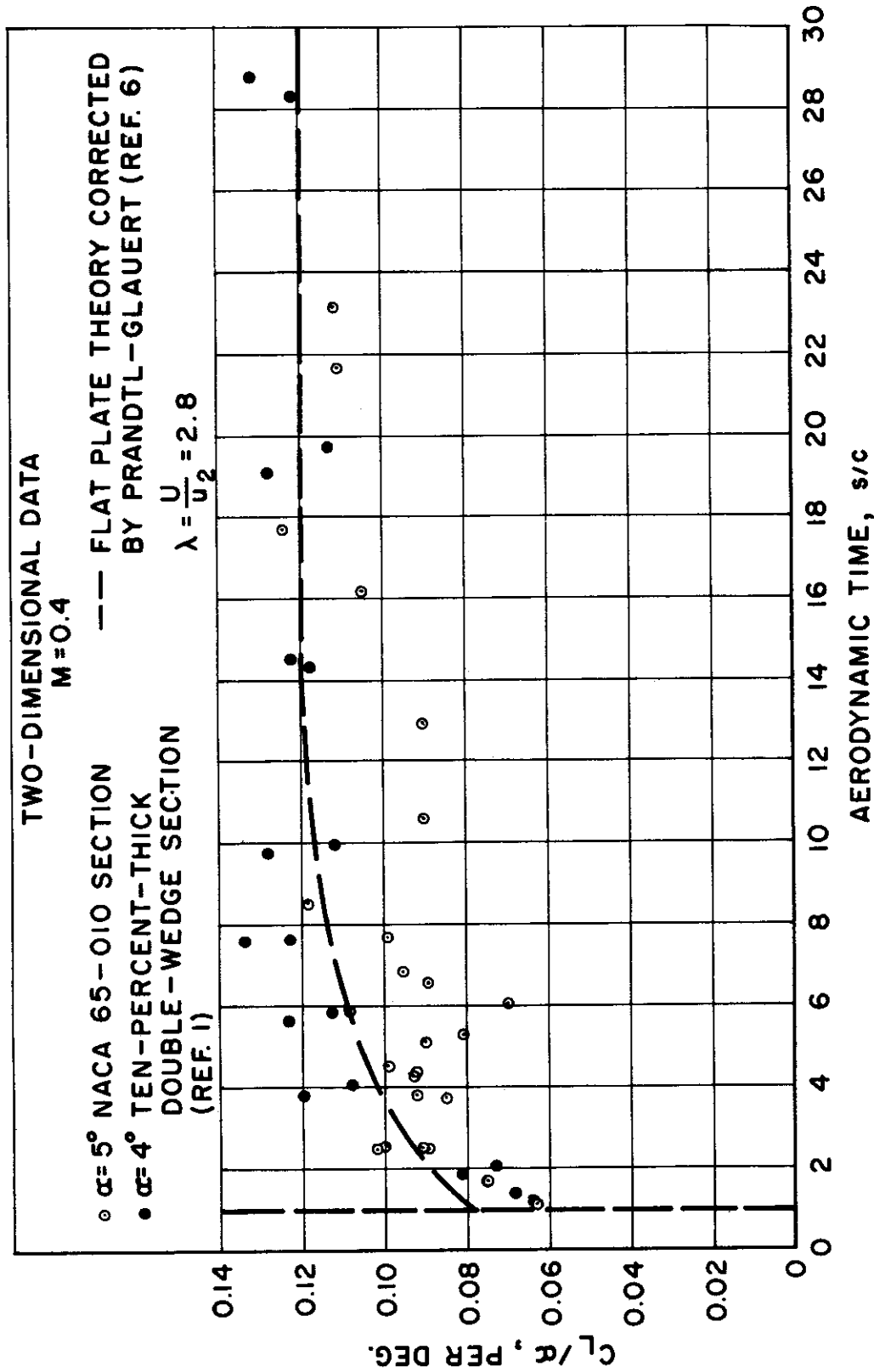


Fig. 29 Comparisons of Theoretical and Experimental Variations of the Ratio of Lift Coefficient to Angle-of-Attack during the Post-Diffractive-Flow Period

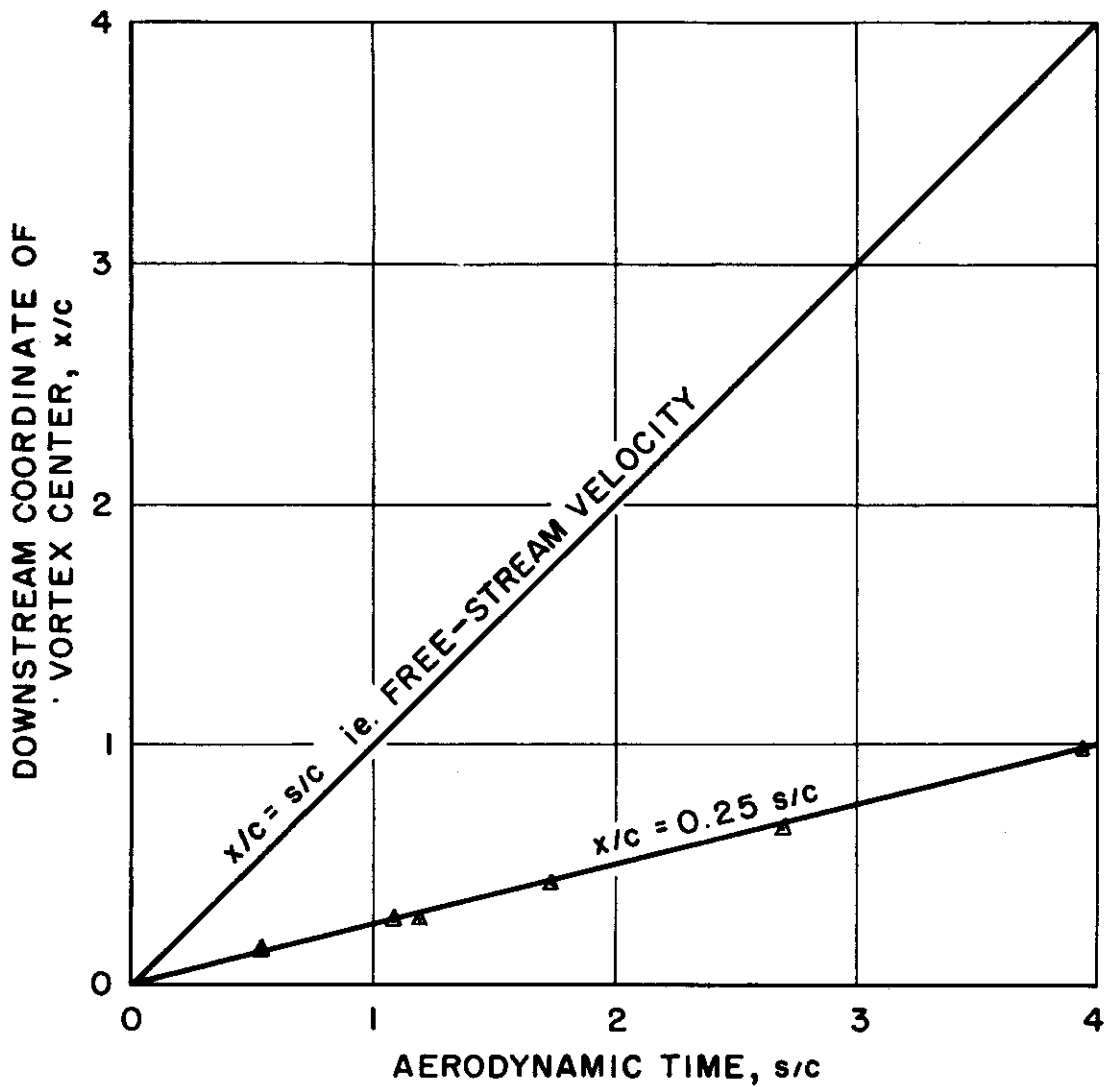


Fig. 30 Downstream Displacement History of the Strong Leading-Edge Vortex for the 30-Degree Angle-of-Attack Case

TABLE I
Test Conditions for Interferometric Studies

Run No.	s/c	P ₁ psi	a ₁ fps	U fps	u ₂ fps	M ₂	Re ₂ x 10 ⁻⁶	α deg.
77.19	0.054	14.58	1133	1468	494	0.400	1.271	5.0
77.33	0.077	14.68	1137.5	1466	486	0.393	1.233	5.0
77.22	0.191	14.73	1133.5	1464	489	0.396	1.264	5.0
77.18	0.325	14.58	1132	1466	492	0.399	1.263	5.0
77.39	0.350	14.79	1135.5	1470	494	0.399	1.277	5.0
77.37	0.355	14.68	1134	1466	490	0.397	1.262	5.0
77.38	0.393	14.68	1134	1464	488	0.396	1.256	5.0
77.25	0.416	14.73	1133.5	1459	482	0.391	1.244	5.0
77.15	0.573	14.58	1135.5	1465	487	0.394	1.237	5.0
77.24	0.732	14.73	1133.5	1461	484	0.393	1.248	5.0
77.14	0.993	14.58	1135.5	1465	487	0.394	1.237	5.0
77.30	1.125	14.68	1137.5	1466	486	0.393	1.233	5.0
77.12	1.725	14.58	1132.5	1466	493	0.400	1.269	5.0
77.36	2.521	14.68	1134	1463	487	0.394	1.249	5.0
77.35	3.810	14.68	1133.9	1461	485	0.393	1.242	5.0
77.32	6.051	14.68	1137.5	1489	516	0.415	1.328	5.0
77.9	6.563	14.58	1132.5	1472	501	0.405	1.293	5.0
77.29	8.565	14.68	1137.5	1457	474	0.384	1.194	5.0
77.10	12.96	14.58	1132.5	1467	494	0.400	1.272	5.0
77.16	17.66	14.58	1137.5	1463	482	0.389	1.210	5.0
77.34	21.66	14.68	1137.5	1474	497	0.401	1.267	5.0
77.11	23.14	14.58	1132.5	1463	489	0.397	1.256	5.0
77.3	33.02	14.73	1134	1461	485	0.393	1.247	5.0
77.31	44.41	14.68	1137.5	1463	482	0.389	1.218	5.0
77.23	57.53	14.73	1133.5	1466	491	0.398	1.271	5.0
108.14	2.471	14.81	1131	1463	491	0.398	1.287	4.9
108.26	2.479	14.66	1130	1464	493	0.400	1.284	4.9
108.34	2.568	14.56	1132.5	1474	504	0.407	1.300	4.9
108.18	3.745	14.79	1132.5	1463	489	0.397	1.275	4.9
108.35	4.305	14.56	1132.5	1456	479	0.389	1.220	4.9

TABLE I (Continued)

Test Conditions for Interferometric Studies

Run No.	s/c	p ₁ psi	a ₁ fps	U fps	u ₂ fps	M ₂	Re ₂ x 10 ⁻⁶	α deg.
108.25	4.392	14.66	1130	1460	487	0.396	1.265	4.9
108.17	4.558	14.79	1132.5	1471	500	0.405	1.307	4.9
108.13	5.139	14.81	1131	1463	491	0.398	1.287	4.9
108.19	5.278	14.79	1132.5	1464	490	0.398	1.277	4.9
108.9	5.866	14.81	1131	1459	486	0.395	1.271	4.9
108.22	6.861	14.79	1132.5	1474	504	0.407	1.320	4.9
108.12	7.694	14.81	1131	1474	505	0.409	1.333	4.9
108.8	10.62	14.81	1131	1454	479	0.390	1.249	4.9
108.7	16.18	14.81	1131	1474	506	0.409	1.336	4.9

TABLE II

Test Conditions for Interferometric Studies

Run No.	s/c	P ₁ psi	a ₁ fps	U fps	u ₂ fps	M ₂	Re ₂ x 10 ⁻⁶	α deg.
78.46	0.043	14.57	1133.5	1462	486	0.394	1.240	10.0
78.61	0.090	14.76	1133.5	1459	482	0.391	1.244	10.0
78.30	0.173	14.61	1132.5	1464	490	0.397	1.261	10.0
78.19	0.299	14.61	1132.5	1462	486	0.395	1.252	10.0
78.52	0.314	14.57	1132.5	1458	483	0.392	1.233	10.0
78.57	0.384	14.57	1132.5	1463	489	0.397	1.255	10.0
78.40	0.454	14.70	1138.5	1470	490	0.395	1.242	10.0
78.12	0.574	14.54	1131.5	1467	494	0.400	1.270	10.0
78.29	0.739	14.61	1132.5	1463	488	0.396	1.255	10.0
78.45	0.990	14.57	1133.5	1463	487	0.395	1.243	10.0
78.51	1.072	14.57	1133.5	1459	482	0.391	1.228	10.0
78.28	1.711	14.61	1132.5	1465	491	0.398	1.264	10.0
78.39	2.571	14.70	1138.5	1471	491	0.396	1.245	10.0
78.44	3.824	14.57	1133.5	1463	487	0.395	1.243	10.0
78.38	5.643	14.70	1138.5	1469	489	0.394	1.238	10.0
78.23	6.482	14.61	1132.5	1469	497	0.402	1.283	10.0
78.56	8.850	14.57	1132.5	1463	489	0.397	1.255	10.0
78.55	13.06	14.57	1132.5	1470	498	0.403	1.283	10.0
78.60	21.98	14.76	1133.5	1471	496	0.403	1.294	10.0
78.27	34.03	14.61	1132.5	1471	499	0.404	1.290	10.0
78.43	45.92	14.57	1133.5	1471	498	0.403	1.278	10.0
78.49	58.32	14.57	1132.5	1471	499	0.404	1.287	10.0

TABLE III								
Test Conditions for Interferometric Studies								
Run No.	s/c	P ₁ psi	a ₁ fps	U fps	u ₂ fps	M ₂	Re ₂ x 10 ⁻⁶	α deg.
93.23	0.040	7.10	1141	1481	502	0.403	0.614	15.6
93.9	0.156	7.28	1143.5	1485	504	0.404	0.628	15.6
93.13	0.352	7.28	1143.5	1488	508	0.407	0.635	15.6
93.19	0.448	6.61	1144	1482	499	0.400	0.562	15.6
93.27	0.563	7.10	1140	1477	498	0.401	0.612	15.6
93.24	0.709	7.10	1141	1481	502	0.403	0.614	15.6
93.50	0.888	7.24	1142	1482	501.2	0.403	0.624	15.6
93.29	1.117	7.10	1140	1478	499	0.402	0.612	15.6
93.14	1.256	7.28	1143.5	1482	499	0.400	0.621	15.6
93.17	1.887	6.61	1144	1485	502	0.403	0.568	15.6
93.33	2.678	7.05	1142	1478	496	0.399	0.600	15.6
93.10	4.038	7.28	1143.5	1481	498	0.400	0.619	15.6
93.20	6.015	6.61	1144	1489	508	0.407	0.576	15.6
93.35	6.461	7.59	1141	1473	491	0.396	0.640	15.6
93.11	9.057	7.28	1143.5	1478	494	0.397	0.614	15.6
93.36	13.03	7.59	1141	1476	495	0.398	0.646	15.6
93.21	22.24	6.61	1144	1488	507	0.406	0.575	15.6
93.25	34.04	7.10	1141	1478	498	0.400	0.609	15.6
93.37	45.60	7.59	1141	1475	494	0.397	0.644	15.6
93.28	58.29	7.10	1140	1477	498	0.401	0.612	15.6
104.27	0.227	7.34	1132.5	1466	493	0.400	0.640	14.7
104.26	0.528	7.34	1132.5	1463	488	0.396	0.631	14.7
104.17	0.566	7.34	1132.5	1470	499	0.405	0.651	14.7
104.12	0.695	7.34	1132.5	1466	493	0.400	0.640	14.7
104.23	0.712	7.34	1132.5	1468	496	0.402	0.643	14.7
104.11	0.887	7.34	1132.5	1472	501	0.405	0.651	14.7
104.22	0.893	7.34	1132.5	1468	496	0.402	0.643	14.7
104.6	1.968	7.34	1132.5	1476	506	0.409	0.658	14.7
104.21	4.014	7.34	1132.5	1467	494	0.400	0.641	14.7
104.10	5.981	7.34	1132.5	1471	499	0.404	0.648	14.7

TABLE III (Continued)

Test Conditions for Interferometric Studies

Run No.	s/c	P ₁ psi	a ₁ fps	U fps	u ₂ fps	M ₂	Re ₂ x 10 ⁻⁶	α deg.
104.16	9.199	7.34	1132.5	1470	499	0.405	0.651	14.7
104.5	12.92	7.34	1132.5	1463	488	0.396	0.631	14.7
104.15	34.34	7.34	1132.5	1470	499	0.405	0.651	14.7
104.9	34.44	7.34	1132.5	1472	501	0.405	0.651	14.7
104.20	34.45	7.34	1132.5	1472	501	0.405	0.651	14.7
104.4	34.47	7.34	1132.5	1472	501	0.405	0.651	14.7

TABLE IV
Test Conditions for Interferometric Studies

Run No.	s/c	P ₁ psi	a ₁ fps	U fps	u ₂ fps	M ₂	Re ₂ x 10 ⁻⁶	α deg.
95.28	0.139	7.40	1136.5	1471	494	0.399	0.635	30.3
95.34	0.192	7.40	1136.5	1466	488	0.394	0.625	30.3
95.14	0.254	7.36	1137.5	1472	494	0.399	0.630	30.3
95.37	0.280	7.41	1136.5	1468	491	0.396	0.631	30.3
95.33	0.364	7.40	1136.5	1465	486	0.393	0.622	30.3
95.24	0.472	7.40	1136.5	1461	481	0.389	0.615	30.3
95.13	0.656	7.36	1137.5	1468	489	0.395	0.622	30.3
95.44	0.855	7.23	1145	1478	492	0.395	0.603	30.3
95.32	1.079	7.40	1136.5	1471	494	0.398	0.635	30.3
95.19	1.194	7.40	1136.5	1470	493	0.398	0.633	30.3
95.12	2.689	7.36	1137.5	1476	499	0.402	0.638	30.3
95.27	3.929	7.40	1136.5	1468	491	0.396	0.630	30.3
95.42	5.901	7.29	1138.5	1479	501	0.404	0.634	30.3
95.18	6.439	15.12	1136.5	1468	491	0.396	0.630	30.3
95.31	9.040	15.12	1136.5	1471	494	0.399	0.636	30.3
95.11	13.27	15.03	1137.5	1478	502	0.494	0.642	30.3
95.45	21.04	14.78	1145	1470	482	0.387	0.586	30.3
95.17	32.65	15.12	1136.5	1459	478	0.387	0.610	30.3
95.26	45.47	15.12	1136.5	1470	492	0.398	0.633	30.3
95.21	57.94	15.12	1136.5	1472	495	0.400	0.638	30.3
103.42	2.678	7.34	1132.5	1468	496	0.402	0.643	30.0
103.41	3.987	7.34	1132.5	1470	498	0.403	0.646	30.0
103.40	5.851	7.34	1132.5	1468	496	0.402	0.643	30.0
103.39	5.855	7.34	1132.5	1471	499	0.404	0.648	30.0
103.34	7.978	7.34	1132.5	1467	494	0.400	0.641	30.0
103.33	9.229	7.34	1132.5	1474	504	0.407	0.655	30.0
103.32	13.23	7.34	1132.5	1472	501	0.405	0.651	30.0